NASA Technical Memorandum 107419

Wind Tunnel Measured Effects on a Twin-Engine Short-Haul Transport Caused by Simulated Ice Accretions

Data Report

Andrew Reehorst, Mark Potapczuk, and Thomas Ratvasky
Lewis Research Center
Cleveland, Ohio

Brenda Gile Laflin
Langley Research Center
Hampton, Virginia

May 1997

National Aeronautics and
Space Administration

WIND TUNNEL MEASURED EFFECTS ON A TWIN-ENGINE SHORT-HAUL TRANSPORT CAUSED BY SIMULATED ICE ACCRETIONS: DATA REPORT

Andrew Reehorst
Mark Potapczuk
Thomas Ratvasky

NASA Lewis Research Center
Cleveland, Ohio

and

Brenda Gile Laflin

NASA Langley Research Center
Hampton, Virginia

Abstract

The purpose of this report is to release the data from the NASA Langley/Lewis 14 by 22 foot wind tunnel test that examined icing effects on a 1/8 scale twin-engine short-haul jet transport model. Presented in this document are summary data from the major configurations tested. The entire test database in addition to ice shape and model measurements is available as a data supplement in CD-ROM form. Data measured and presented are: wing pressure distributions, model force and moment, and wing surface flow visualization.

Nomenclature

b wing span, feet

c_s slat chord length, feet

c_w wing main element chord length, feet

c_{ff} forward flap element chord length, feet

c_{mf} mid flap element chord length, feet

c_{af} aft flap element chord length, feet

c_p pressure coefficient, $(p_n-p_{atm})/q$

C_D drag coefficient, Drag/qS

C_L lift coefficient, Lift/qS

C_m pitching moment coefficient, pitching moment/qSb

p_{atm} atmospheric pressure, lb/ft^2

p_n pressure at specific model tap n=1,2..., lb/ft^2

q free-stream dynamic pressure, lb/ft^2

S wing area, ft^2

α angle of attack, deg

β sideslip angle, deg

δ_f flap deflection angle, deg

Introduction

Aircraft icing simulation methods are currently under development in order to provide design and certification tools for the aircraft industry. These tools include simulation methods for ice accretion, ice protection system performance, and aircraft performance degradation, and scaling methods. As in all computer simulations of physical processes, it is important to determine the quality of the prediction. This paper presents results of an experimental program designed to provide validation information for performance degradation of a commercial transport aircraft with ice accumulated on its wing and tail.

It is important to understand how ice accretions can influence the aerodynamic behavior of an aircraft in order to determine the ice protection requirements and to understand the effects of an ice protection system failure. This is currently done through flight and wind tunnel tests using real or artificial ice accretions. The development of a reliable computational tool for evaluation of performance changes due to ice accretion would help to decrease the number of such tests and in turn reduce the time and costs of design and certification.

The need for a computational tool and therefore a validation database is based on the desire of several aircraft manufacturers to determine the size and shape of ice accretions which are critical to aerodynamic performance. Currently, there is not a great deal of such data publicly available for a complete aircraft with ice. There have been several studies of airfoil and wing models with leading edge ice accretions[1-3]. These have provided information of sufficient quality to assess the accuracy of computational simulations and have helped to point out areas for improvement of such simulation methods. The data from this test program should serve a similar purpose

for the evaluation of simulation methods applied to complete aircraft configurations.

Presented in this document are summary data from the major configurations tested. The entire test database in addition to ice shape and model measurements is available as a data supplement in CD-ROM form. A discussion of the test results is available in Reference 4.

Test Apparatus

The wind tunnel test was conducted in the NASA Langley 14 by 22 foot subsonic wind tunnel. The test article was a 1/8 scale twin-engine short-haul jet transport model. Several aircraft configurations were examined including various flap and slat deflections, with and without landing gear. Two separate configurations of leading edge ice contamination were tested in addition to the uncontaminated baseline configuration.

Facility Description

The NASA Langley 14 by 22 foot Subsonic Tunnel[5] is a closed-circuit, single return, atmospheric wind tunnel with a test section that can be operated in a variety of configurations: closed, slotted, partially open, and open. For this test, the test section was operated in the closed configuration. The closed test section is 14.5 feet high by 21.75 feet wide by 50 feet long.

Model Description

The model used for this test was a 1/8 scale twin-engine subsonic transport with multi-element wings[6] shown in figure 1. The empennage consisted of a vertical tail with rudder and a motorized horizontal stabilizer with elevator. The engines were represented by two flow-through nacelles. The model was tested in cruise, take-off, and landing configurations.

Ice shape description

Two different artificial ice shapes were used for this test. They were based upon drawings of ice shapes used by Boeing (for a mid 1960s wind tunnel test of a similar aircraft[7]). The two shapes represent realistically sized ice accretions for this configuration. Because of the age of the information, no clear documentation was identified stating the method of determining these shapes, however, it is conjectured that the shapes were developed using either the Boeing ice shape prediction technique[8] or the method described in the FAA icing handbook[9].

The Boeing outlines were transformed to provide the appropriate scale and orientation for production of the artificial ice shapes in the NASA Lewis Research Center's wood-model shop. The ice shapes were manufactured for inboard and outboard wing, vertical tail and horizontal tail surfaces for both sides of the aircraft. The ice shapes

were attached to the aircraft model using mechanical fasteners and double sided adhesive tape. Figures 2 and 3 show the artificial ice shapes attached to the horizontal tail. After being attached, the joints between the aircraft model and the ice shapes were filled using modeling clay. Profiles of the ice shapes installed on the aerodynamic surfaces were measured after the test to document the ice shapes used and their alignment to the aircraft surfaces.

Roughness determination

The roughness size for the model ice shapes was calculated by scaling down experimentally measured roughness. Roughness elements have been measured in the NASA Lewis Icing Research Tunnel and have been determined to be on the order of 0.02 inches[10,11]. This approximate value does not appear to vary significantly as the chord length or airfoil section changes, and is therefore considered reasonable for the full scale transport ice accretion. The next step in calculating the model ice roughness size was to determine an appropriate scaling method. Neither full scale roughness nor geometrically scaled roughness are appropriate, since neither will appropriately address the change in the flow field due to the presence of roughness. The method selected was to scale the roughness with the ratio of the model to full scale boundary layer momentum thicknesses. The momentum thickness was calculated for both the full scale and 1/8 scale ice shapes using Cebeci's IBL computer program[12,13]. The average ratio between the two momentum thickness was 0.5411. When the full scale roughness size of 0.02 inches is multiplied by the scaling ratio of 0.5411, the scale model roughness size becomes 0.011 inches. This corresponds to a roughness that falls between a #60 and #70 grit. #60 grit, with nominal 0.0117 inch diameters, was utilized for this experiment. Figure 4 is a close-up view of the grit applied to the artificial ice shape.

Test Procedures

The test was conducted at dynamic pressures, q, from 10 lb/ft^2 to 50 lb/ft^2 corresponding to Reynolds numbers of 8.2×10^5 to 1.8×10^6 and Mach numbers of 0.08 to 0.18. Data was obtained over an angle-of-attack range from -4^o through 16^o with sideslip varying from -10^o to 10^o.

Aerodynamic forces and moments were obtained with a six-component strain-gauge balance and wing pressures were obtained with electronically scanned pressure devices from flush pressure ports. Angle-of-attack and sideslip were measured electronically in the model/model support system. Wing, body and wake blockage corrections to free stream dynamic pressure[14] were applied as were corrections for tunnel wall interference[15].

Two different flow visualization techniques were utilized during this test. The first technique was a surface oil method that utilized motor oil with a fluorescent additive viewed under ultraviolet lighting. The oil was painted on the left wing surface in a span-wise direction. When the proper test condition was achieved an overhead photograph was quickly taken with an ultraviolet flash. Due to the restrictive nature of

this testing technique, only a select number of model configurations were examined with this technique.

A less restrictive technique was utilized for almost all test conditions. This technique makes use of fluorescent mono-filament wing tufts glued to the left wing. The tufts were digitally photographed using an ultraviolet flash. The "mini-tufts" do not provide quite the image resolution of the oil flow visualization technique, but proved to be much more practical for regular use since they required little upkeep from one test condition to the next.

Data Presentation

Figures 5 through 86 represent a summary of the data available on the data supplement CD-ROM.

The figures are organized such that figures 5 through 28 display the results of the testing with the intermediate temperature ice shape (Ice #2, figure 3) with the model in the δ_f=40^o wing configuration. Results shown are the C_L, C_m, C_D, C_l, C_n, C_Y curves, pressure coefficient curves, oil flow visualization, and mini-tuft flow visualization images.

Figures 29-46 represent the results for Ice #2 with the model in the cruise wing configuration. Results shown are the C_L, C_m, C_D, C_l, C_n, C_Y curves, pressure coefficient curves, and mini-tuft flow visualization images.

Figures 47-58 represent the results of testing with the low temperature ice shape (Ice #1, figure 2) with the model in the δ_f=40^o wing configuration. Results shown are the C_L, C_m, C_D, C_l, C_n, C_Y curves, pressure coefficient curves, and mini-tuft flow visualization images.

Figures 59-69 represent the results for Ice #1 with the model in the δ_f=30^o wing configuration. Results shown are the C_L, C_m, C_D, C_l, C_n, C_Y curves, pressure coefficient curves, and mini-tuft flow visualization images.

Figures 70-86 represent the results for Ice #1 with the model in the cruise wing configuration. Results shown are the C_L, C_m, C_D, C_l, C_n, C_Y curves, pressure coefficient curves, and mini-tuft flow visualization images.

Data Supplement

This report and its data supplement (in the form of a CD-ROM) are available from the NASA Center for AeroSpace Information (CASI), 800 Elkridge Landing Road, Linthicum Heights, Maryland, 21090-2934 (NASA Access Help Desk (301)621-0390). On the CD-ROM, the following information is available:

-Test database--the database is in Data Analysis System[16] (DAS) “ffsif” format (the DAS program is available from NASA Langley Research Center, Hampton, VA)

-Model photographs

-Model measurements--measurements of the model with the ice shapes installed (made with portable laser profilometer developed by Hovenac and Vargas[17])

-Model measurements notes--model measurement file naming convention

-Ice shape measurements--detailed measurements of the ice shapes

-Ice shape measurements notes--ice shape measurement file naming convention

-Mini-tuft images

-Mini-tuft image catalog

Acknowledgments

The authors would like to thank the efforts of Mr. Mario Vargas for his help in making the model measurements with his laser profilometer.

References

1. Reehorst, A., Potapczuk, M,, Ratvasky, T., and Gile Laflin, B.,"Wind Tunnel Measured Effects on a Twin-Engine Short-Haul Transport Caused by Simulated Ice Accretions", AIAA-96-0871, NASA TM-107143, January, 1996.

1. Bragg, M.B. and Spring, S.A., "An Experimental Study of the Flow Field about an Airfoil with Glaze Ice," AIAA Paper 87-0100, Jan. 1987.

2. Khodadoust, A. and Bragg, M.B.,"Measured Aerodynamic Performance of a Swept Wing with a Simulated Ice Accretion," AIAA Paper 90-0490, Jan. 1990.

3. Flemming, R.J., Britton, R.K., and Bond, T.H., "Model Rotor Icing Tests in the NASA Lewis Icing Research Tunnel," AGARD Conference Proceedings 496, Paper No. 9, Dec. 1991.

4. Reehorst, A., Potapczuk, M,, Ratvasky, T., and Gile Laflin, B.,"Wind Tunnel Measured Effects on a Twin-Engine Short-Haul Transport Caused by Simulated Ice Accretions", AIAA-96-0871, NASA TM-107143, January, 1996.

5. Gentry, Garl L. Jr., Quinto, P. Frank, Gatlin, Gregory M., and Applin, Zachary T.,"The Langley 14- by 22-Foot Subsonic Tunnel: Description, Flow Characteristics, and Guide for Users",NASA TP 3008, September 1990.

6. Paulson, John P.,"Wind-Tunnel Results of the Aerodynamic Characteristics of a 1/8-Scale Model of a Twin-Engine Short-Haul Transport", NASA TM X-74011, April 1977.

7. Hill, Eugene G., Personal communication, November 1992.

8. Wilder, Ramon, W.,"A theoretical and experimental means to predict ice accretion shapes for evaluating aircraft handling and performance characteristics", Paper 5, AGARD Advisory Report No. 127, September 1977.

9. Bowden, D.T., Gensemer, A.G., and Sheen, C.A.,"Engineering Summary of Airframe Icing Technical Data, FAA Technical Data, FAA Technical Report ADS-4, December 1963.

10. Hansman, R. John,"Analysis of Surface Roughness Generation in Aircraft Ice Accretion", AIAA-92-0298, January 1992.

11. Shin, Jaiwon,"Characteristics of Surface Roughness Associated with Leading Edge Ice Accretion",AIAA-94-0799, NASA TM-106459, January 1994.

12. Cebeci, T. and Chang, K.C.,"Calculation of Incompressible Rough-Wall Boundary-Layer Flows",AIAA Journal, Vol. 16, No. 7, July 1978.

13. Cebeci, T., Clark, R.W., Chang, K.C., Halsey, N.D. and Lee, K.,"Airfoils with Separation and the Resulting Wakes",Journal of Fluid Mechanics, Vol. 163, pp. 320-347, 1986.

14. Heyson, Harry H.,"Use of Superposition in Digital Computers to Obtain Wind-Tunnel Interference Factors for Arbitrary Configurations, With Particular Reference to V/STOL Models", NASA TR R-302, February 1969.

15. Rae, W.H., Jr., and Pope, A,Low-Speed Wind Tunnel Testing, John Wiley & Sons, Inc., 1984.

16. Graham, A.B.,“The Data Analysis System, System Description and User’s Guide”, NASA Langley Research Center, April, 1993.

17. Hovenac, E.A., and Vargas, M.,”A Lsser-Based Ice Shape Profilometer for Use in Icing Wind Tunnels”, NASA TM 106936, June, 1995.

Figure 1.—NASA Langley 1/8 scale twin engine subsonic transport model.

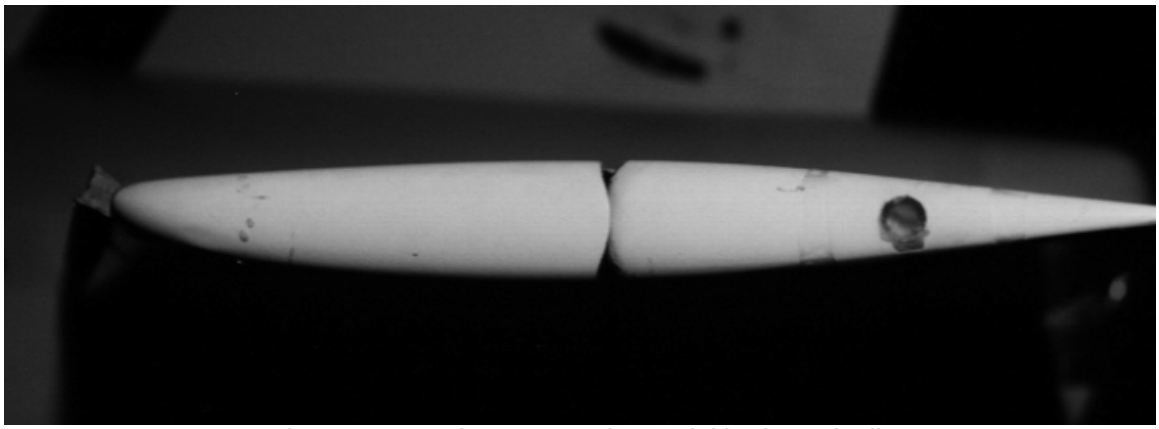

Figure 2.—Ice shape #1 on the model horizontal tail.

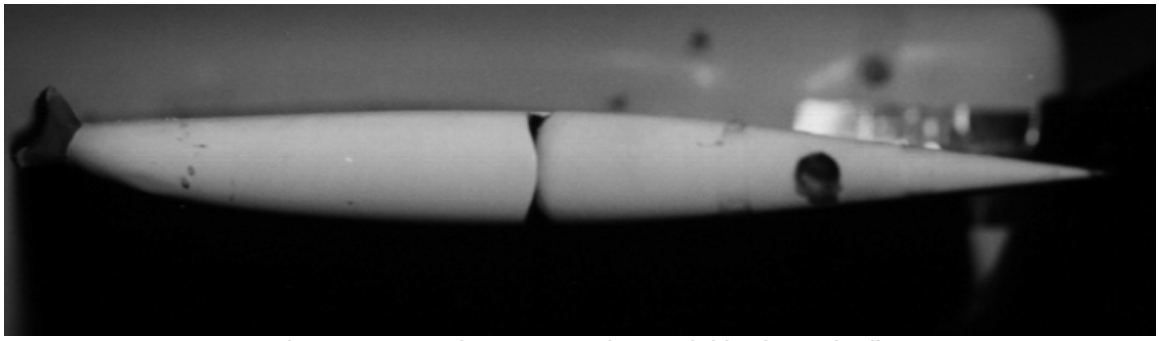

Figure 3.—Ice shape #2 on the model horizontal tail.

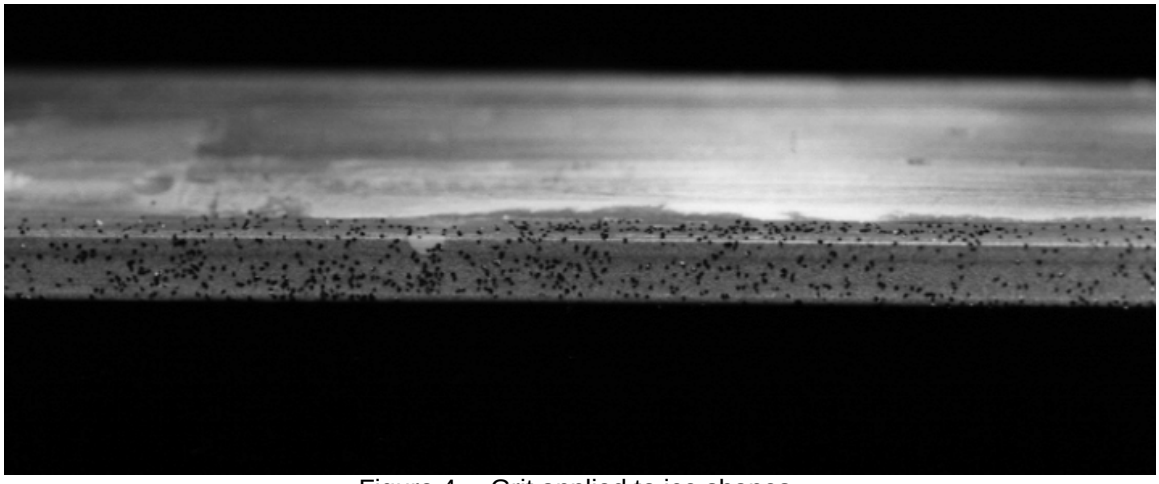

Figure 4.—Grit applied to ice shapes.

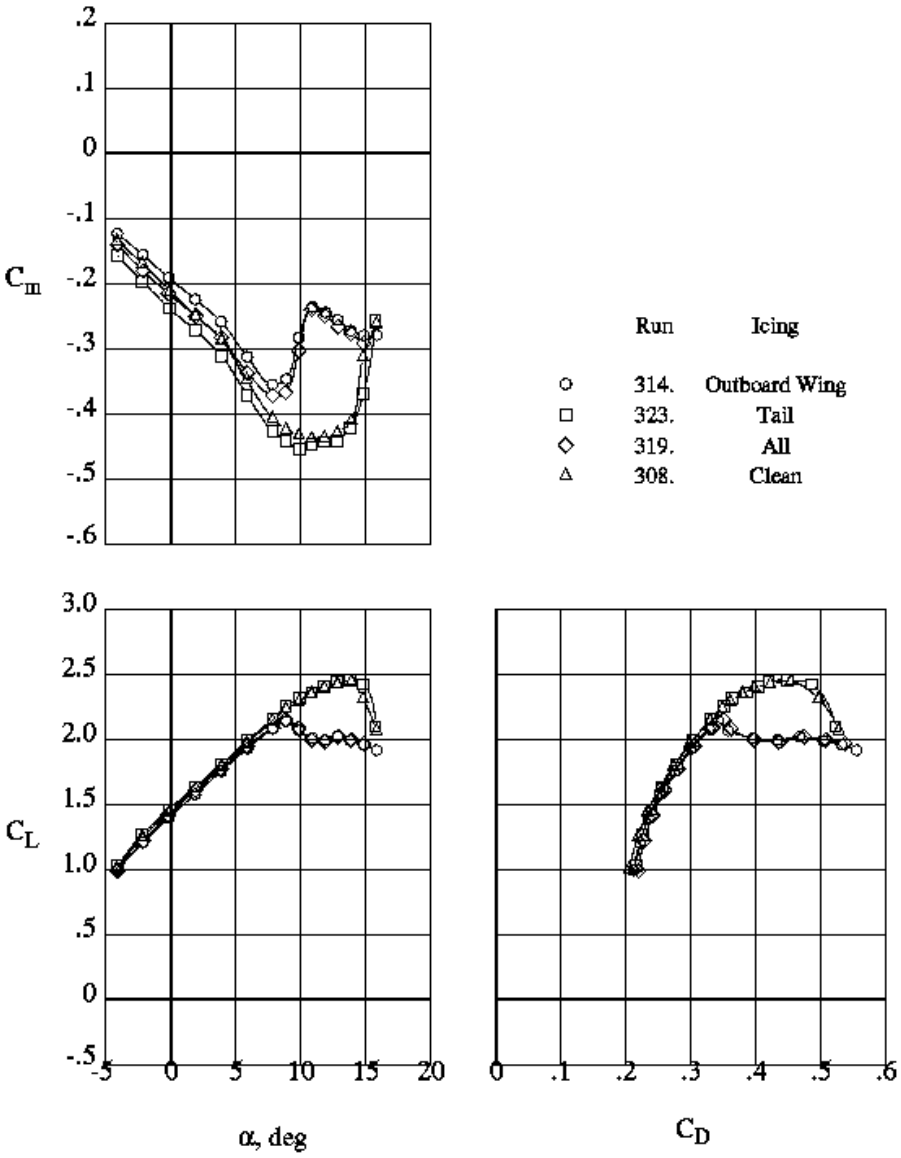

Figure 5.—Effects of Ice #2 on longitudinal aerodynamic characteristics of the model in the δ_f=40° configuration.

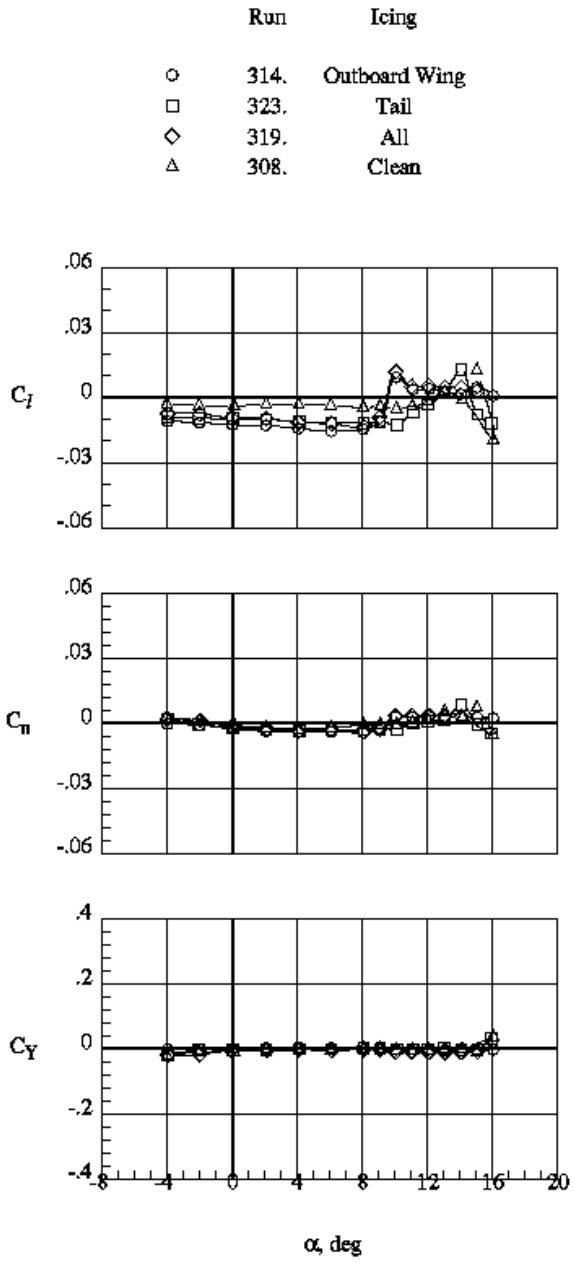

Figure 6.— Effects of Ice #2 and sideslip on the lateral aerodynamic characteristics of the model in the δ_f=40° configuration.

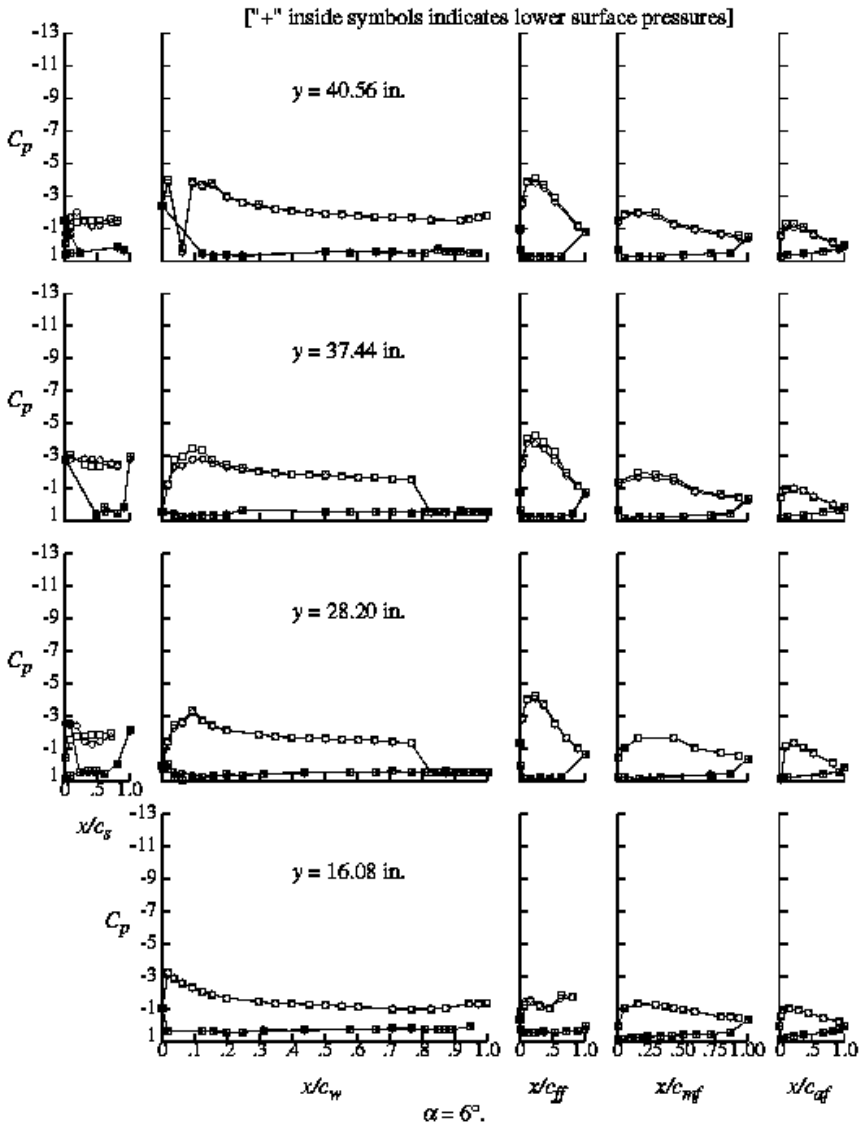

Figure 7.—Effect of Ice #2 on the wing pressure distribution for the model in the δ_f=40° configuration.

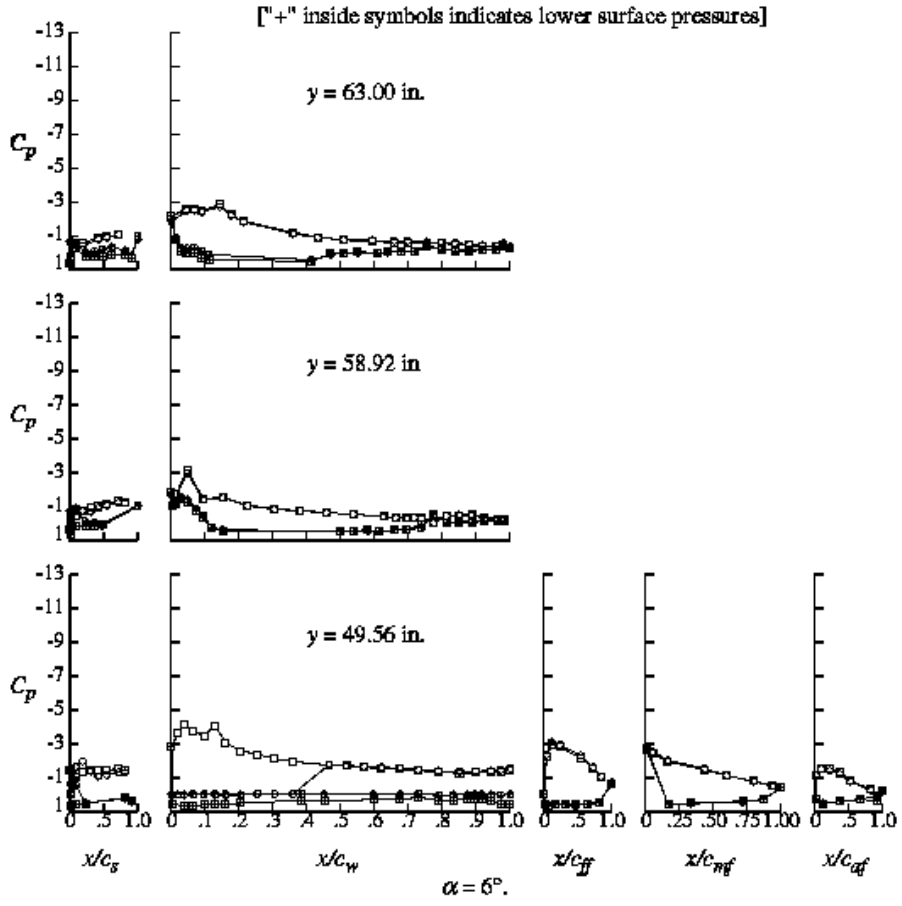

Figure 7 (concluded).—Effect of Ice #2 on the wing pressure distribution for the model in the δ_f=40° configuration.

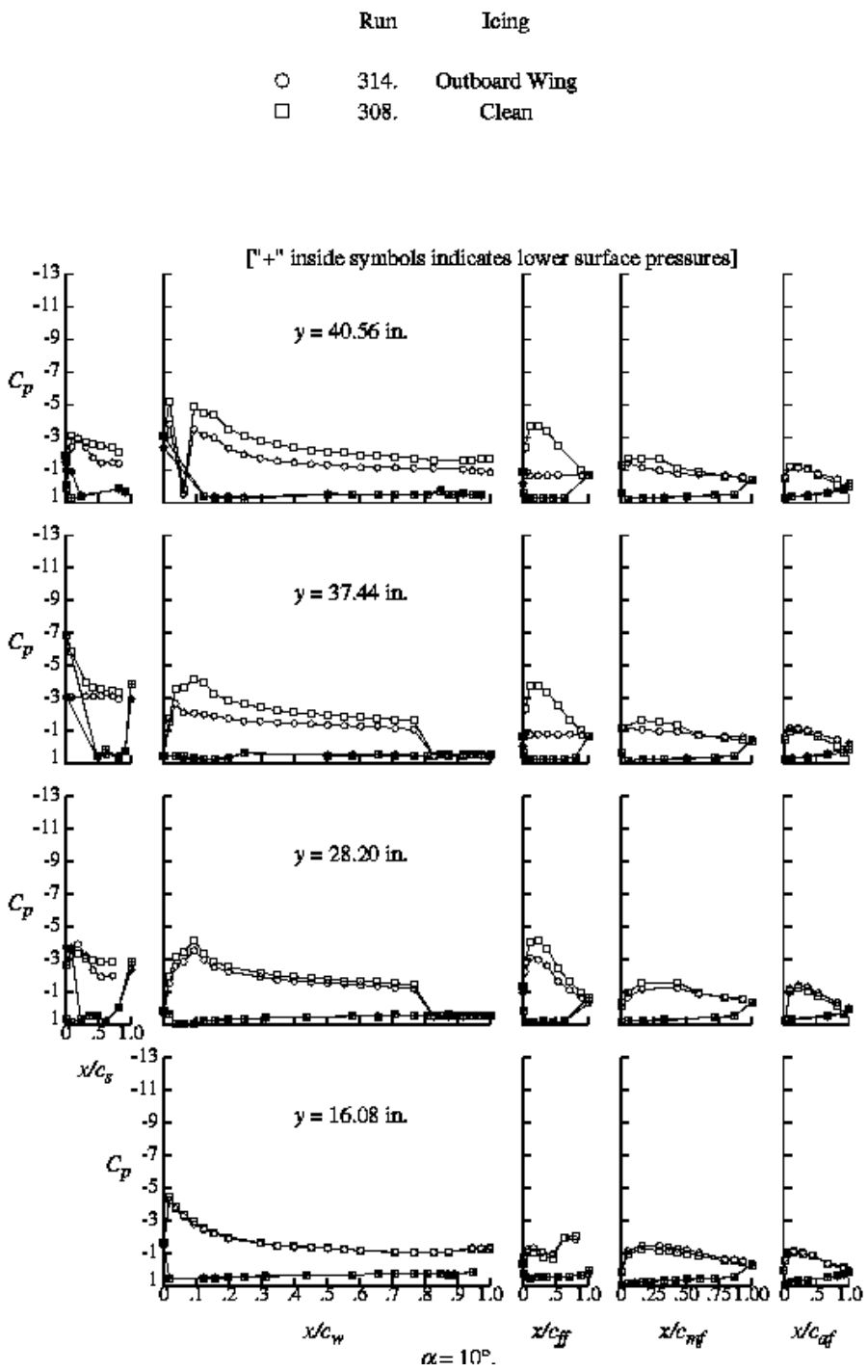

Figure 8.—Effect of Ice #2 on the wing pressure distribution for the model in the δ_f=40° configuration.

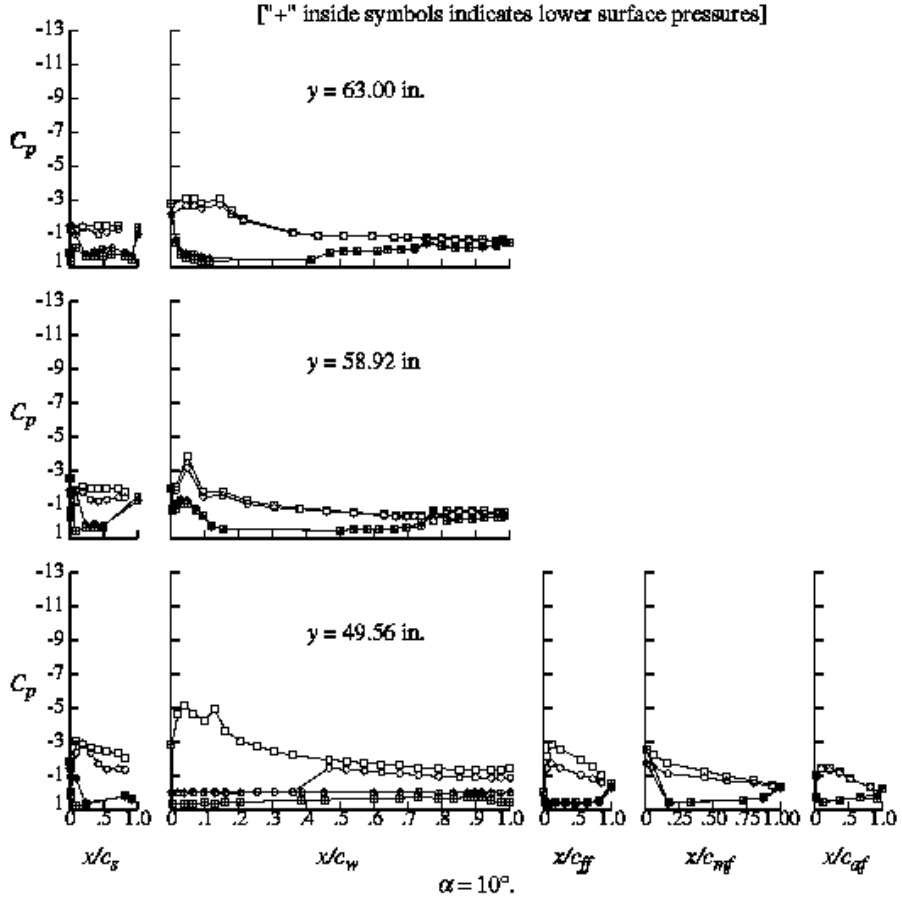

Figure 8 (concluded).—Effect of Ice #2 on the wing pressure distribution for the model in the δ_f=40° configuration.

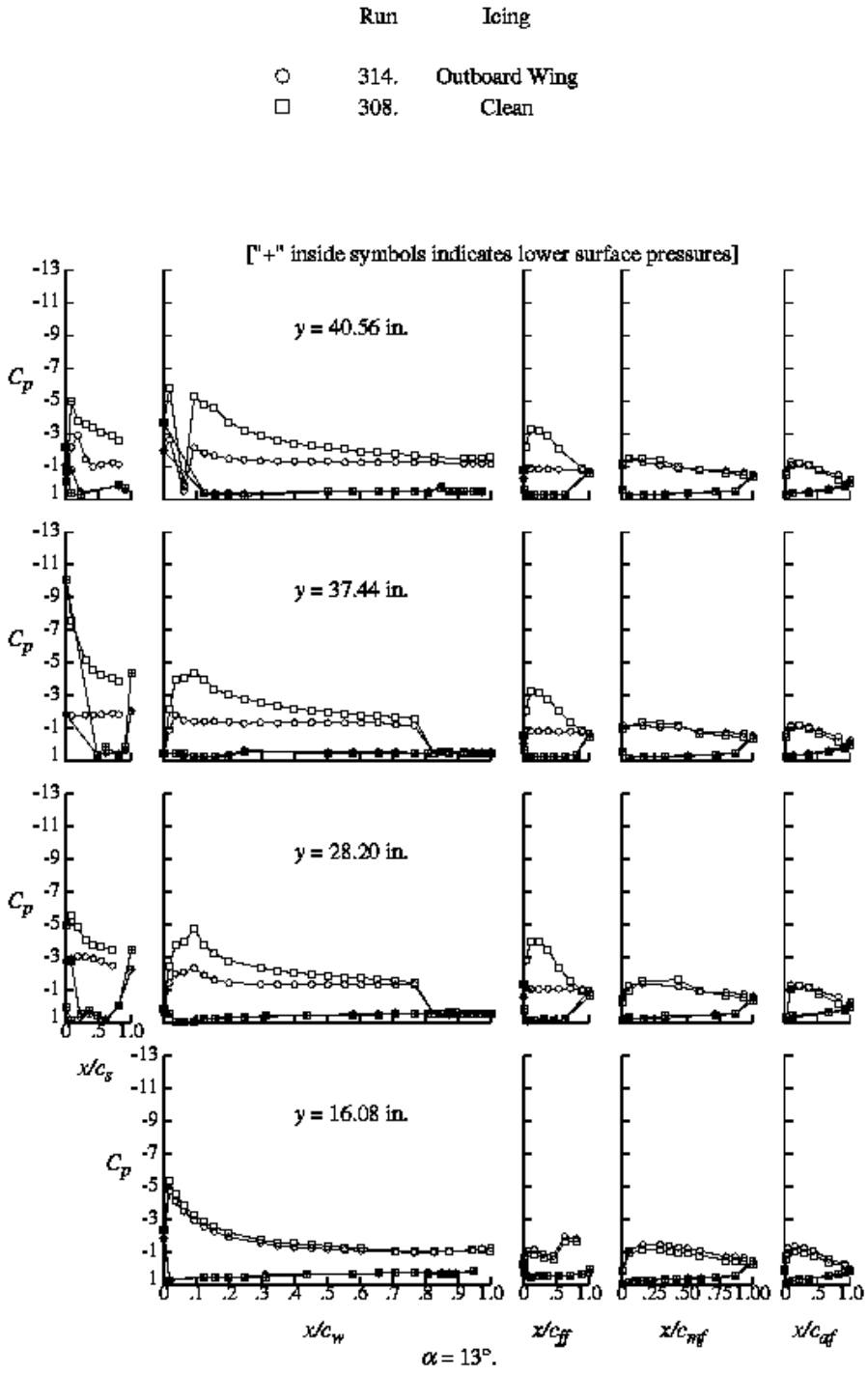

Figure 9.—Effect of Ice #2 on the wing pressure distribution for the model in the δ_f=40° configuration.

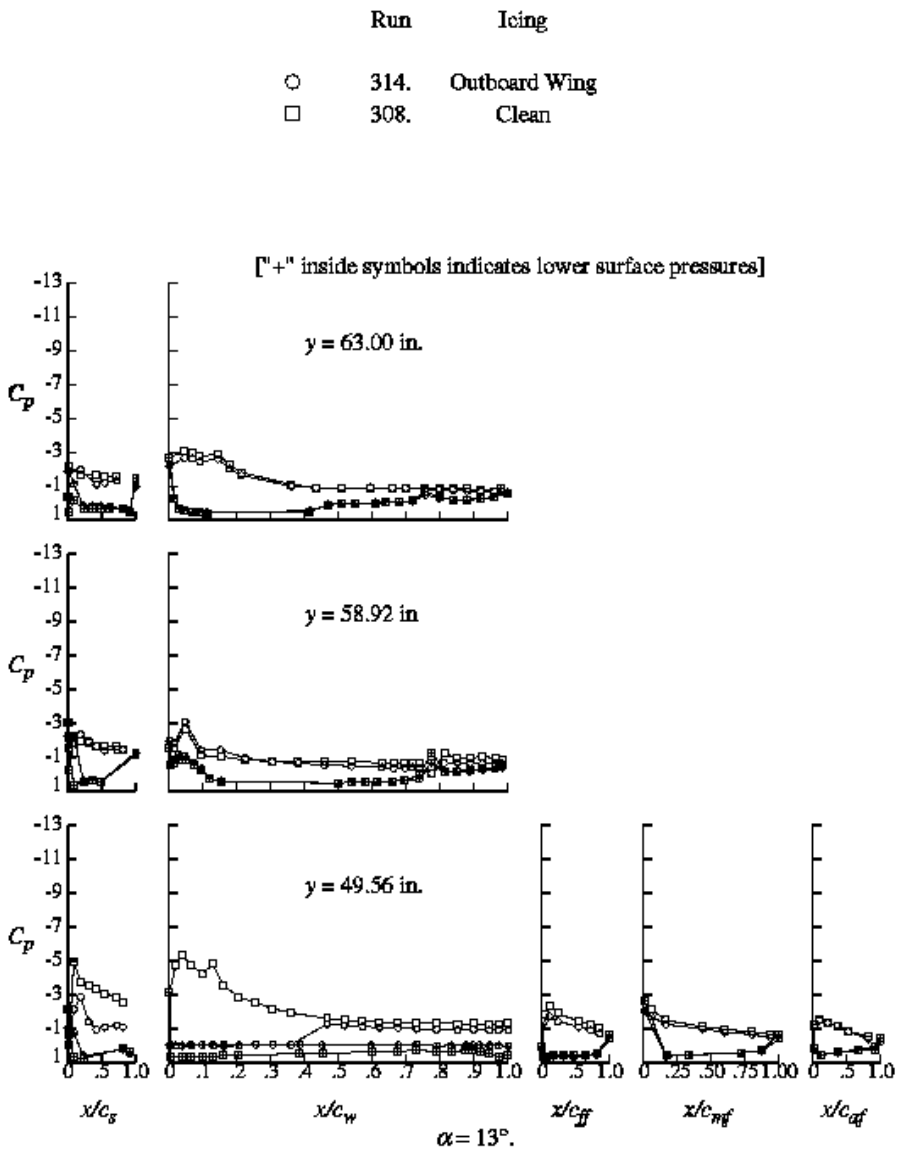

Figure 9 (concluded).—Effect of Ice #2 on the wing pressure distribution for the model in the δ_f=40° configuration.

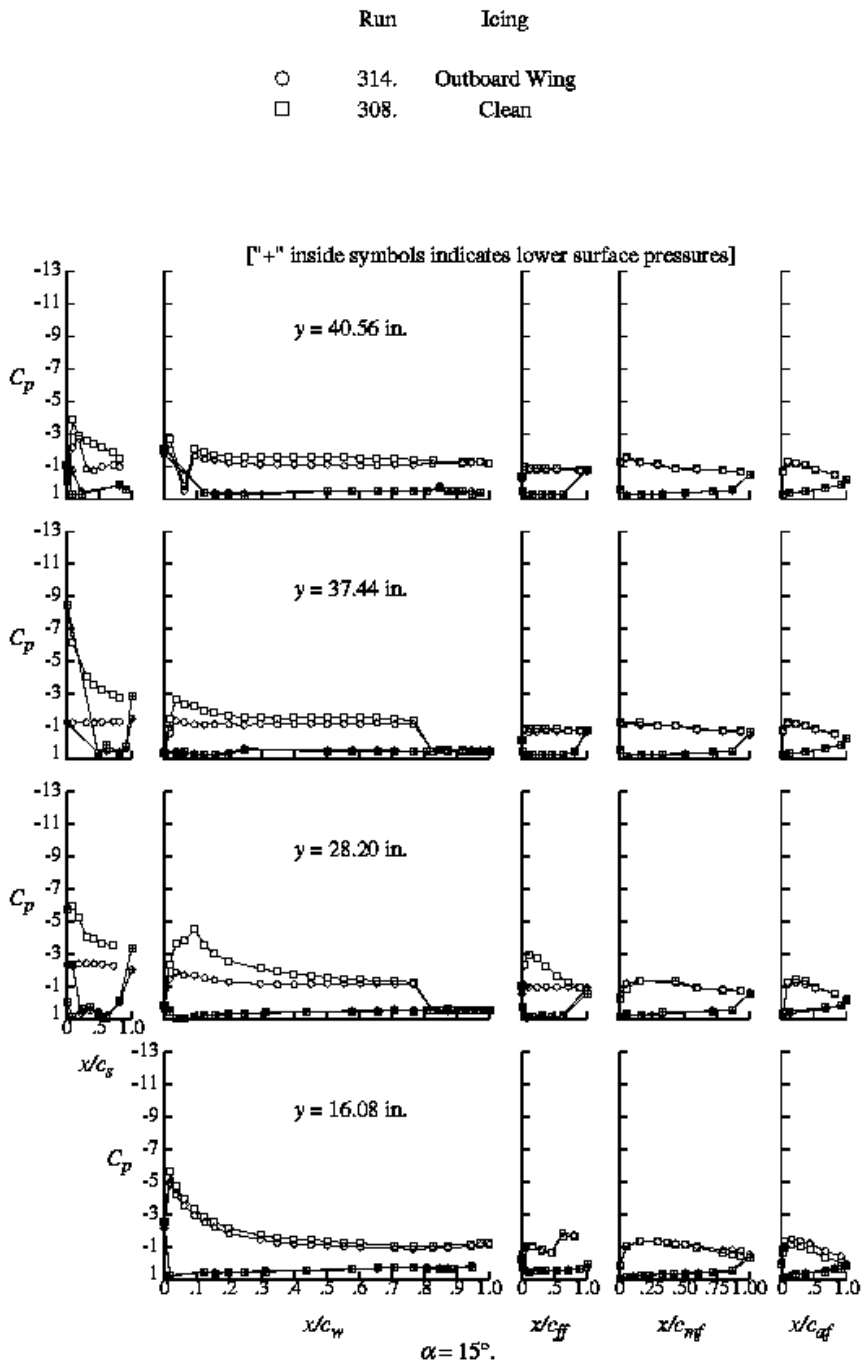

Figure 10.—Effect of Ice #2 on the wing pressure distribution for the model in the δ_f=40° configuration.

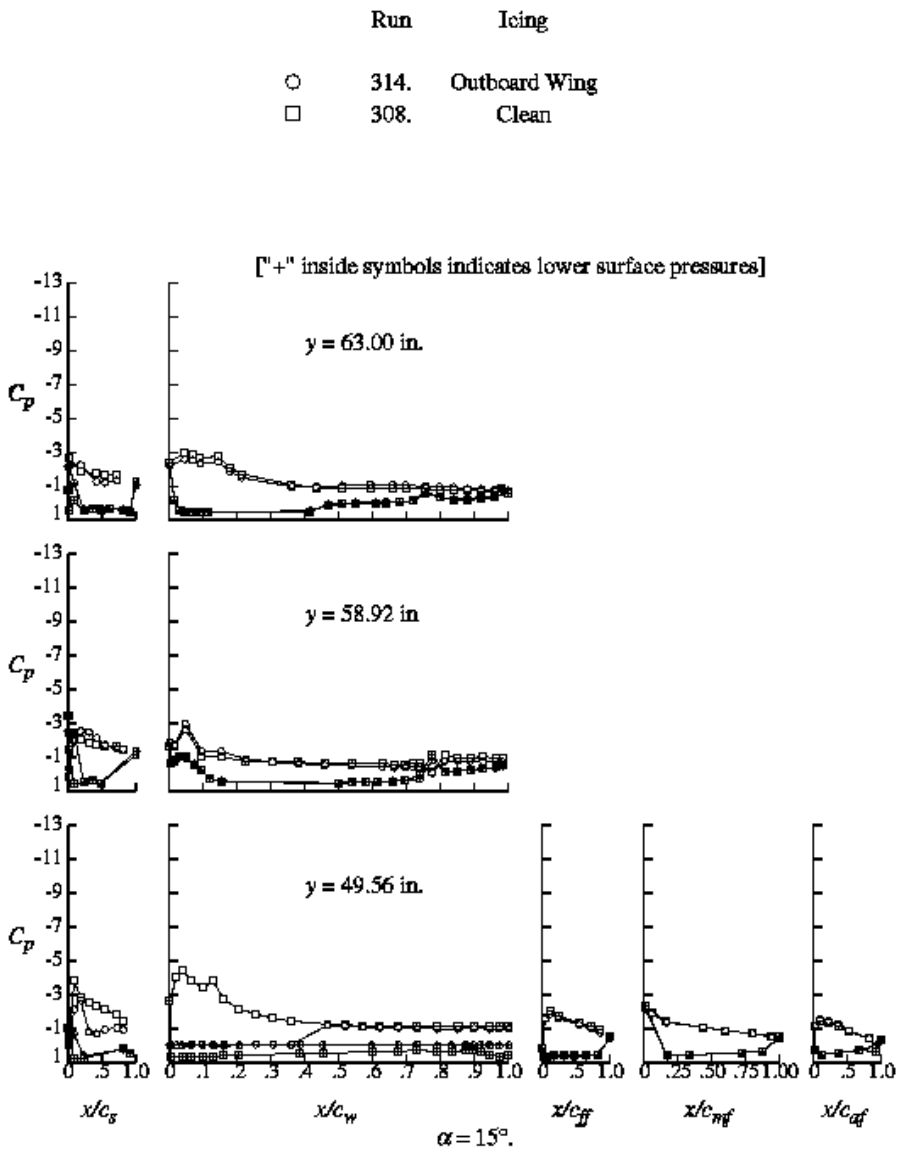

Figure 10 (concluded).—Effect of Ice #2 on the wing pressure distribution for the model in the δ_f=40° configuration.

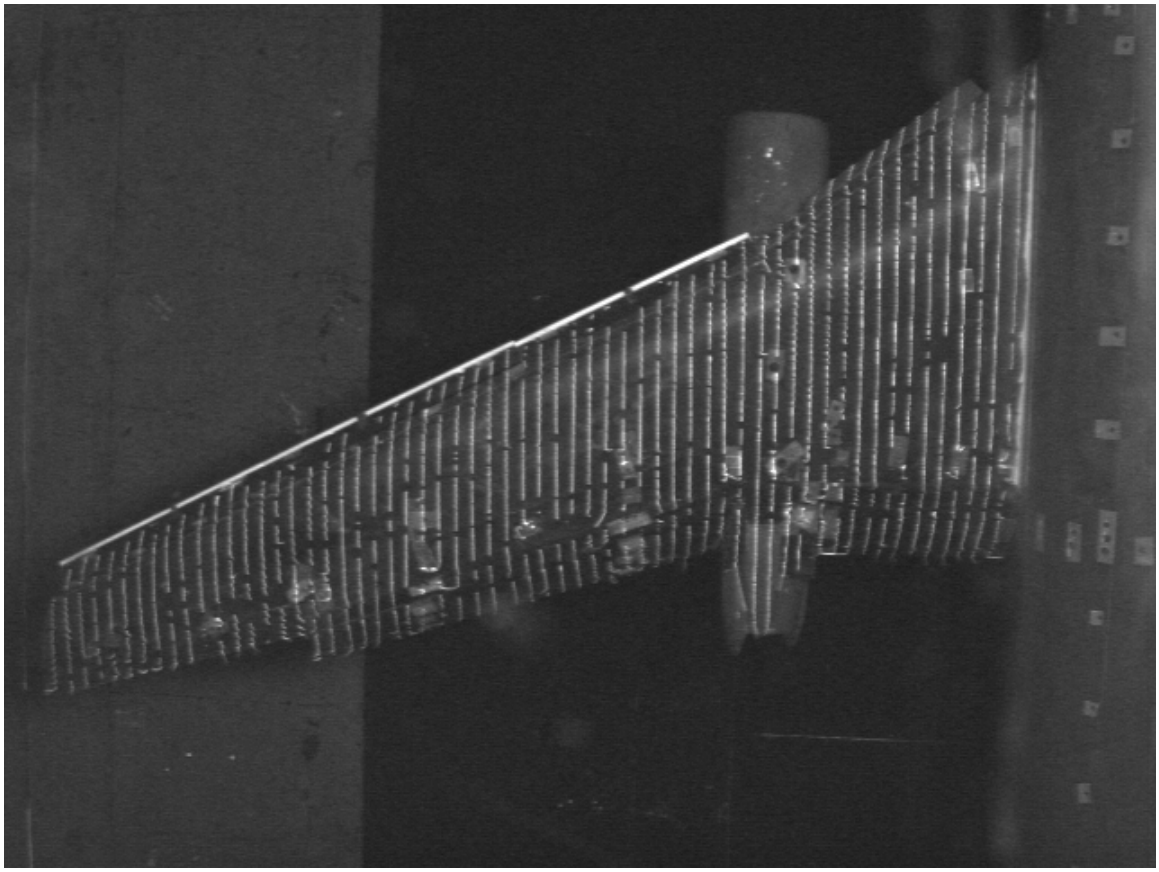

Figure 11.—Wing mini-tuft flow visualization for outboard ice #2, δ_f=40°, α=4°, run 314 condition.

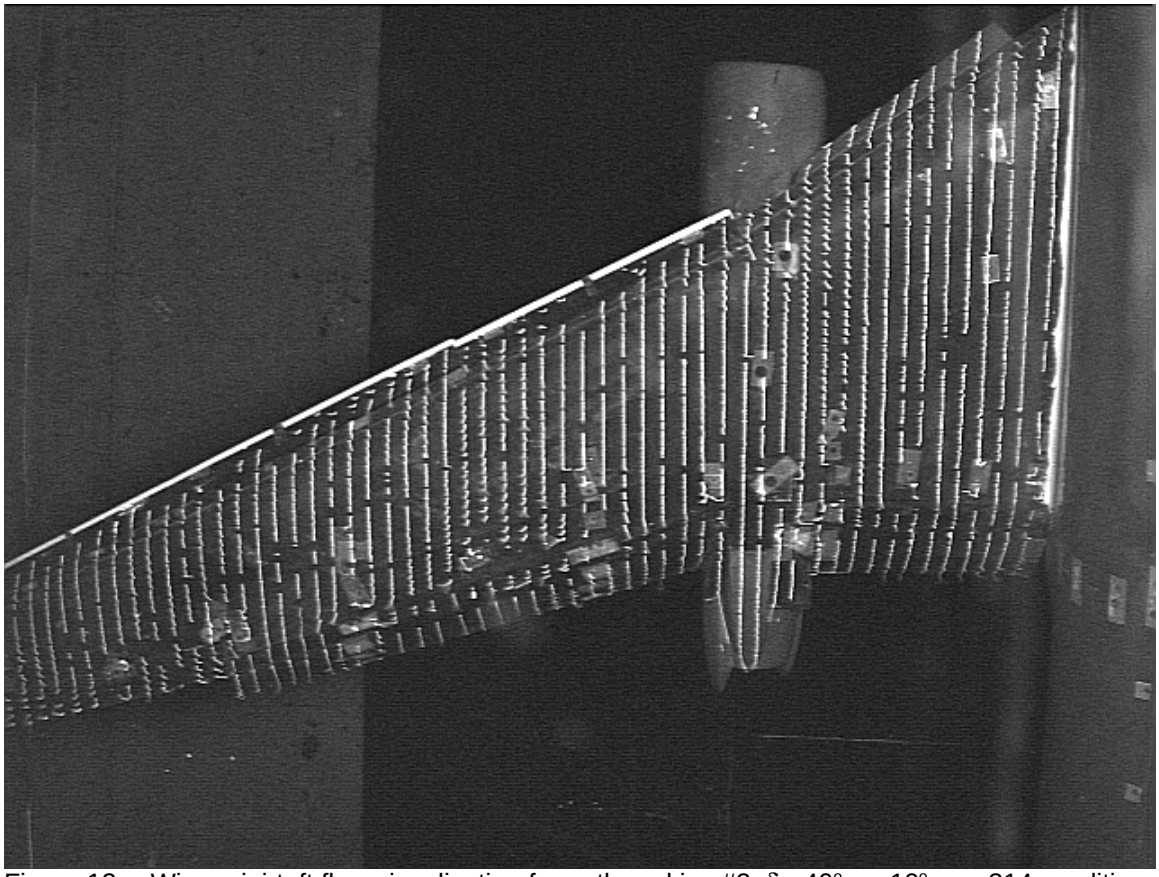

Figure 12.—Wing mini-tuft flow visualization for outboard ice #2, δ_f=40°, α=10°, run 314 condition.

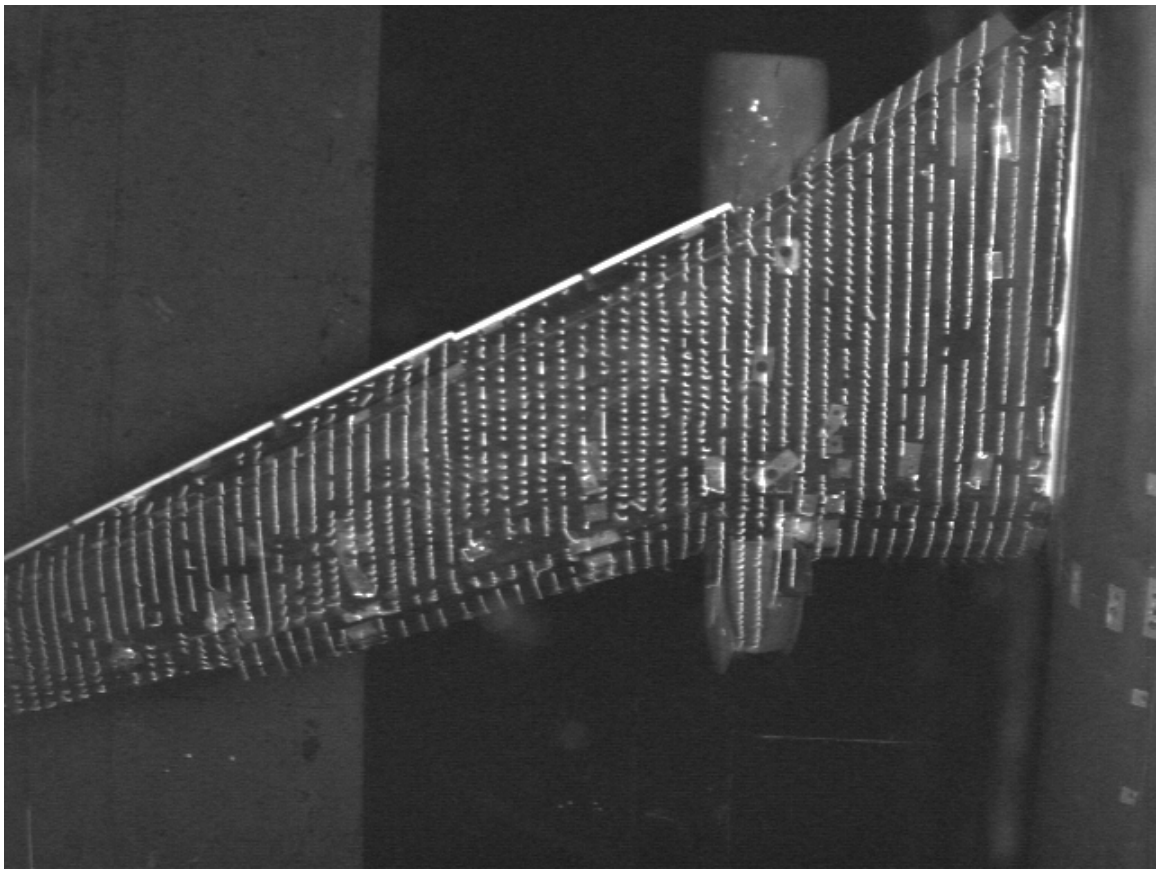

Figure 13.—Wing mini-tuft flow visualization for outboard ice #2, $\delta_f=40^o$, $\alpha=14^o$, run 314 condition.

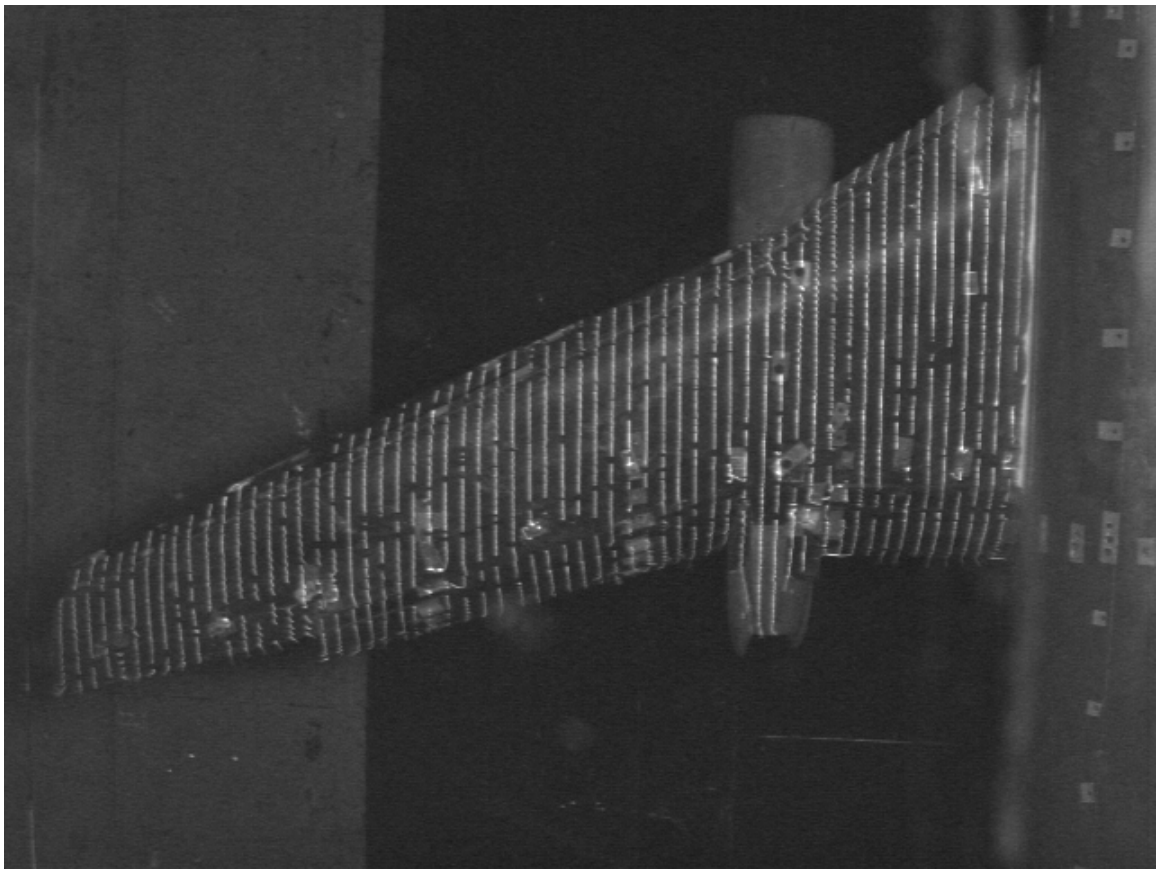

Figure 14.—Wing mini-tuft flow visualization for no ice, $\delta_f=40^o$, $\alpha=4^o$, run 314 condition.

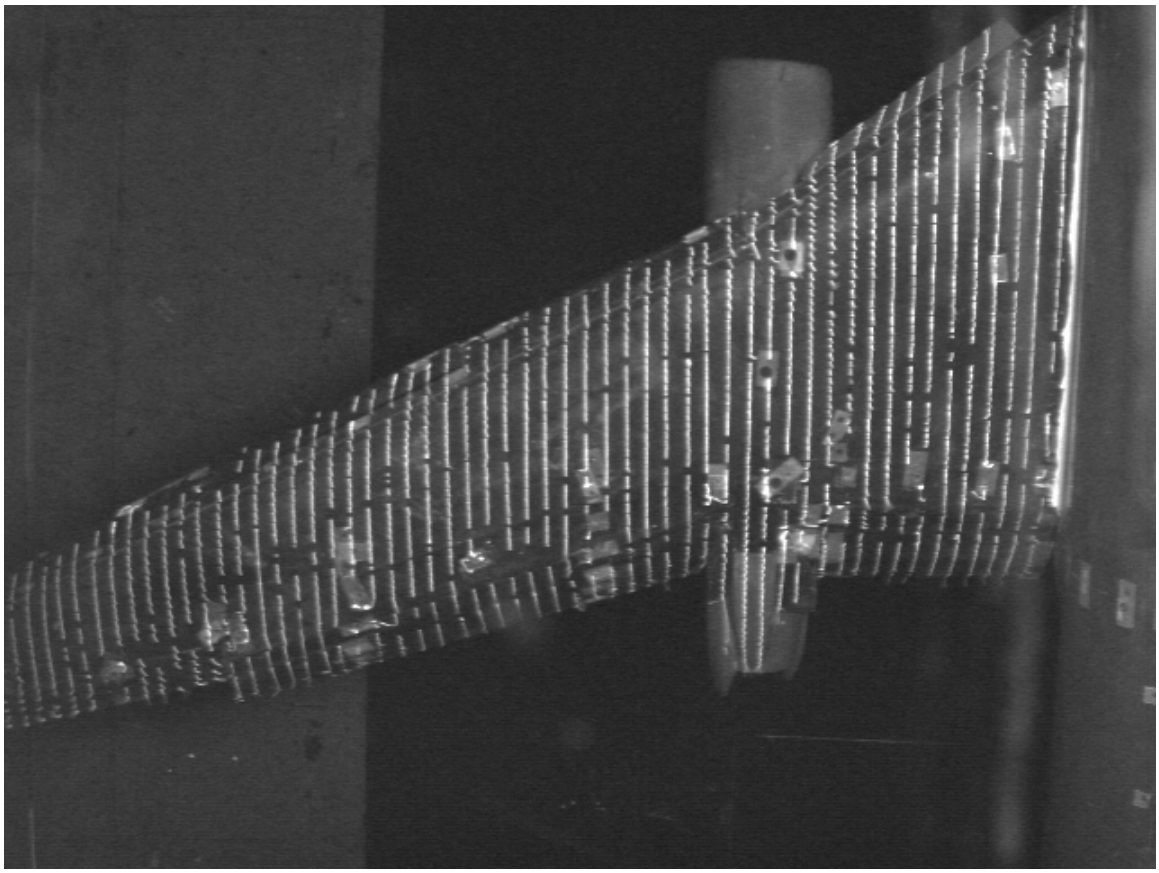

Figure 15.—Wing mini-tuft flow visualization for no ice, δ_f=40°, α=10°, run 314 condition.

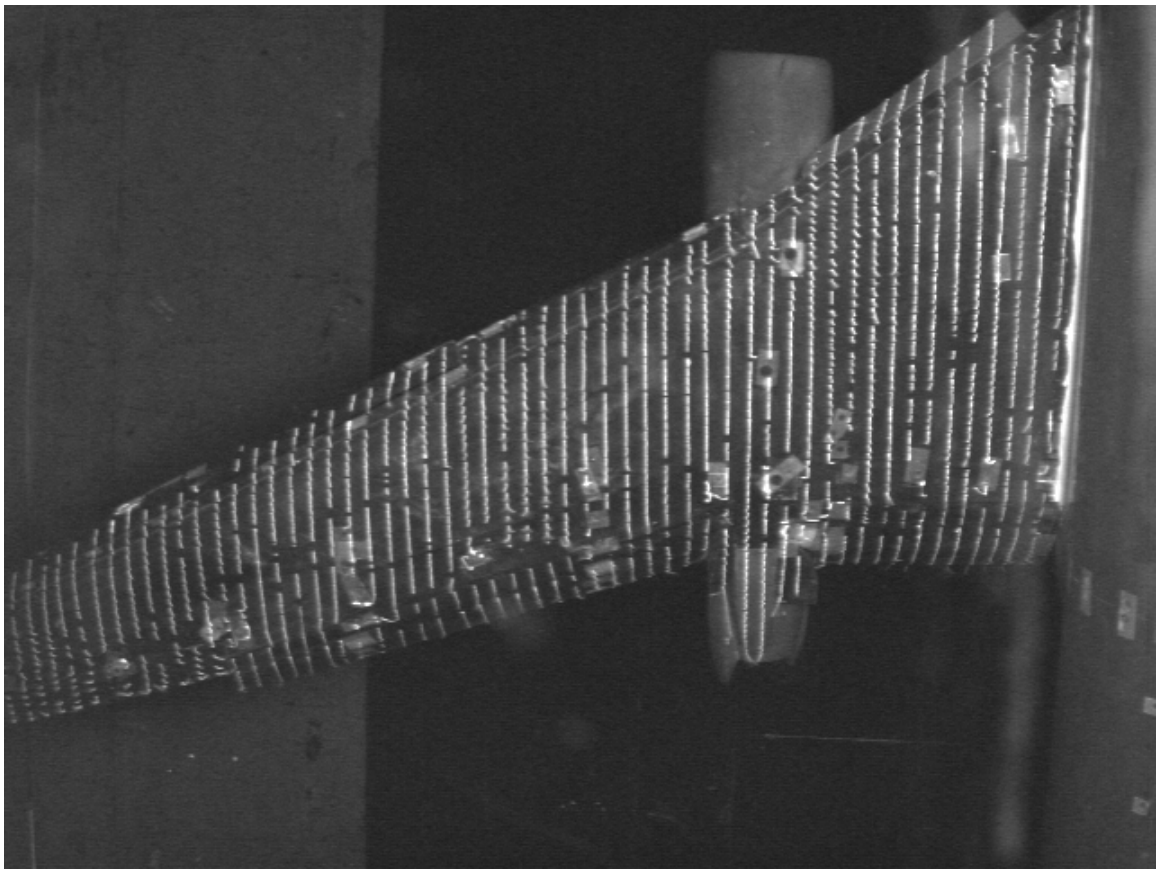

Figure 16.—Wing mini-tuft flow visualization for no ice, δ_f=40°, α=14°, run 314 condition.

Figure 17.—Main wing flow visualization for ice #2, $\delta_f=40^o$, $\alpha=0^o$ condition.

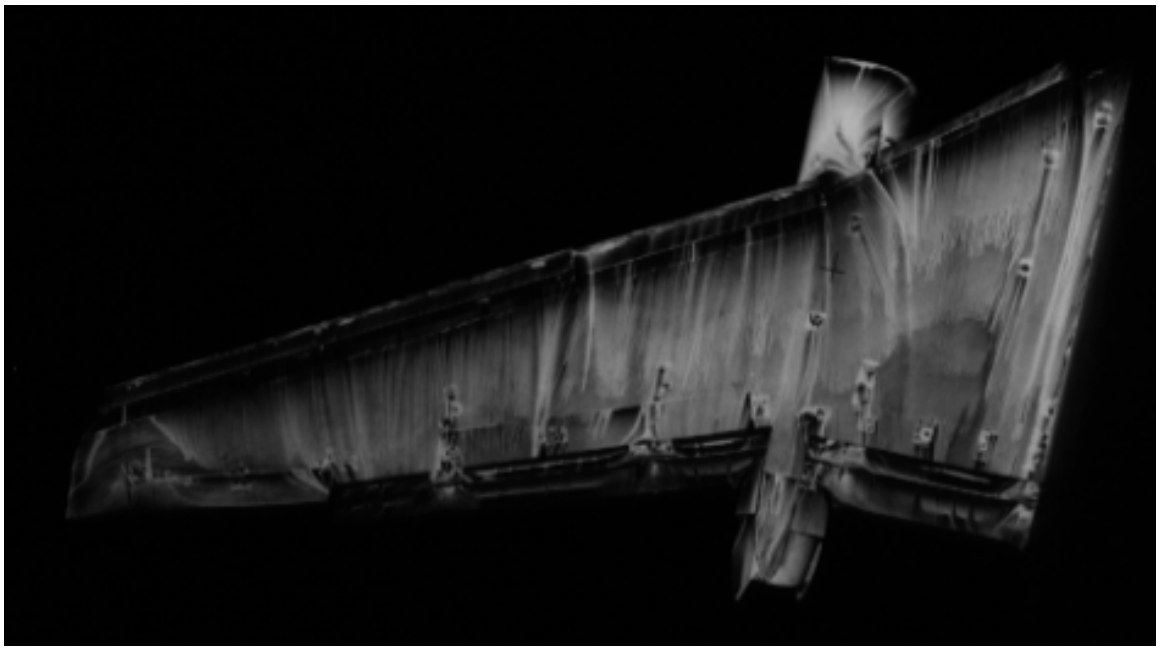

Figure 18.—Main wing flow visualization for ice #2, $\delta_f=40^o$, $\alpha=8^o$ condition.

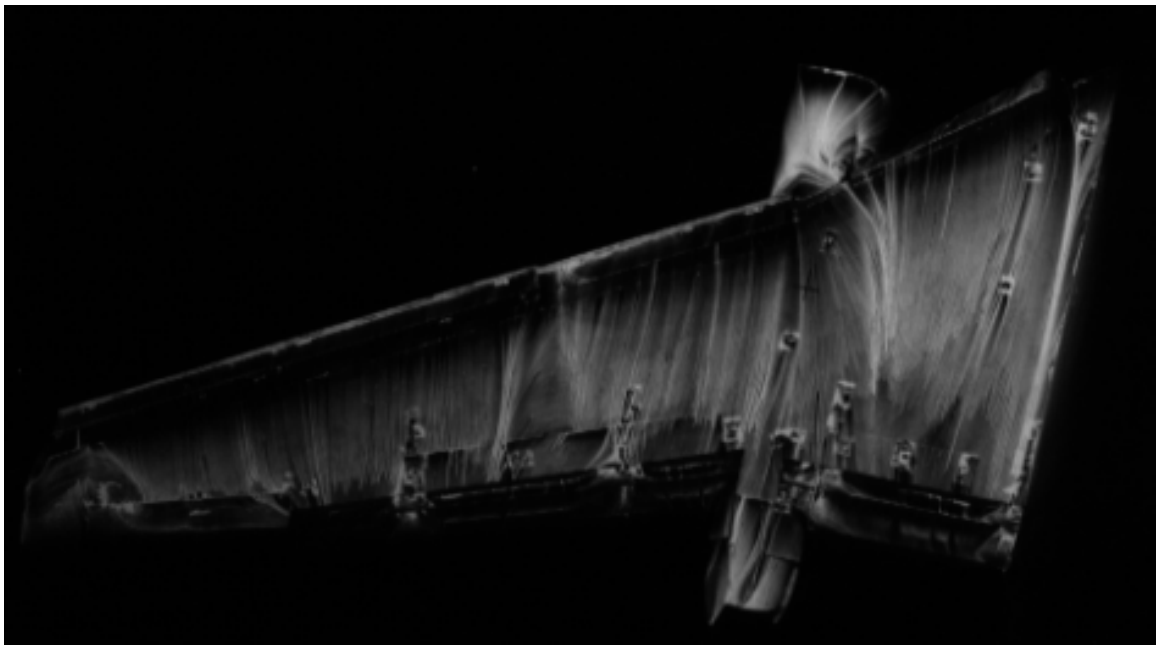

Figure 19.—Main wing flow visualization for ice #2, δ_f=40°, α=10° condition.

Figure 20.—Main wing flow visualization for ice #2, δ_f=40°, α=12° condition.

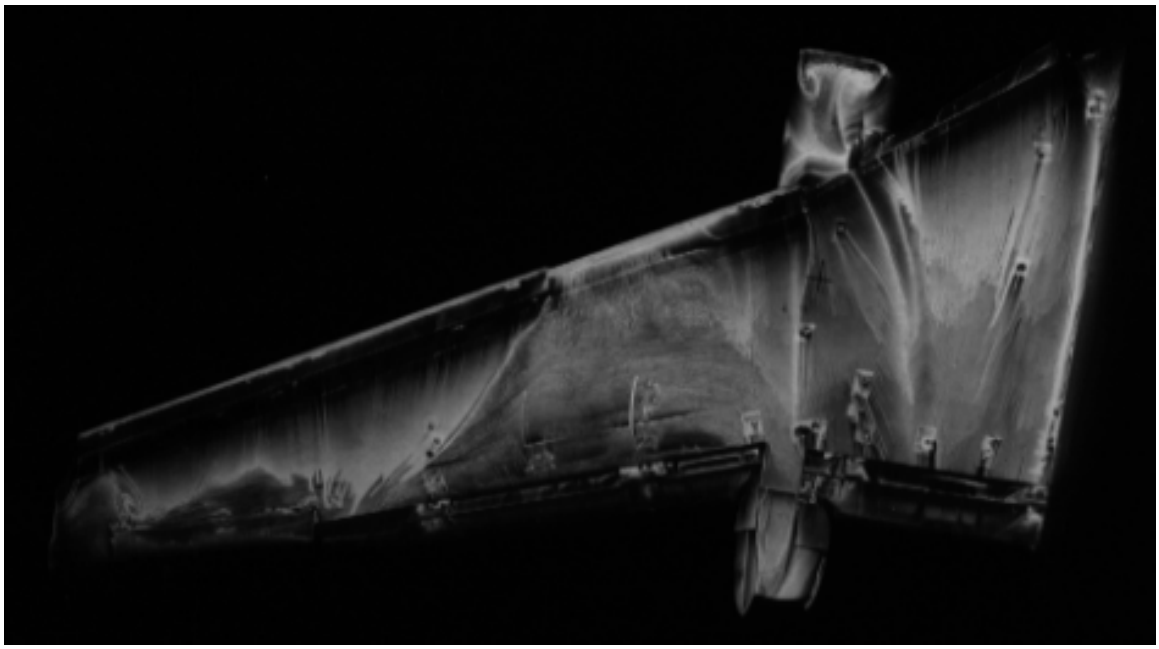

Figure 21.—Main wing flow visualization for ice #2, δ_f=40°, α=13° condition.

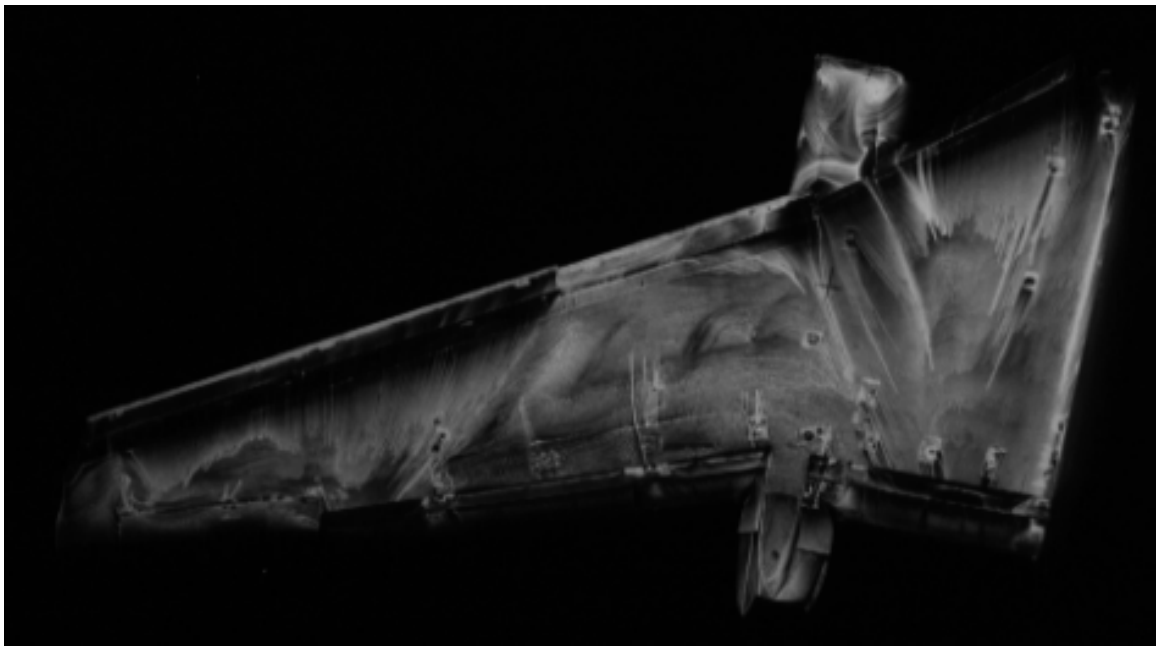

Figure 22.—-Main wing flow visualization for ice #2, δ_f=40°, α=15° condition.

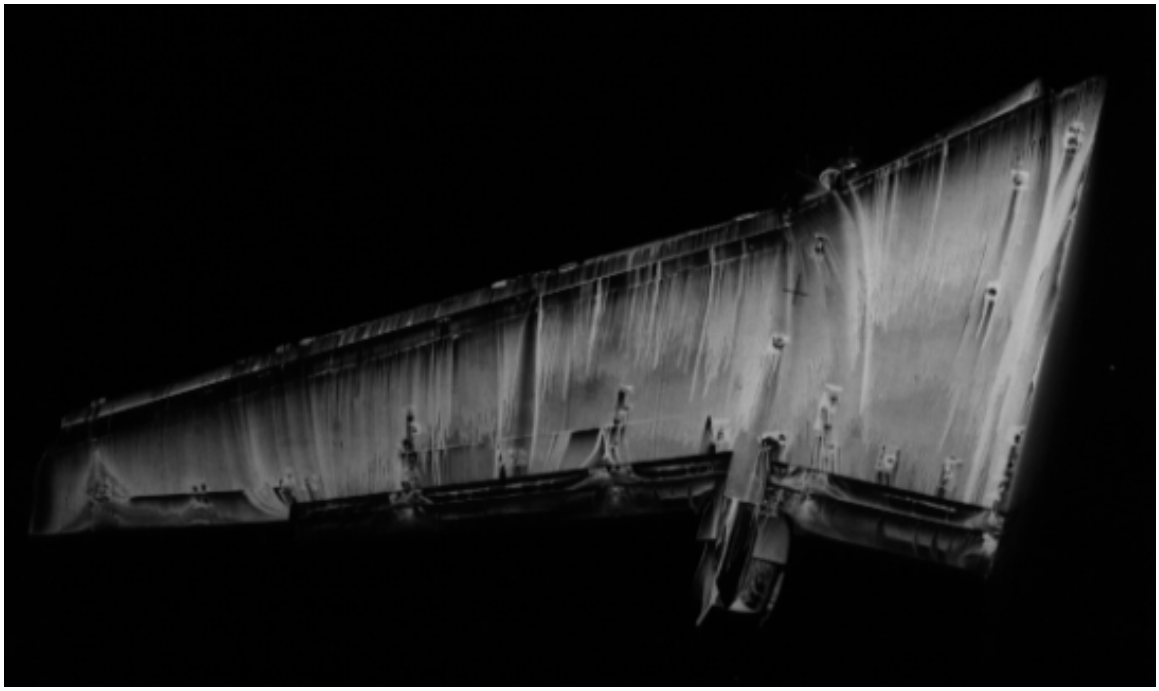

Figure 23.—Main wing flow visualization for no ice, $\delta_f=40^o$, $\alpha=0^o$ condition.

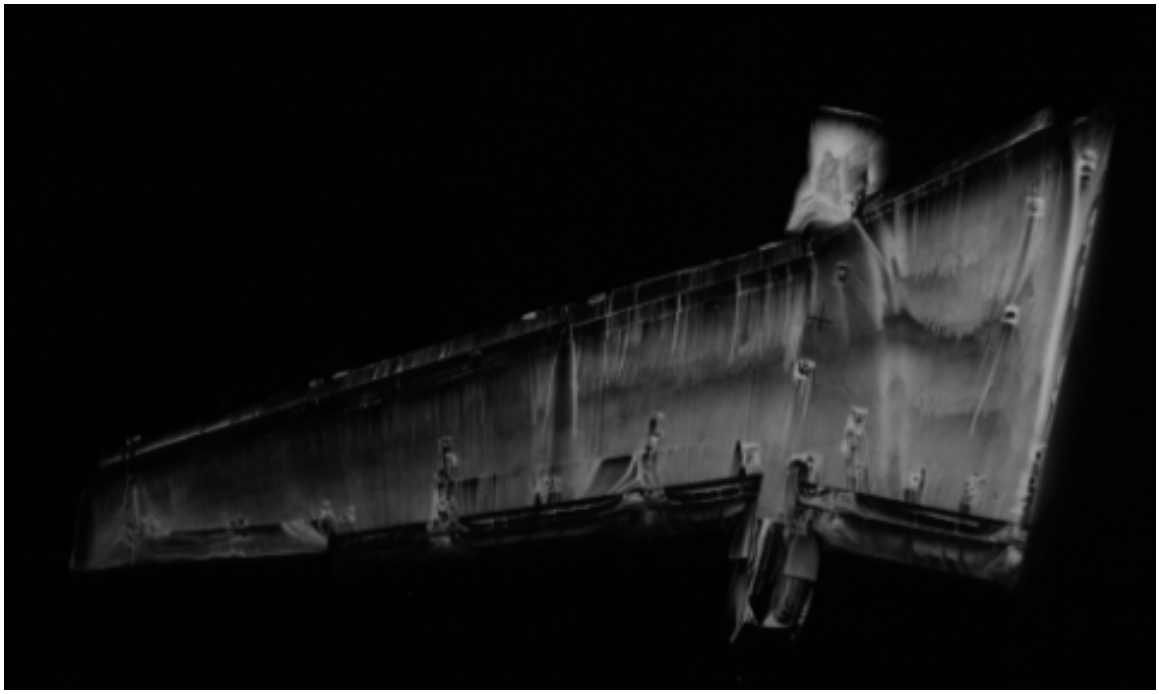

Figure 24.—Main wing flow visualization for no ice, $\delta_f=40^o$, $\alpha=8^o$ condition.

Figure 25.—Main wing flow visualization for no ice, δ_f=40°, α=10° condition.

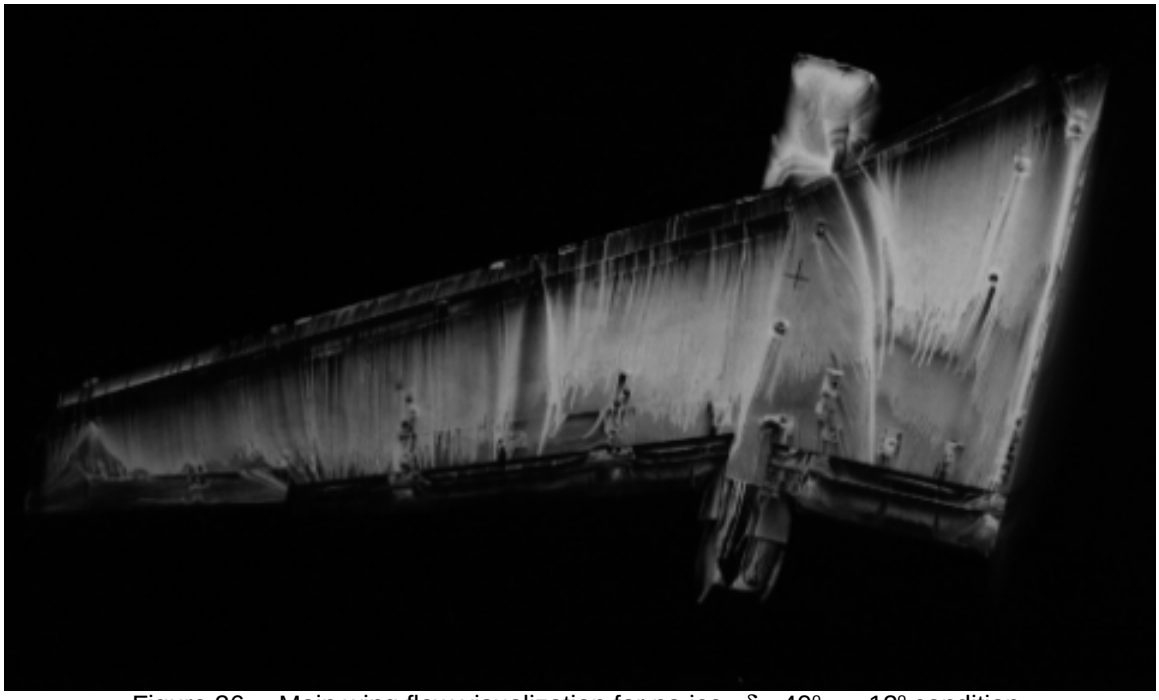

Figure 26.—Main wing flow visualization for no ice, δ_f=40°, α=12° condition.

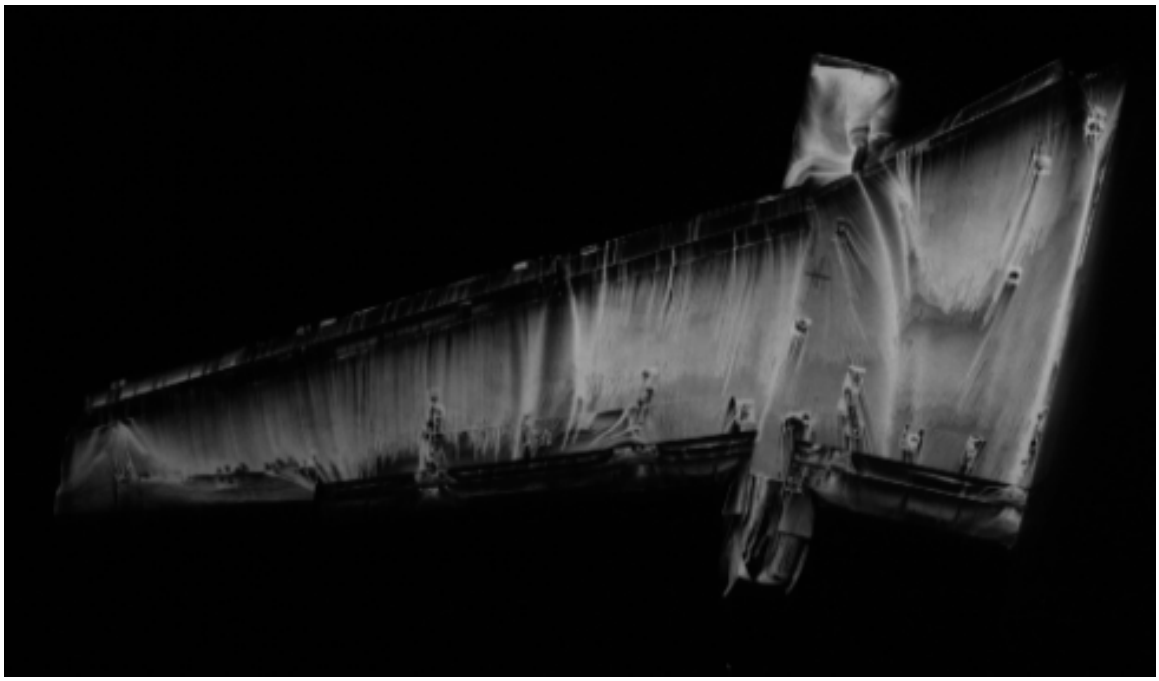

Figure 27.—Main wing flow visualization for no ice, $\delta_f=40^o$, $\alpha=13^o$ condition.

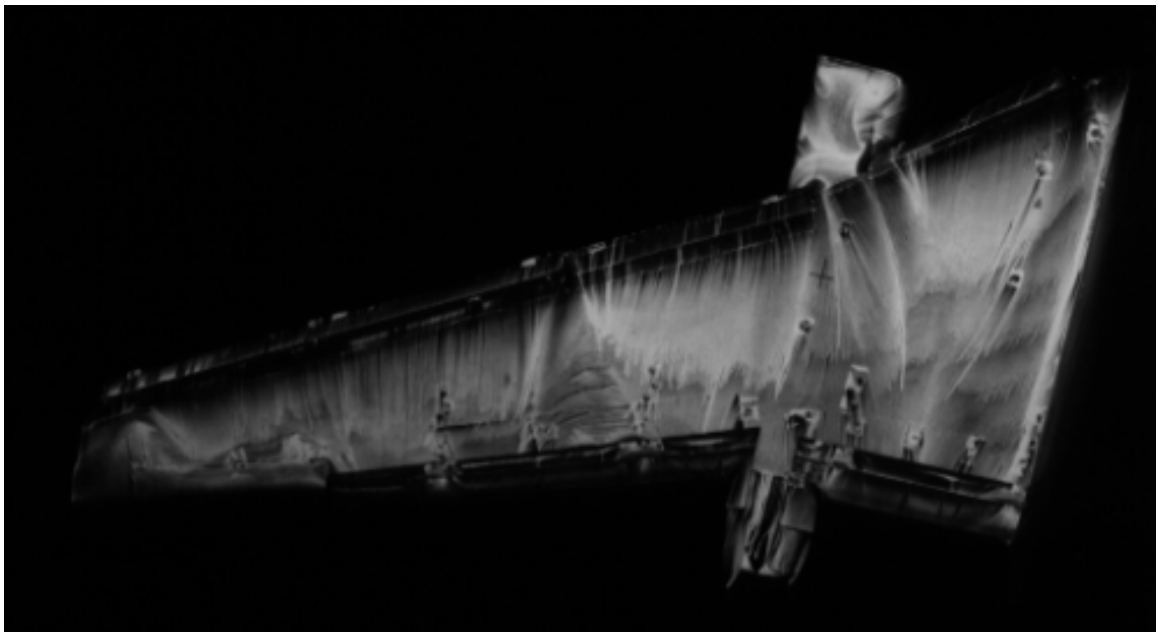

Figure 28.—Main wing flow visualization for no ice, $\delta_f=40^o$, $\alpha=15^o$ condition.

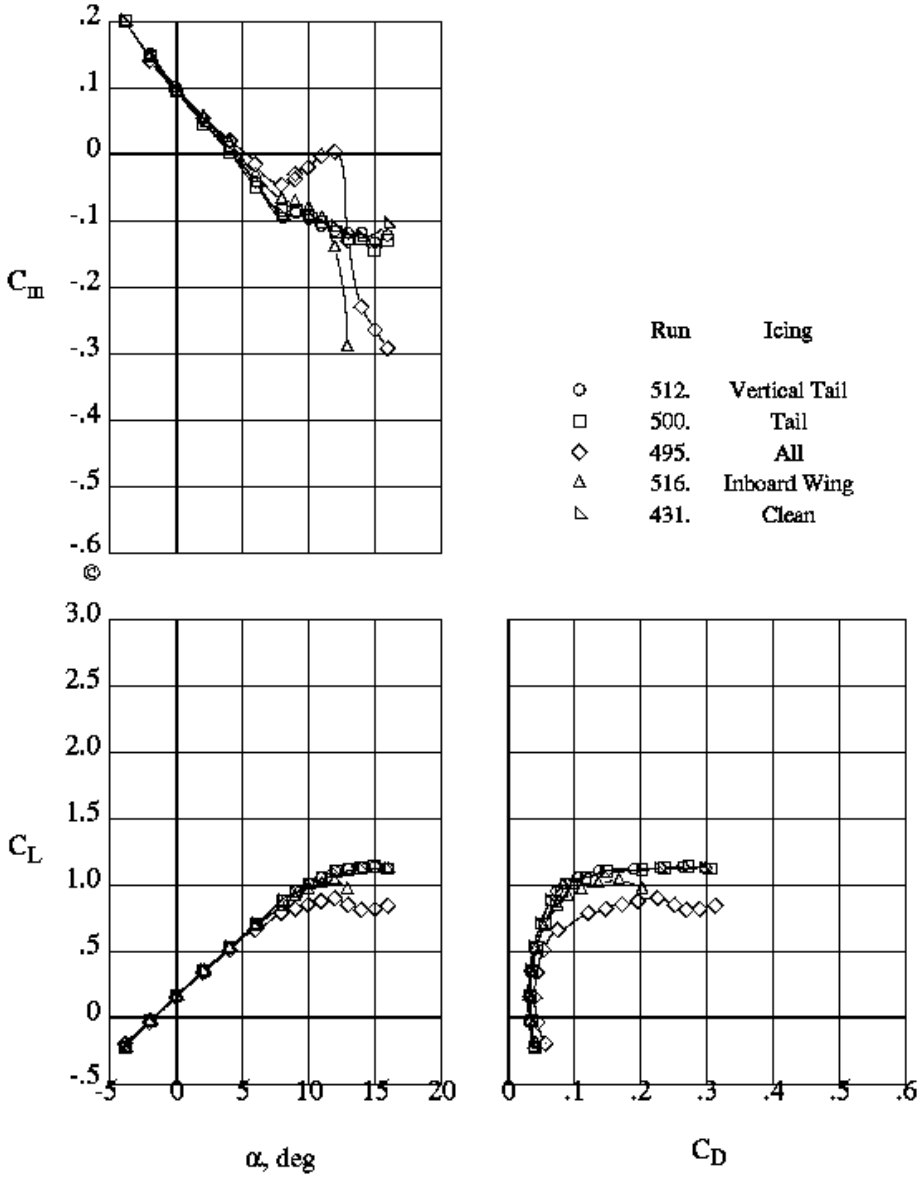

Figure 29.—Effects of Ice #2 on longitudinal aerodynamic characteristics of the model in the cruise configuration.

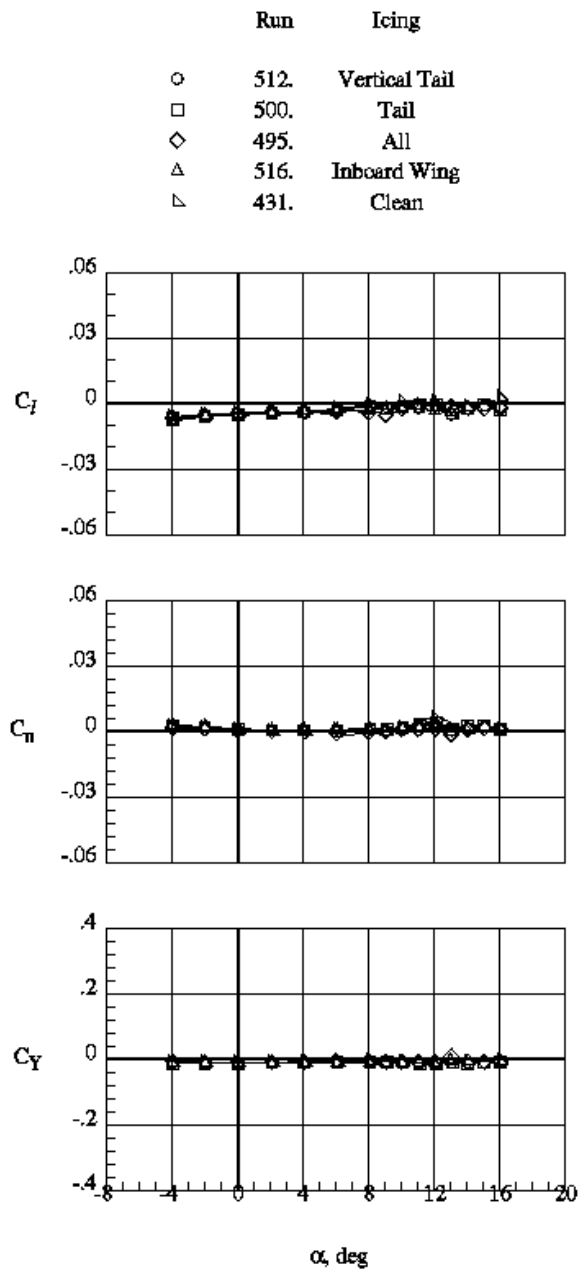

Figure 30.—Effects of Ice #2 and sideslip on the lateral aerodynamic characteristics of the model in the cruise configuration.

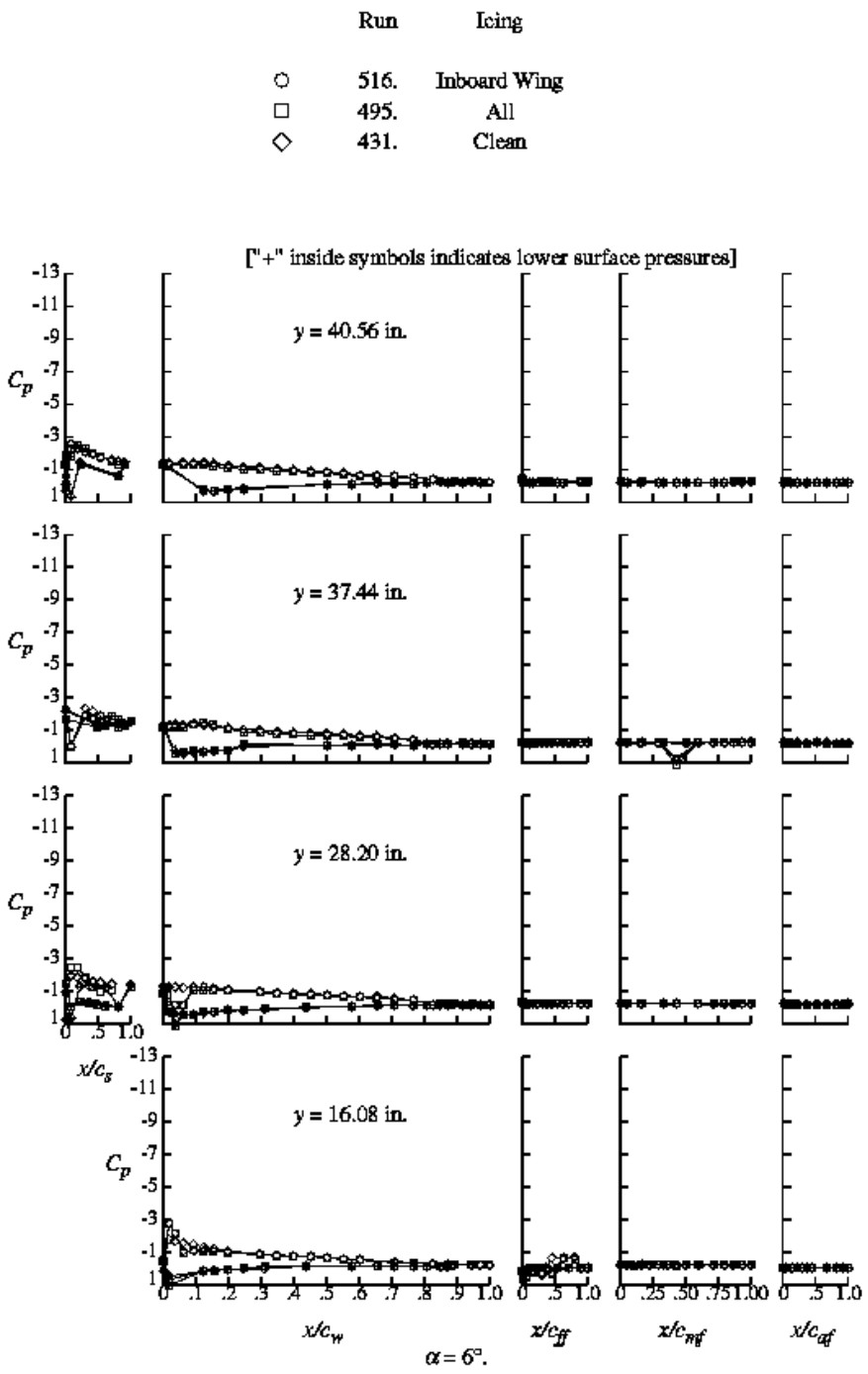

Figure 31.—Effect of Ice #2 on the wing pressure distribution for the model in the cruise configuration.

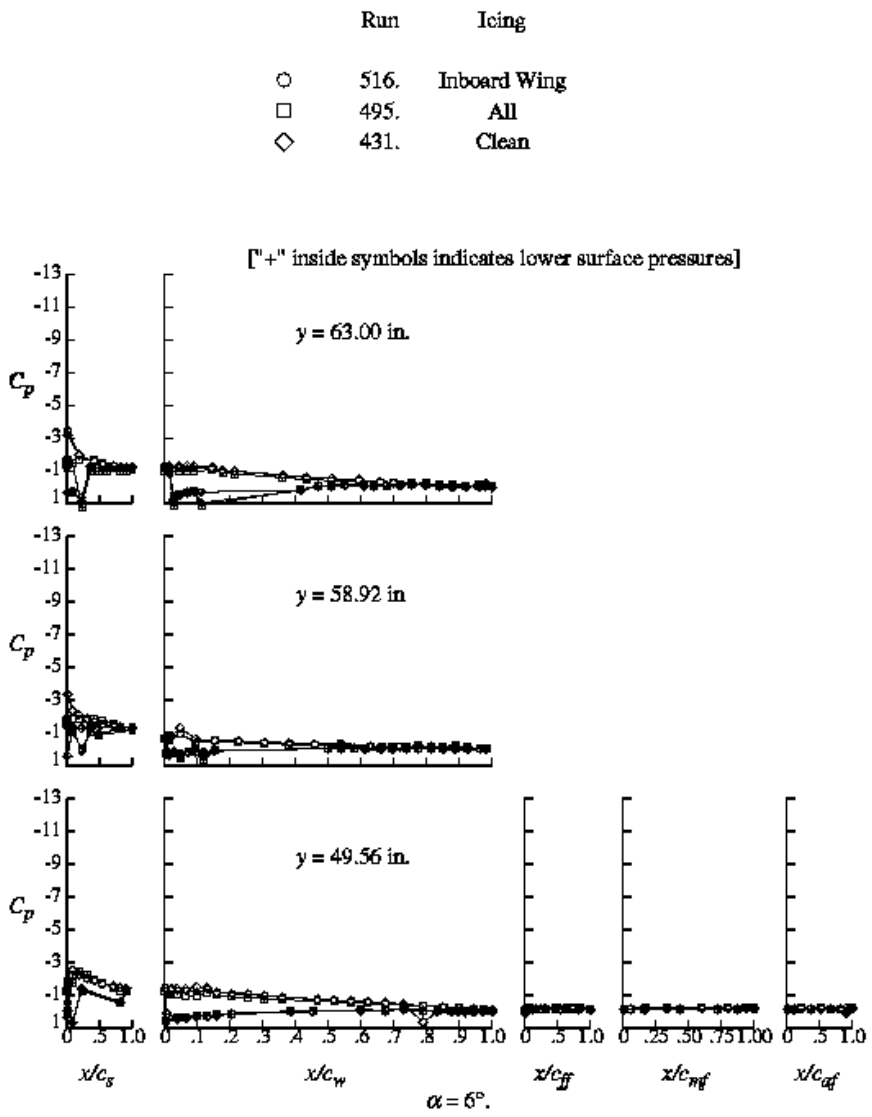

Figure 31(concluded).—Effect of Ice #2 on the wing pressure distribution for the model in the cruise configuration.

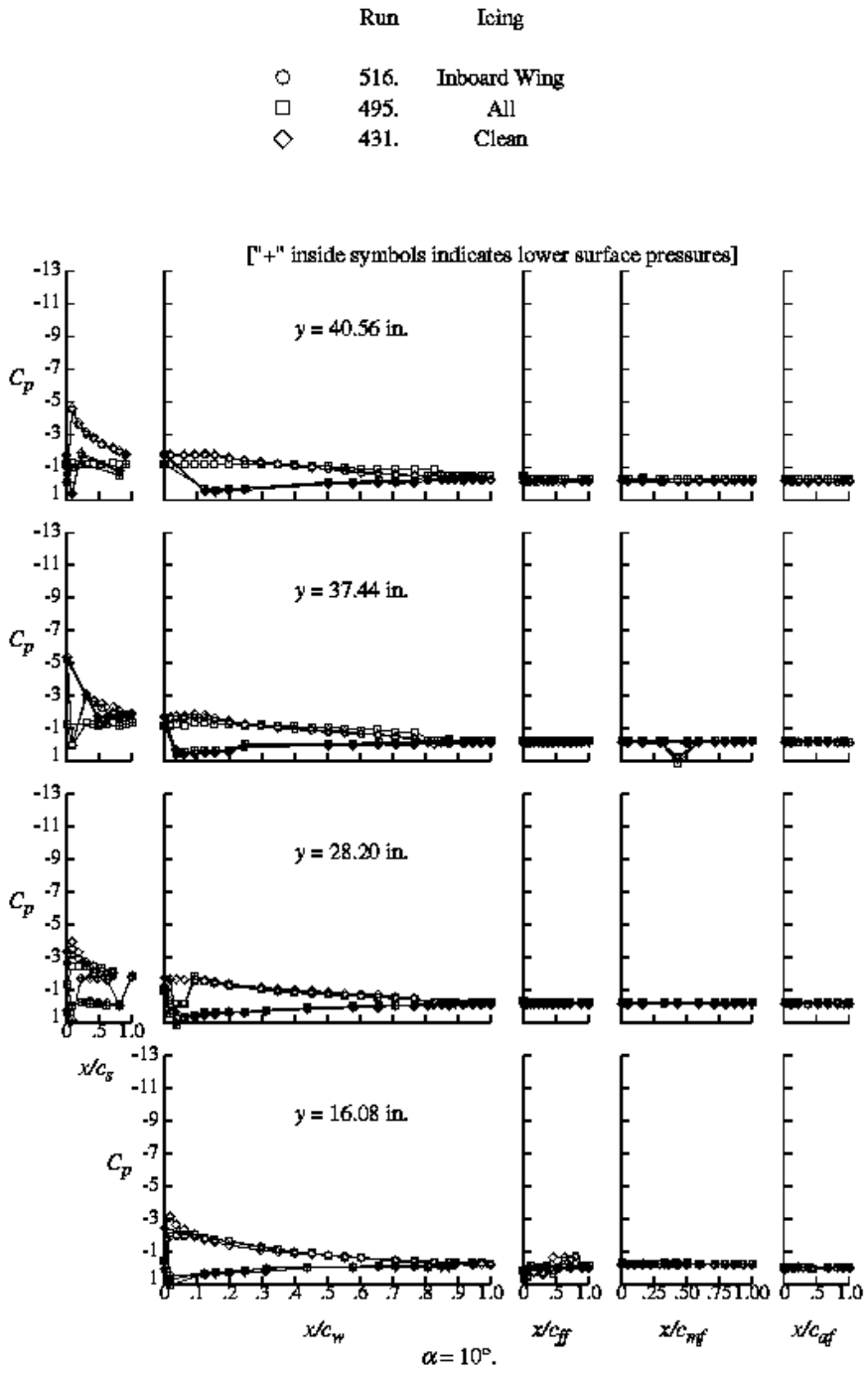

Figure 32.—Effect of Ice #2 on the wing pressure distribution for the model in the cruise configuration.

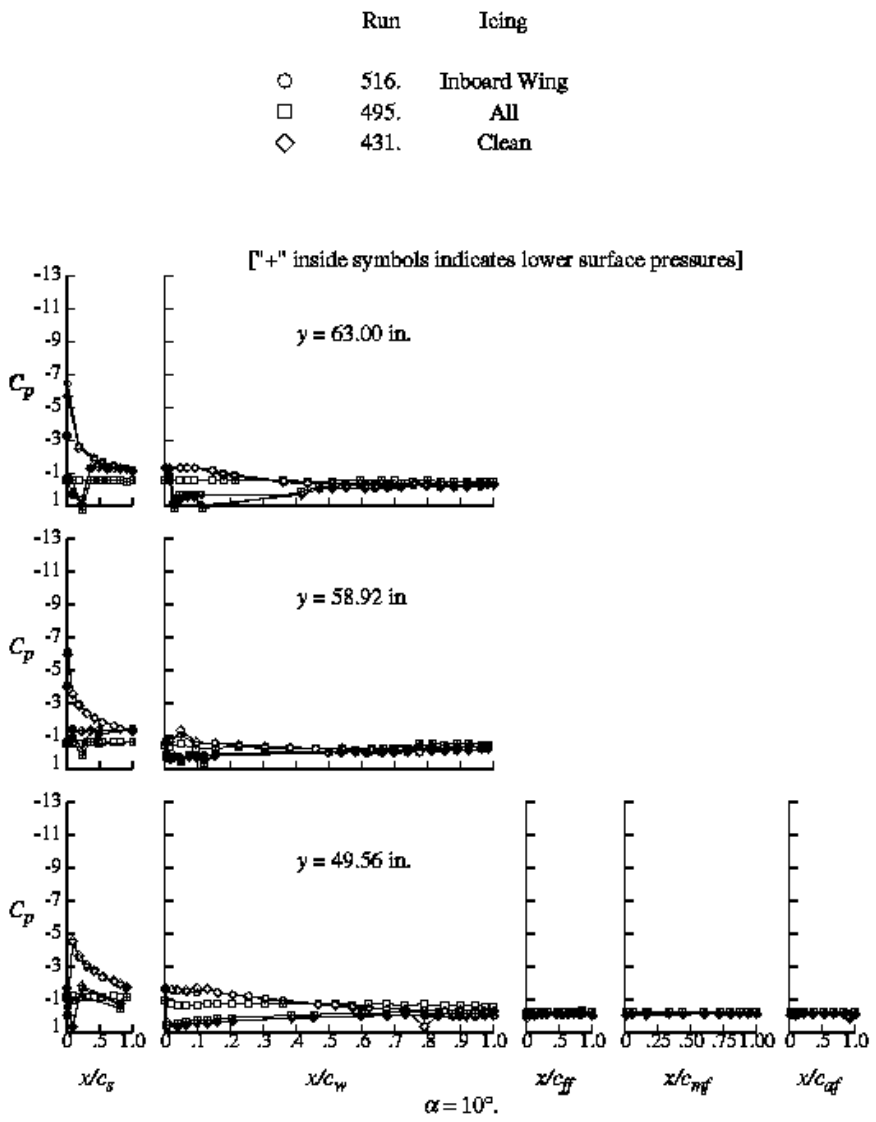

Figure 32 (concluded).—Effect of Ice #2 on the wing pressure distribution for the model in the cruise configuration.

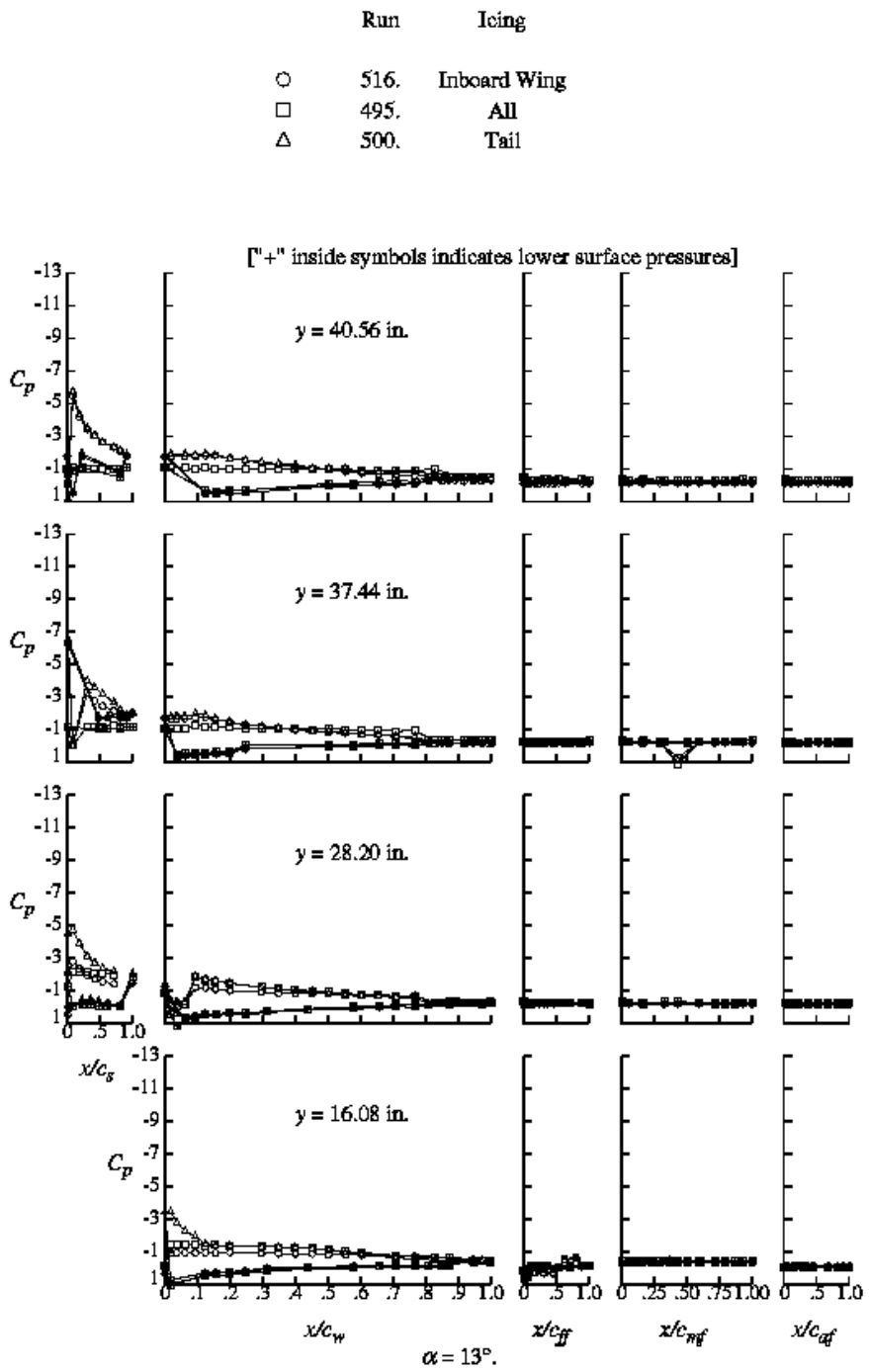

Figure 33.—Effect of Ice #2 on the wing pressure distribution for the model in the cruise configuration.

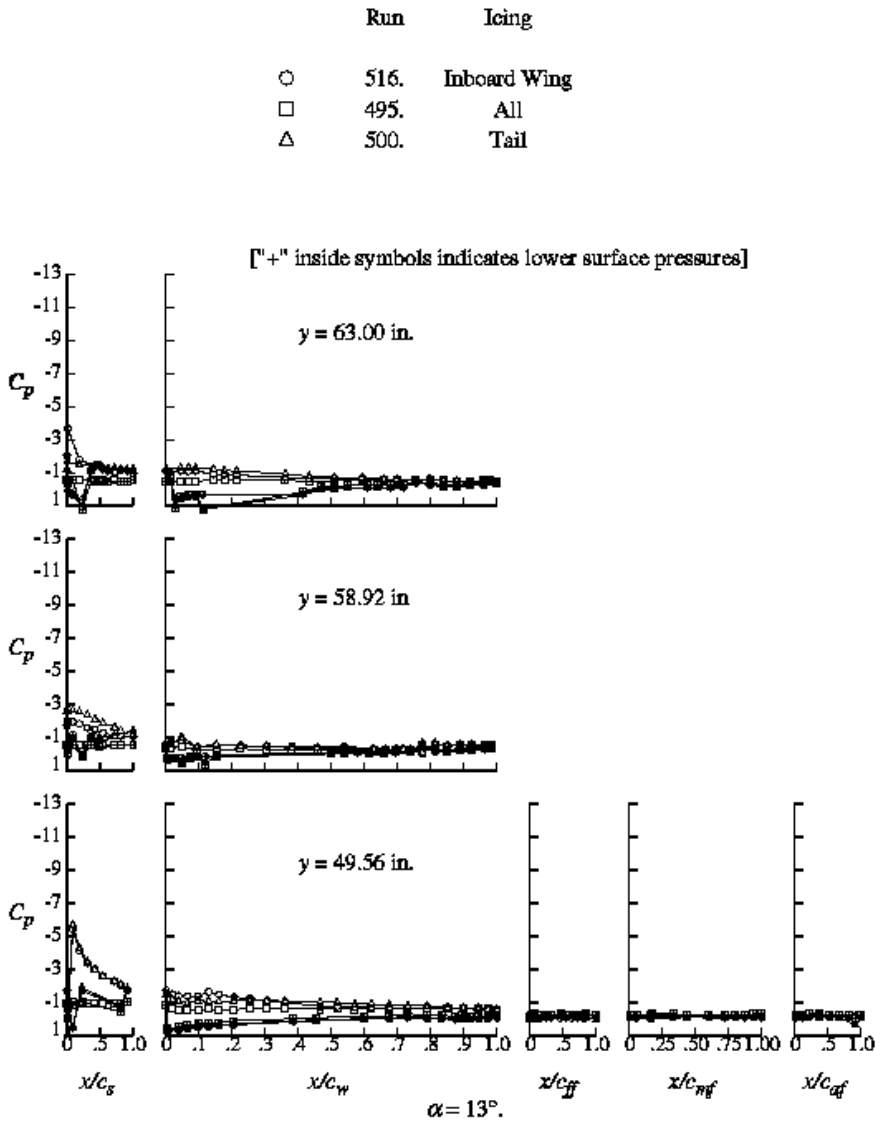

Figure 33 (concluded).—Effect of Ice #2 on the wing pressure distribution for the model in the cruise configuration.

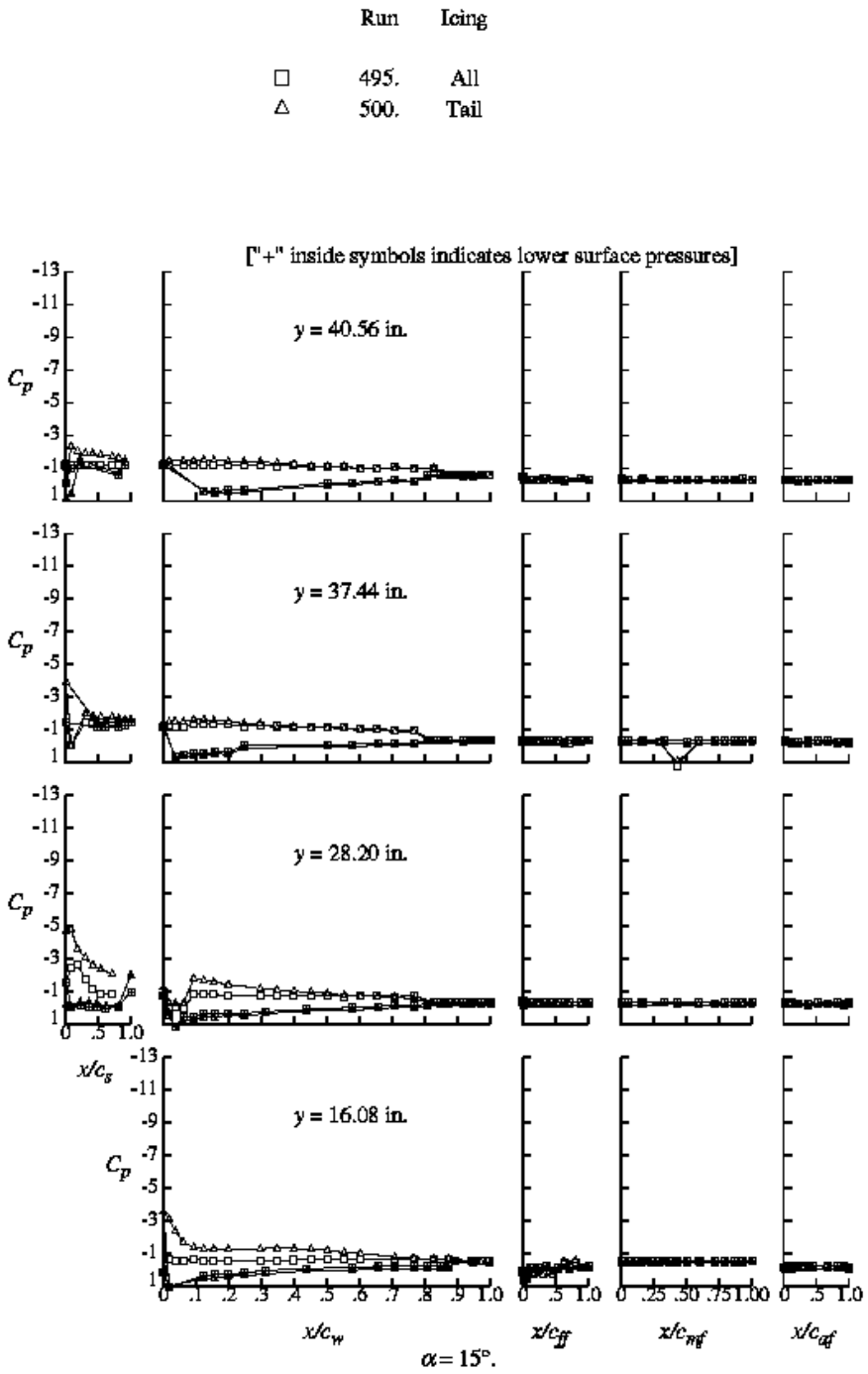

Figure 34.—Effect of Ice #2 on the wing pressure distribution for the model in the cruise configuration.

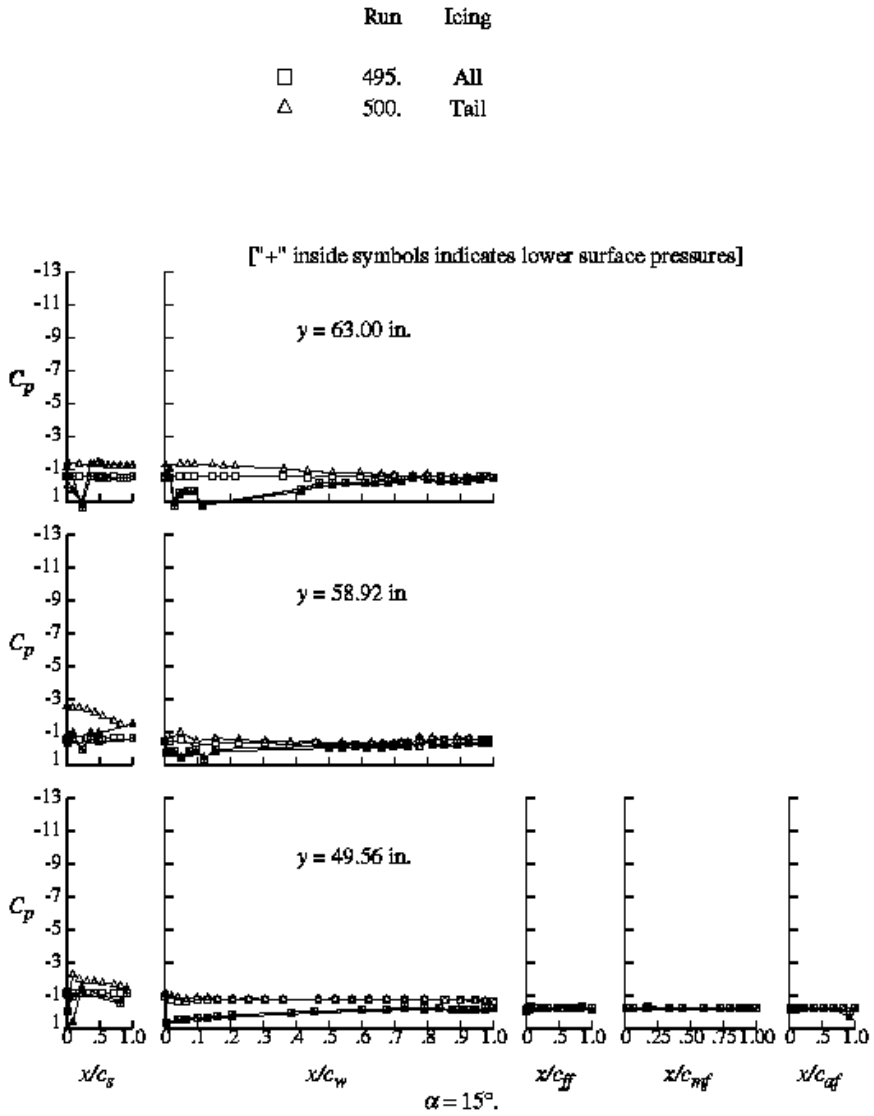

Figure 34 (concluded).—Effect of Ice #2 on the wing pressure distribution for the model in the cruise configuration.

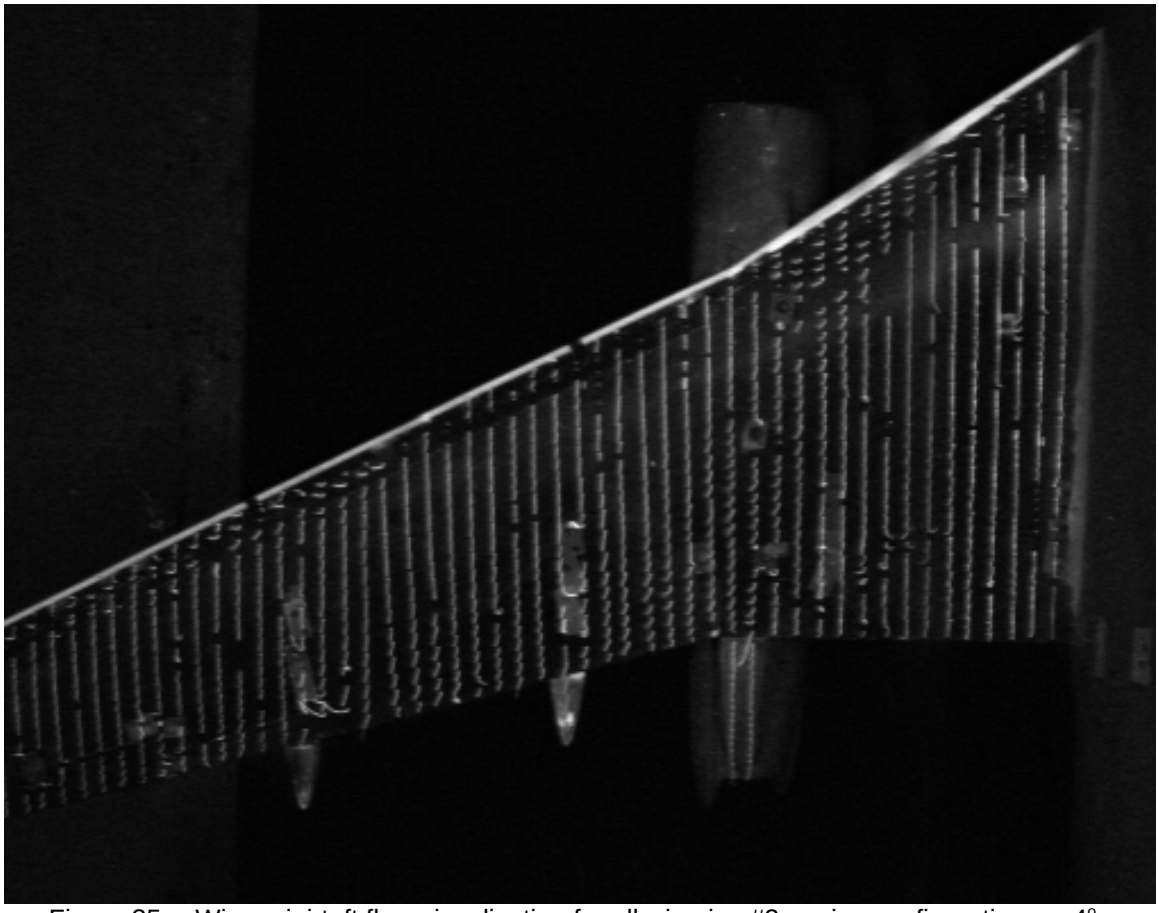

Figure 35.—Wing mini-tuft flow visualization for all wing ice #2, cruise configuration, α=4°, run 495 condition.

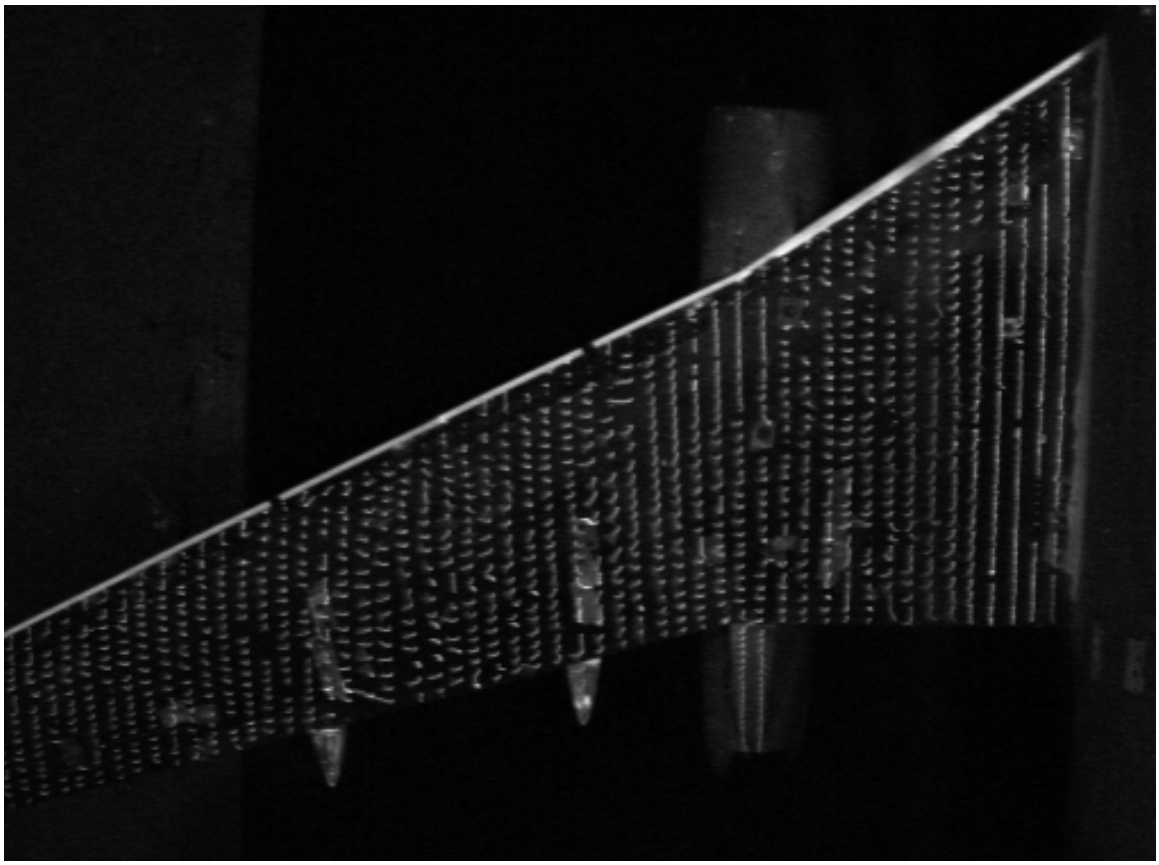

Figure 36.—Wing mini-tuft flow visualization for all wing ice #2, cruise configuration, $\alpha=10^{o}$, run 495 condition.

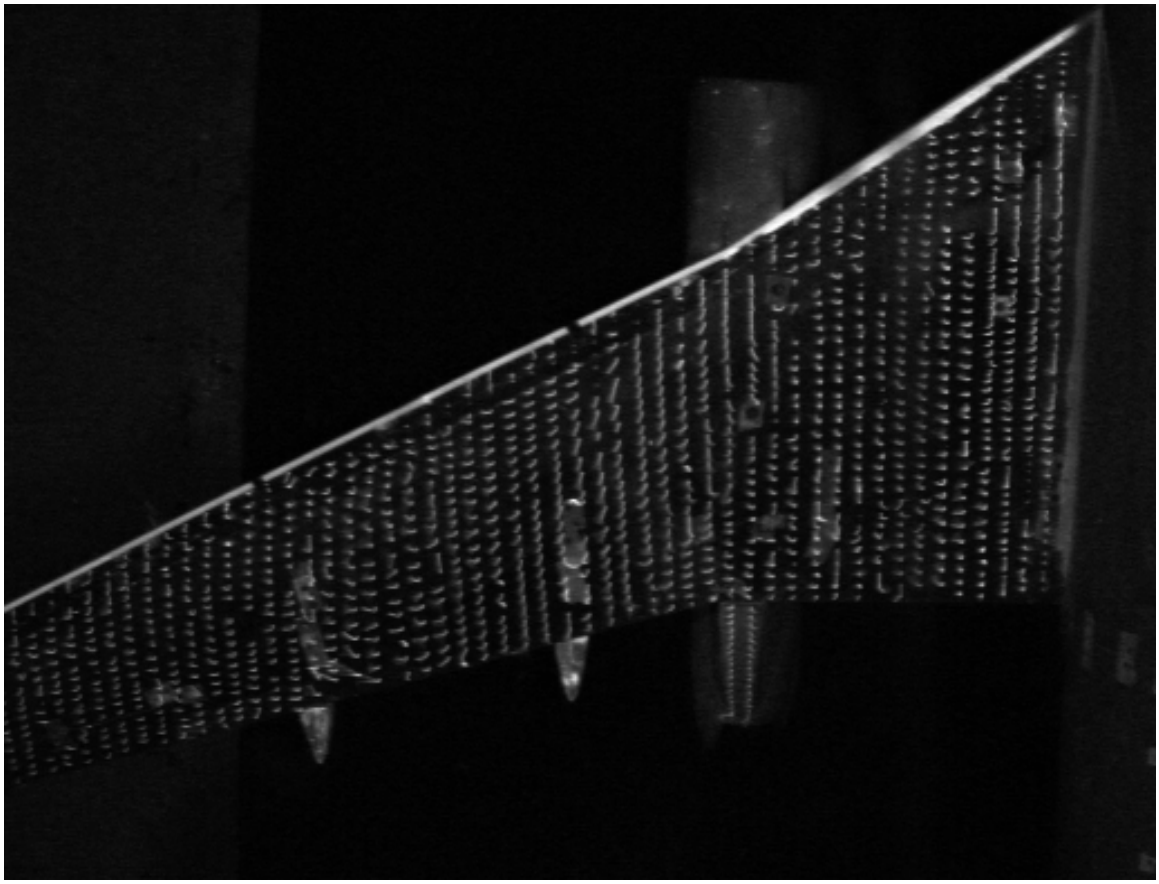

Figure 37.—Wing mini-tuft flow visualization for all wing ice #2, cruise configuration, α =14^{o}, run 495 condition.

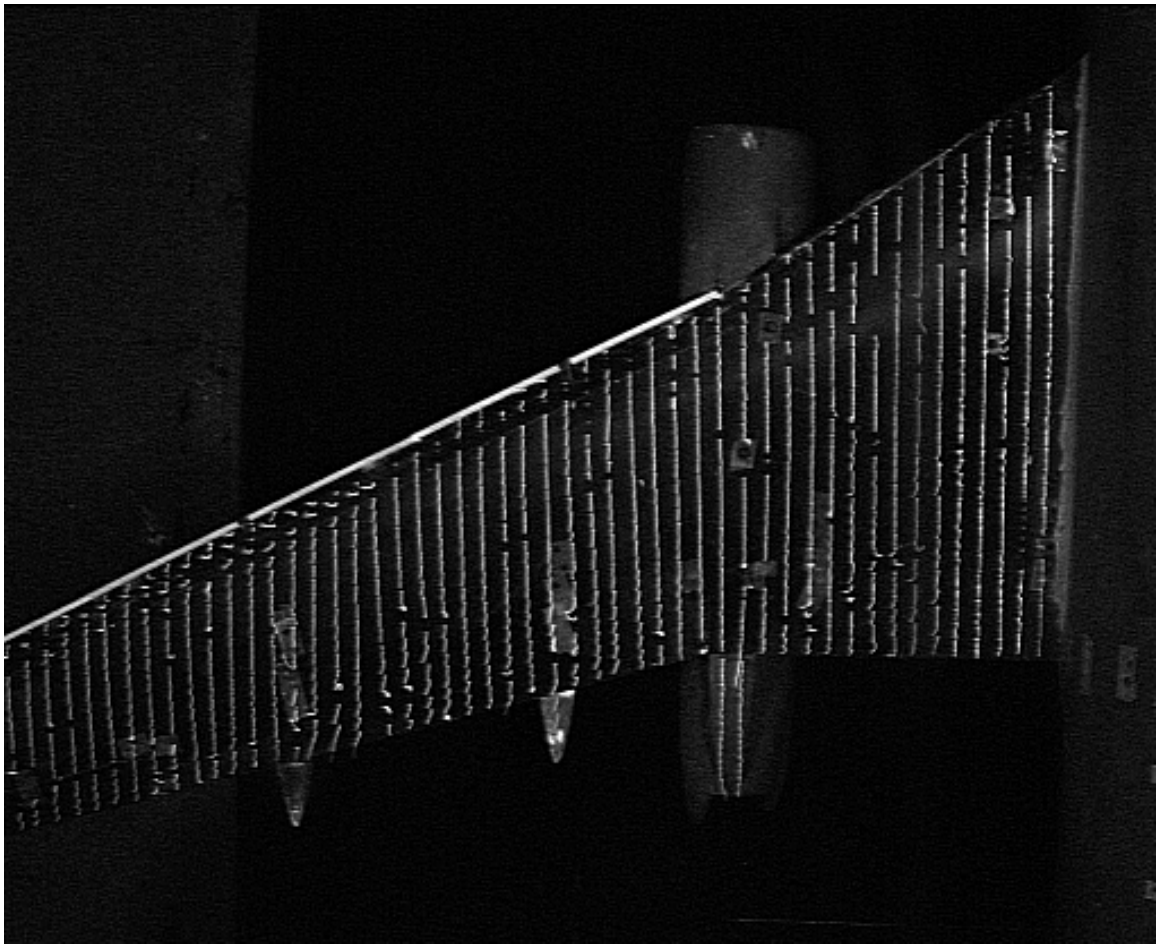

Figure 38.—Wing mini-tuft flow visualization for outboard ice #2, cruise configuration, $\alpha = 4^{o}$, run 486 condition.

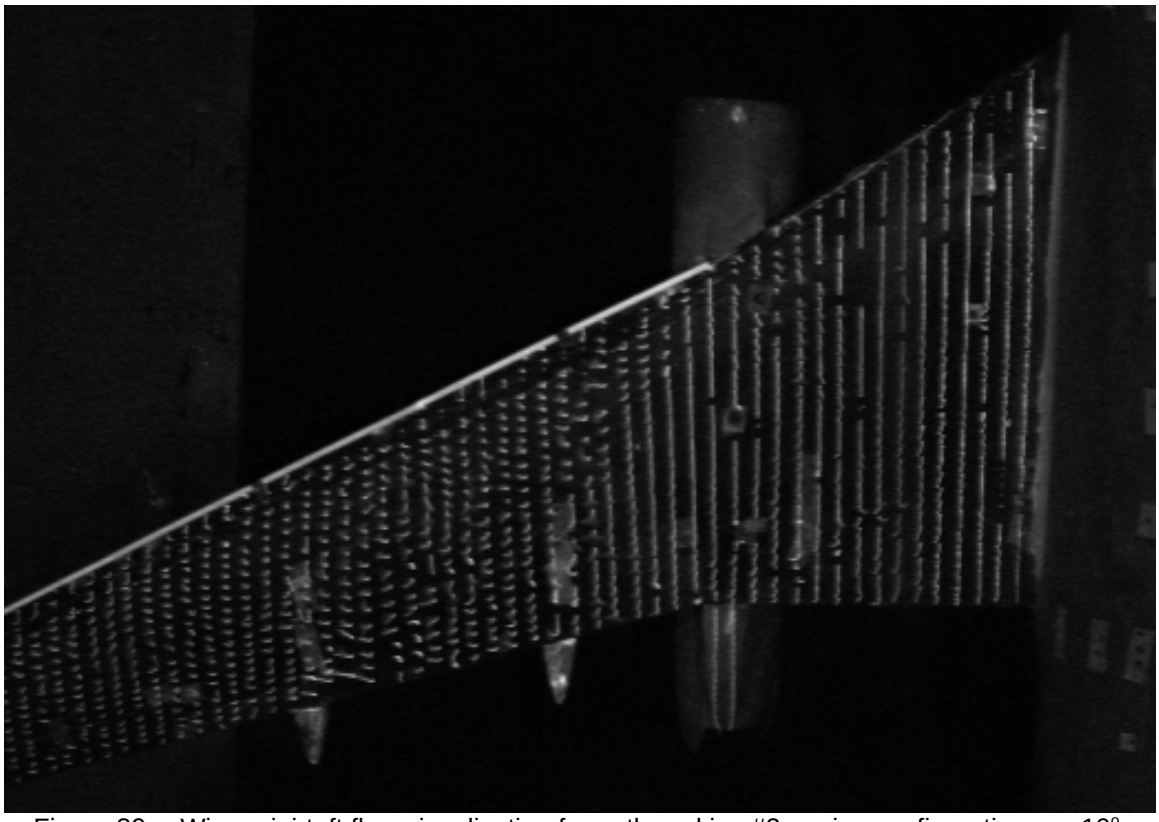

Figure 39.—Wing mini-tuft flow visualization for outboard ice #2, cruise configuration, $\alpha = 10^{o}$, run 486 condition.

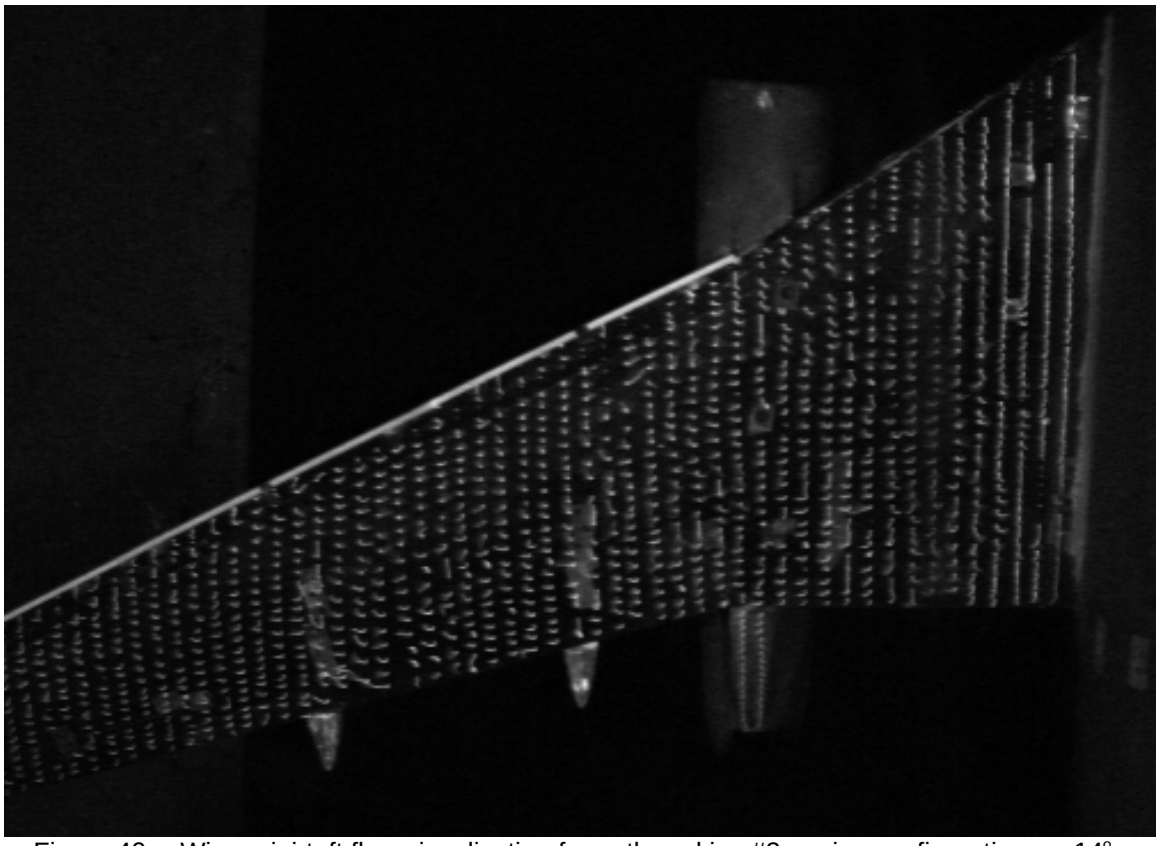

Figure 40.—Wing mini-tuft flow visualization for outboard ice #2, cruise configuration, α=14^{o}, run 486 condition.

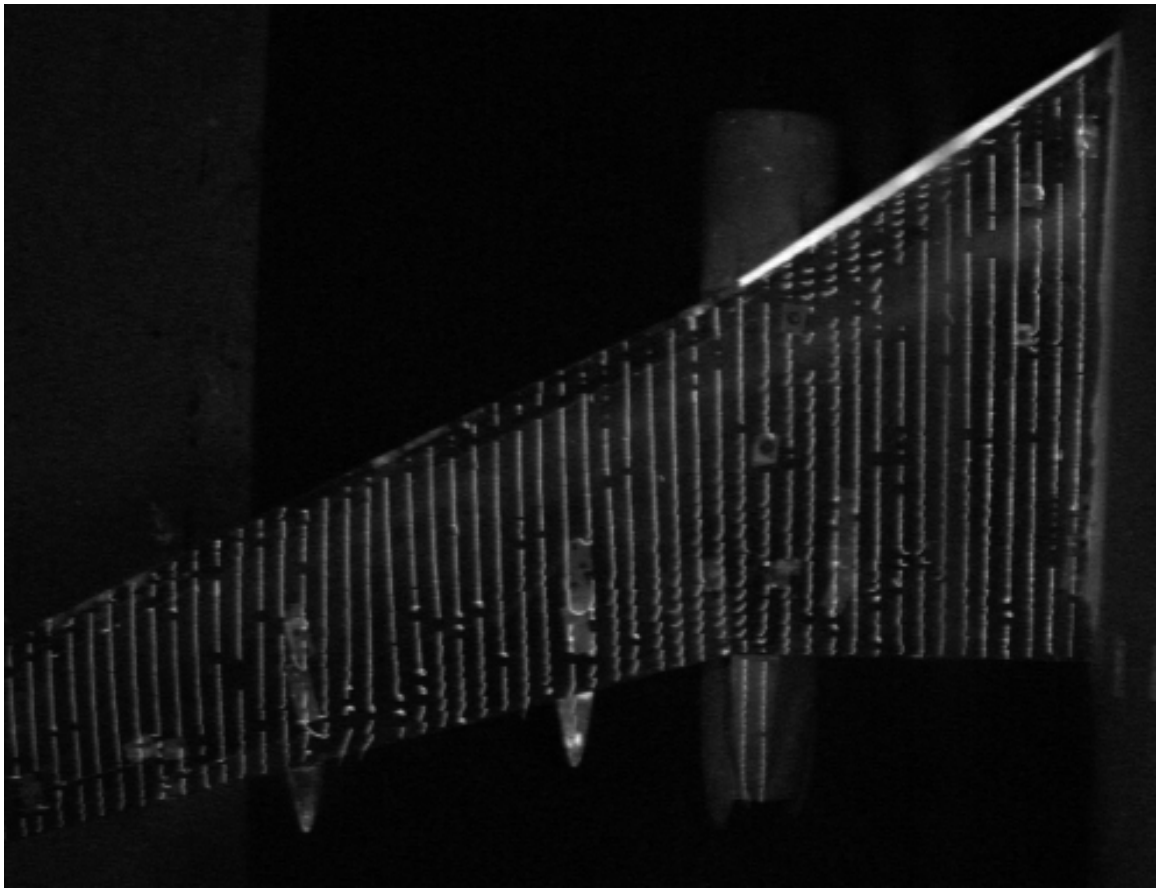

Figure 41.—Wing mini-tuft flow visualization for inboard ice #2, cruise configuration, $\alpha = 4^{o}$, run 516 condition.

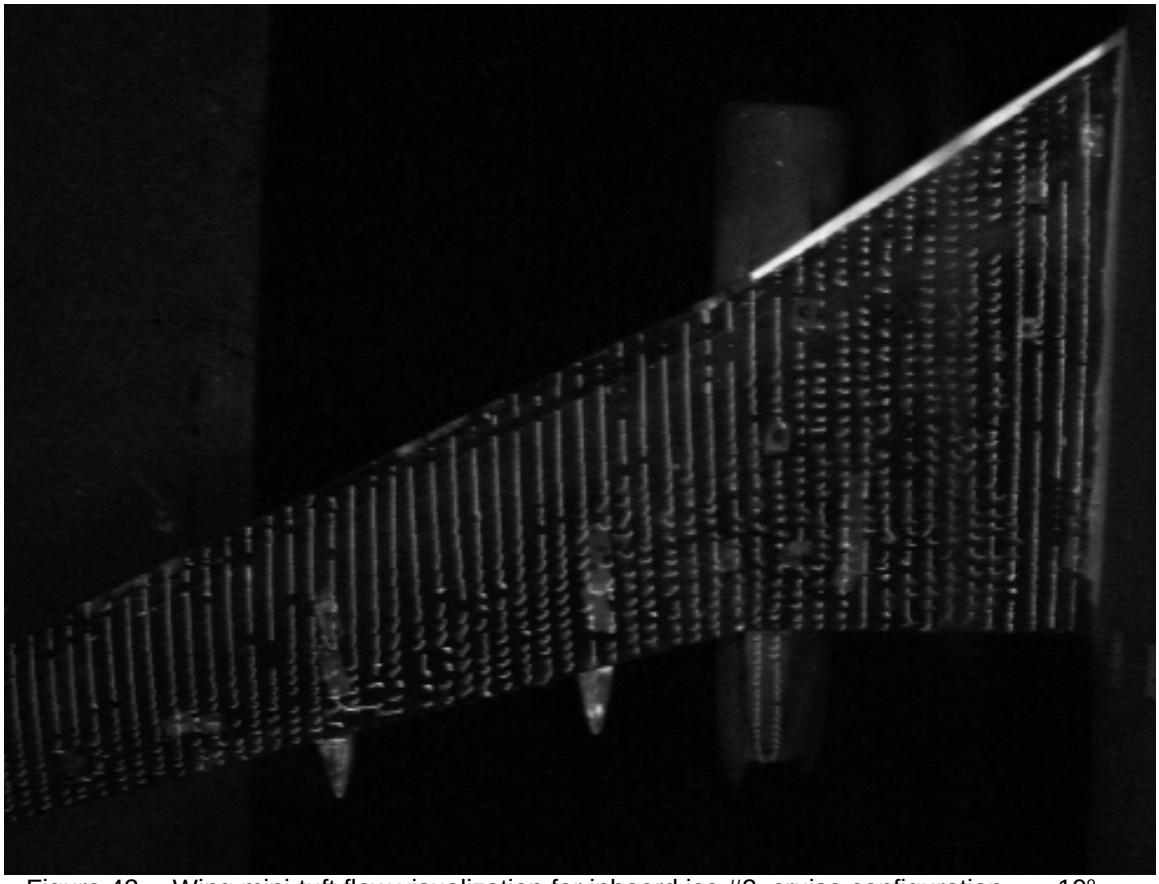

Figure 42.—Wing mini-tuft flow visualization for inboard ice #2, cruise configuration, $\alpha = 10^{o}$, run 516 condition.

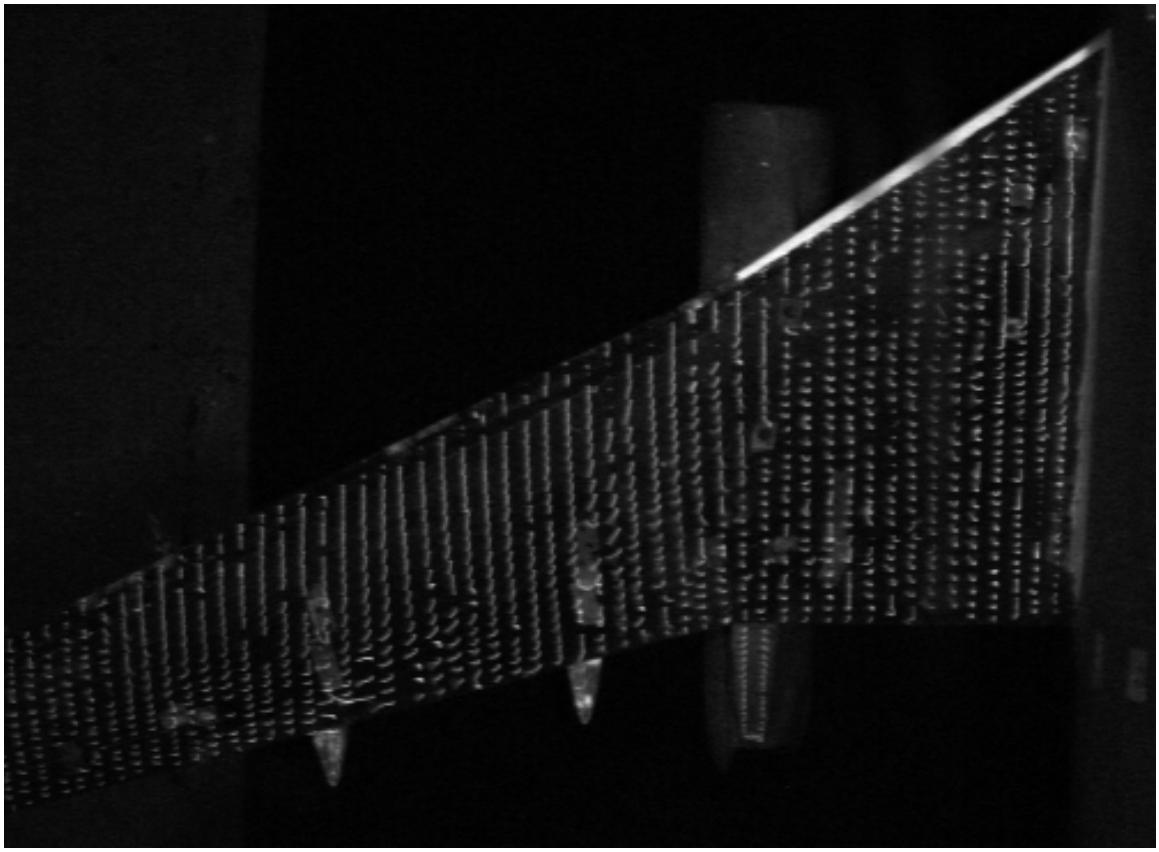

Figure 43.—Wing mini-tuft flow visualization for inboard ice #2, cruise configuration, α =14^{o}, run 516 condition.

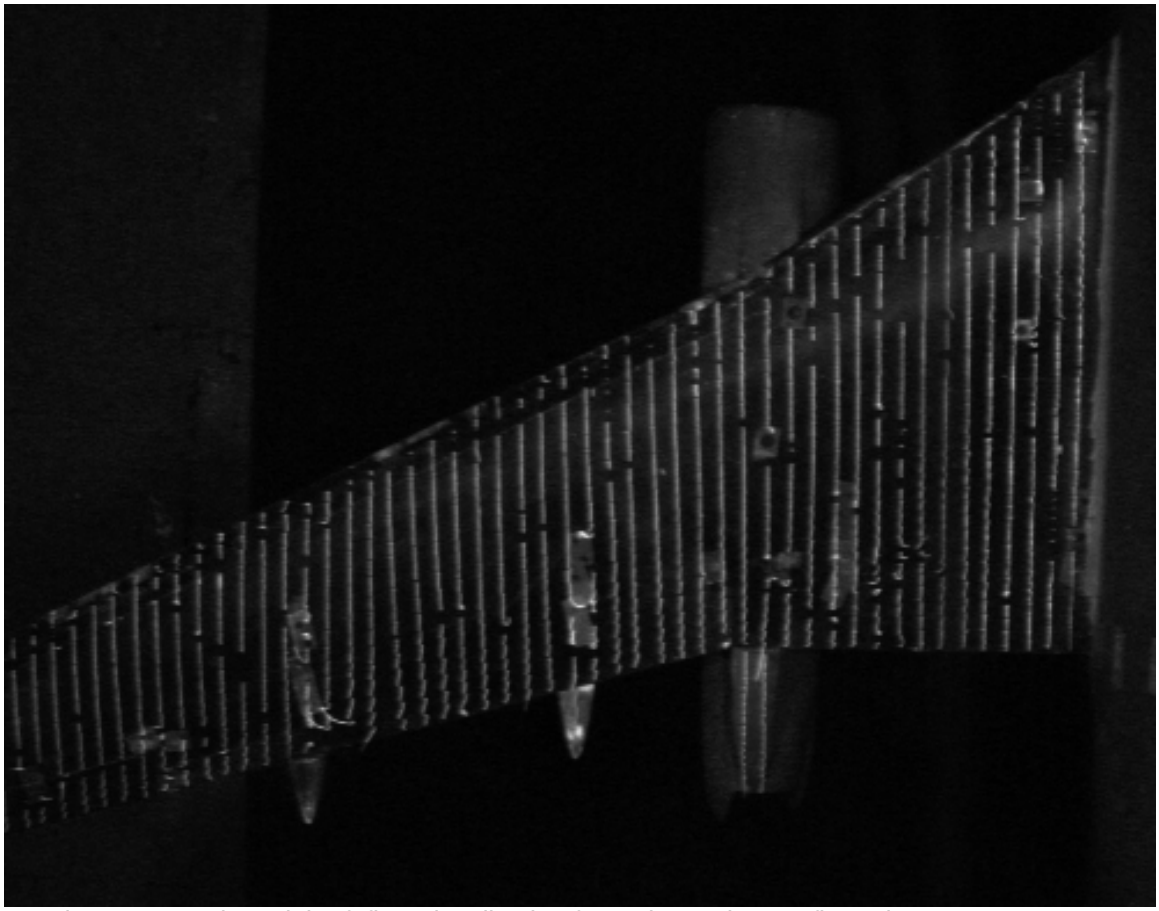

Figure 44.—Wing mini-tuft flow visualization for no ice,cruise configuration, α =4°, run 500 condition.

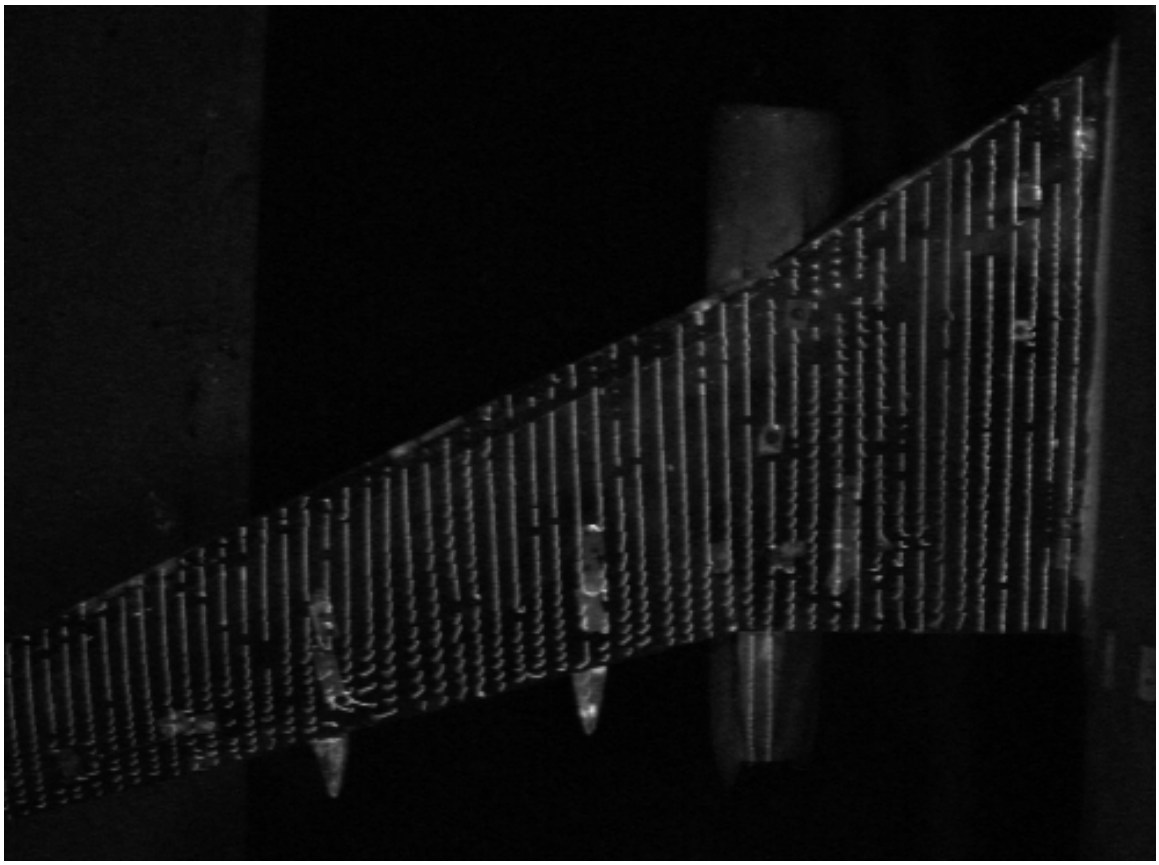

Figure 45.—Wing mini-tuft flow visualization for no ice, cruise configuration, $\alpha = 10^{o}$, run 500 condition.

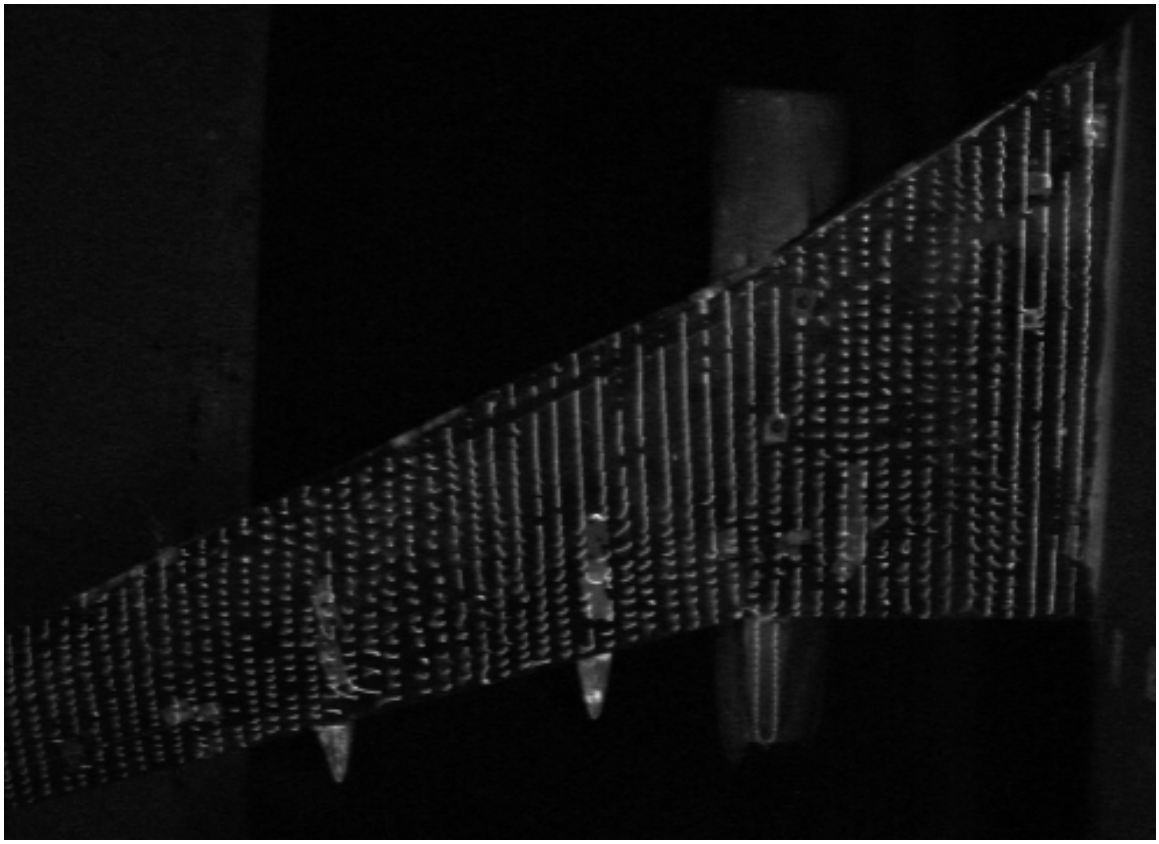

Figure 46.—Wing mini-tuft flow visualization for no ice, cruise configuration, α =14^{o}, run 500 condition.

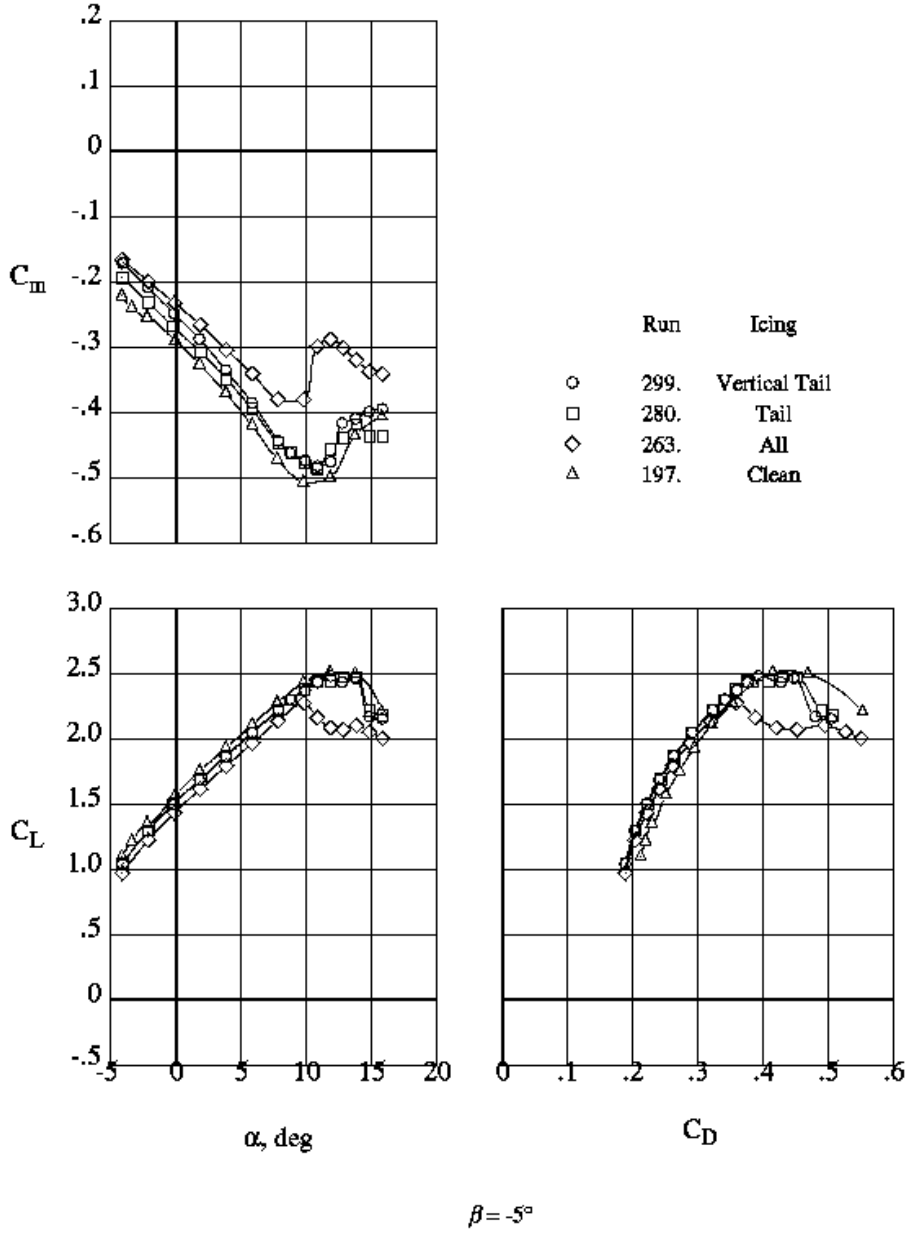

Figure 47.—Effects of Ice #1 on longitudinal aerodynamic characteristics of the model in the δ_f=40° configuration.

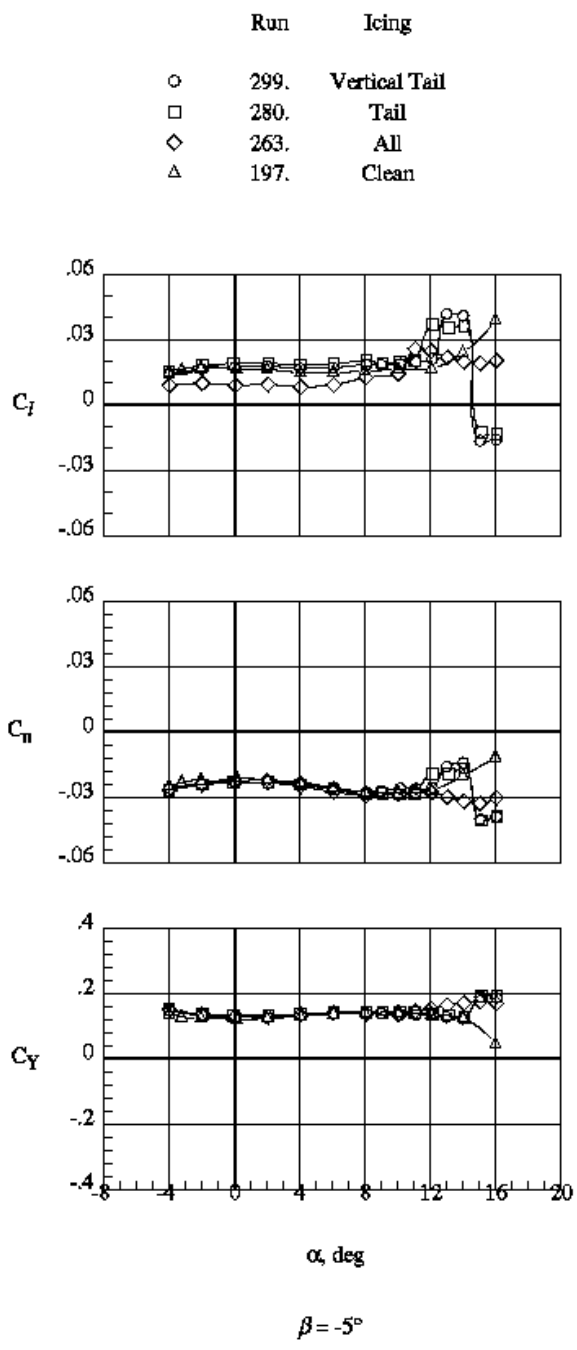

Figure 48.—Effects of Ice #1 and sideslip on the lateral aerodynamic characteristics of the model in the δ_f=40° configuration.

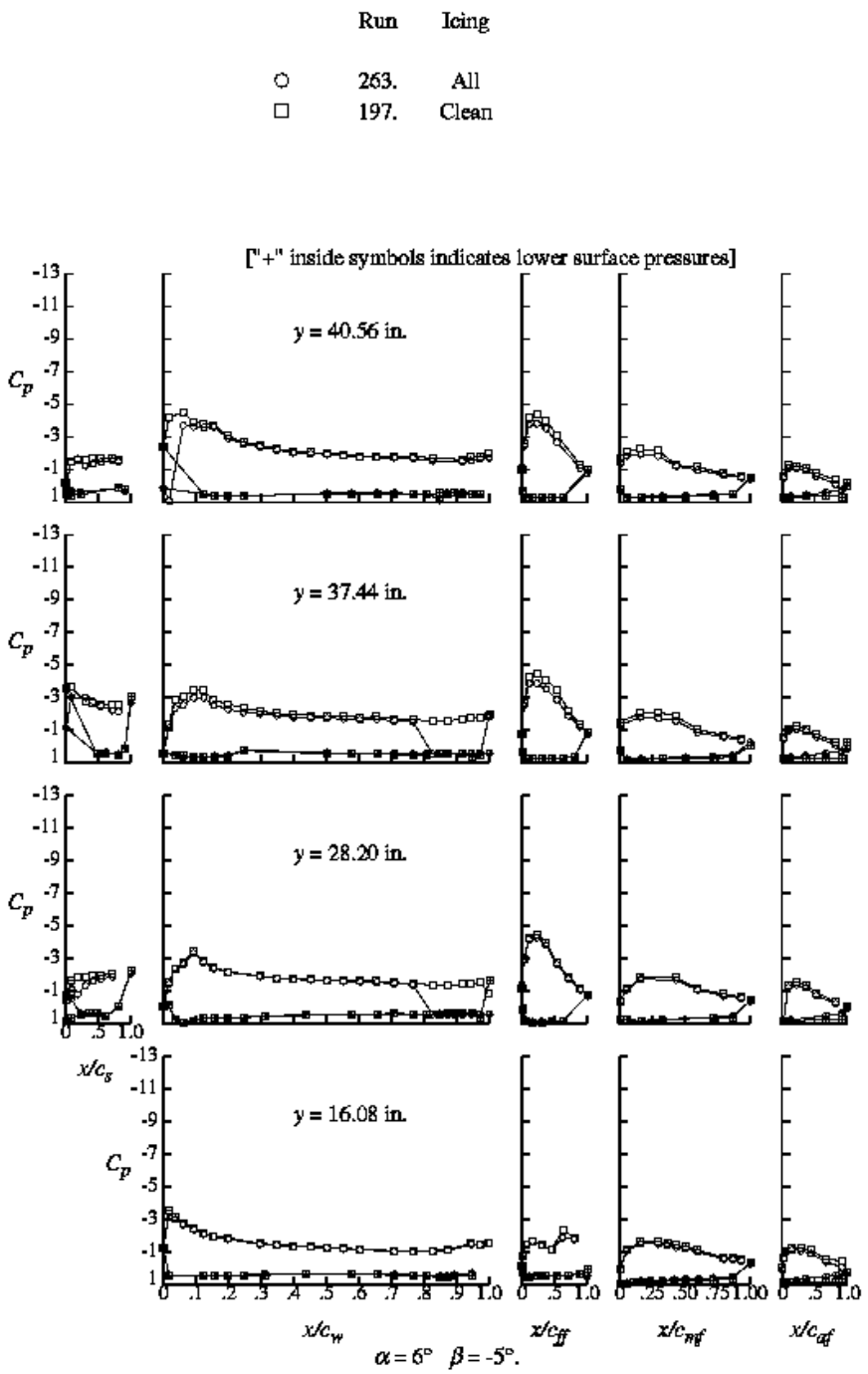

Figure 49.—Effect of Ice #1 on the wing pressure distributions for the model in the δ_f=40° configuration.

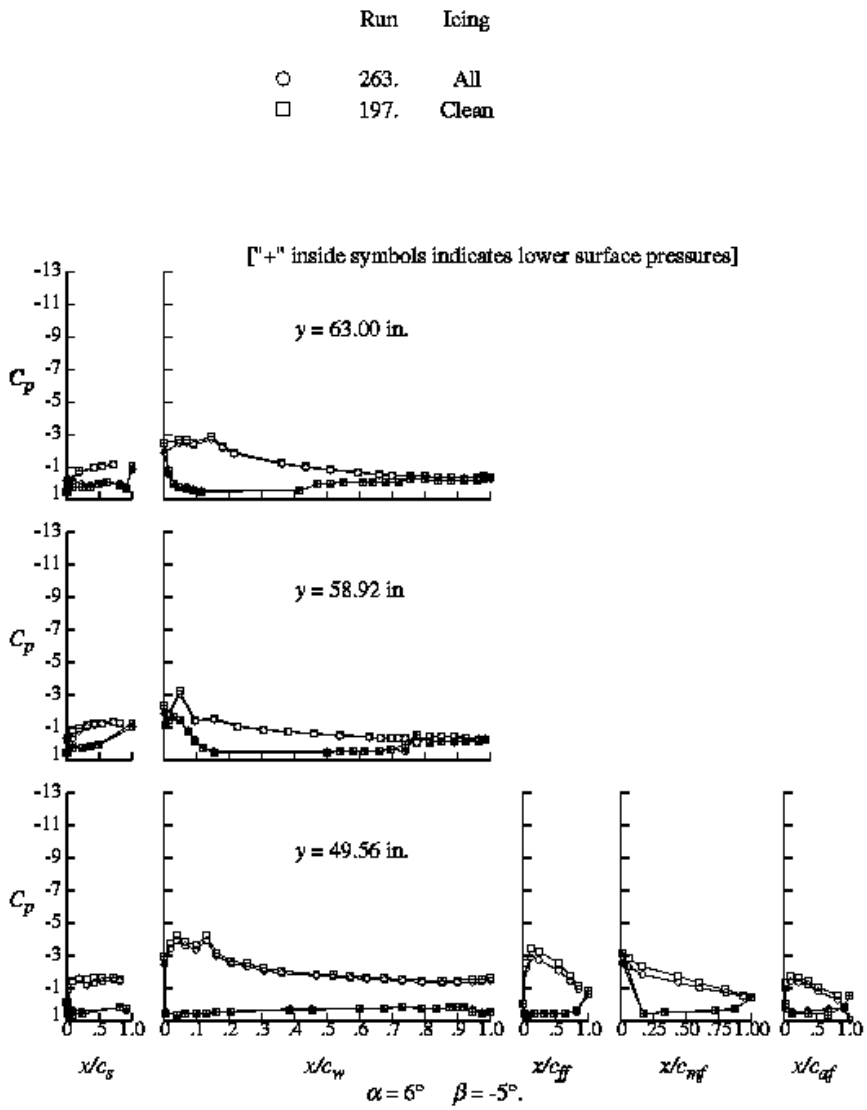

Figure 49 (concluded).—Effect of Ice #1 on the wing pressure distributions for the model in the δ_f=40° configuration.

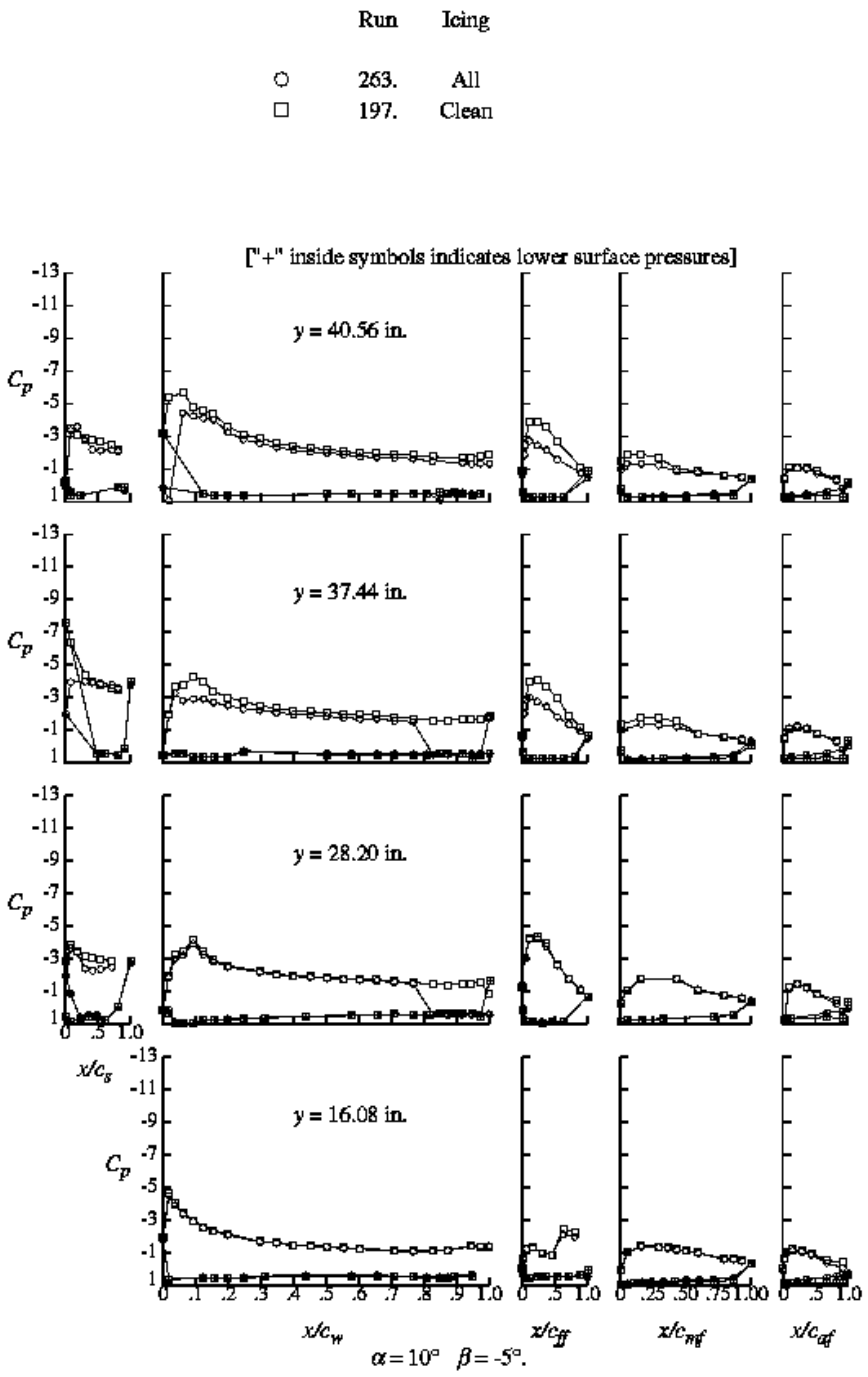

Figure 50.—Effect of Ice #1 on the wing pressure distributions for the model in the δ_f=40° configuration.

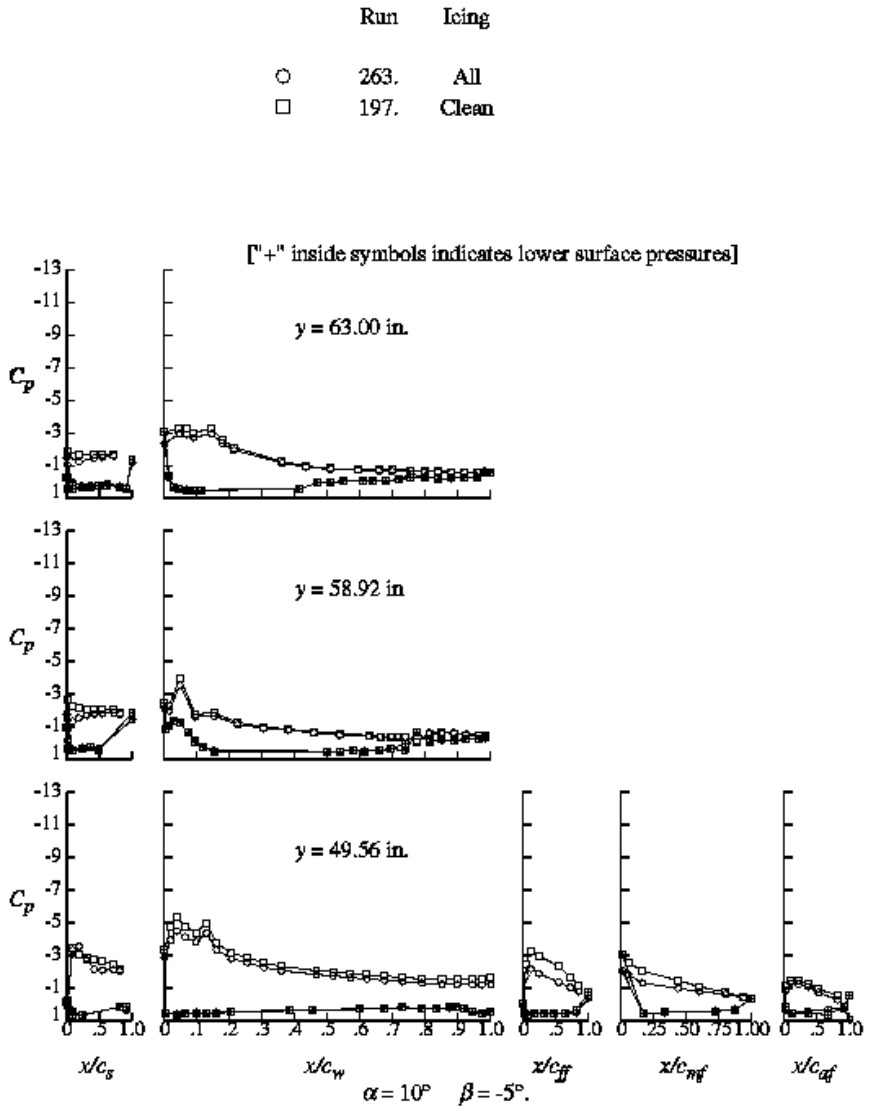

Figure 50 (concluded).—Effect of Ice #1 on the wing pressure distributions for the model in the δ_f=40° configuration.

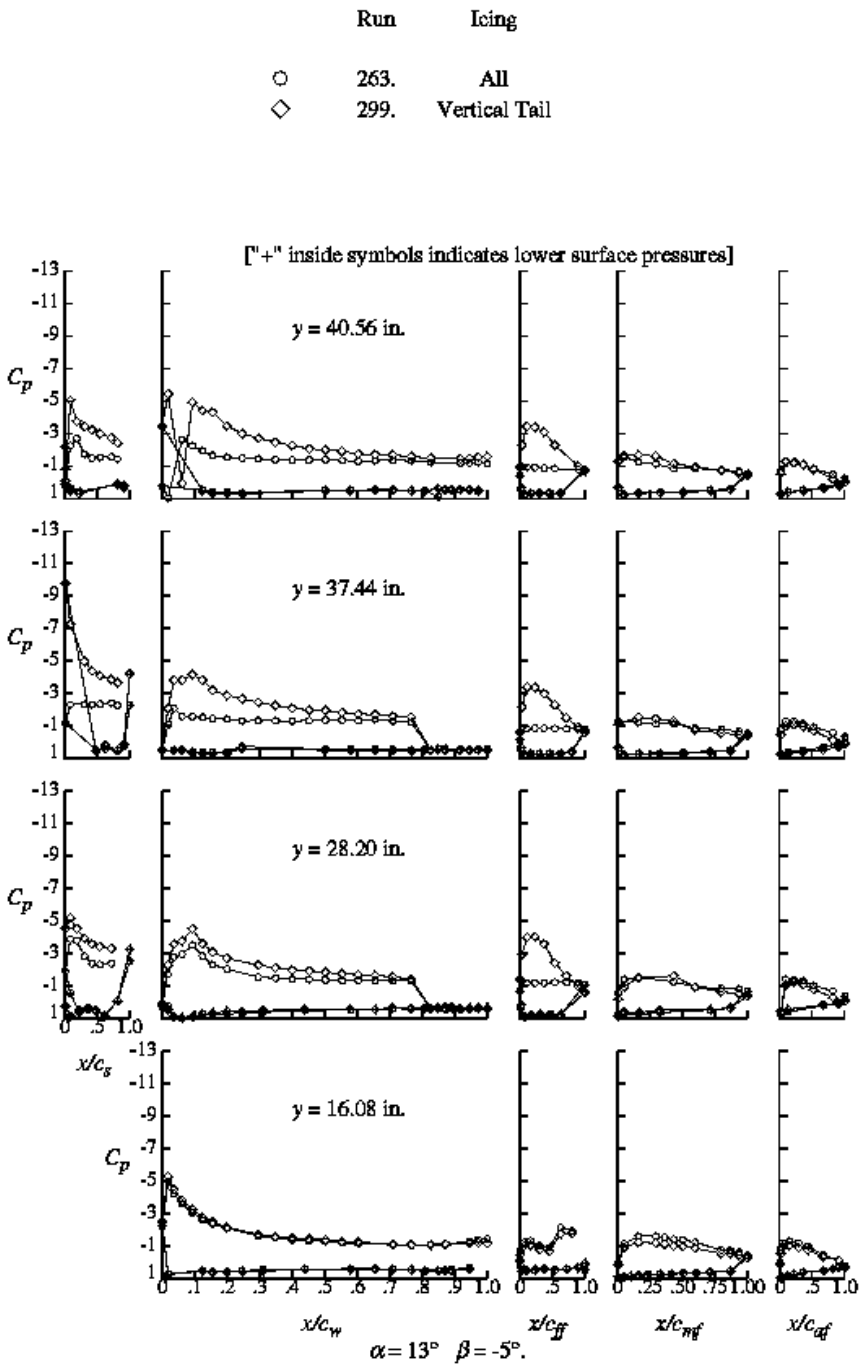

Figure 51.—Effect of Ice #1 on the wing pressure distributions for the model in the δ_f=40° configuration.

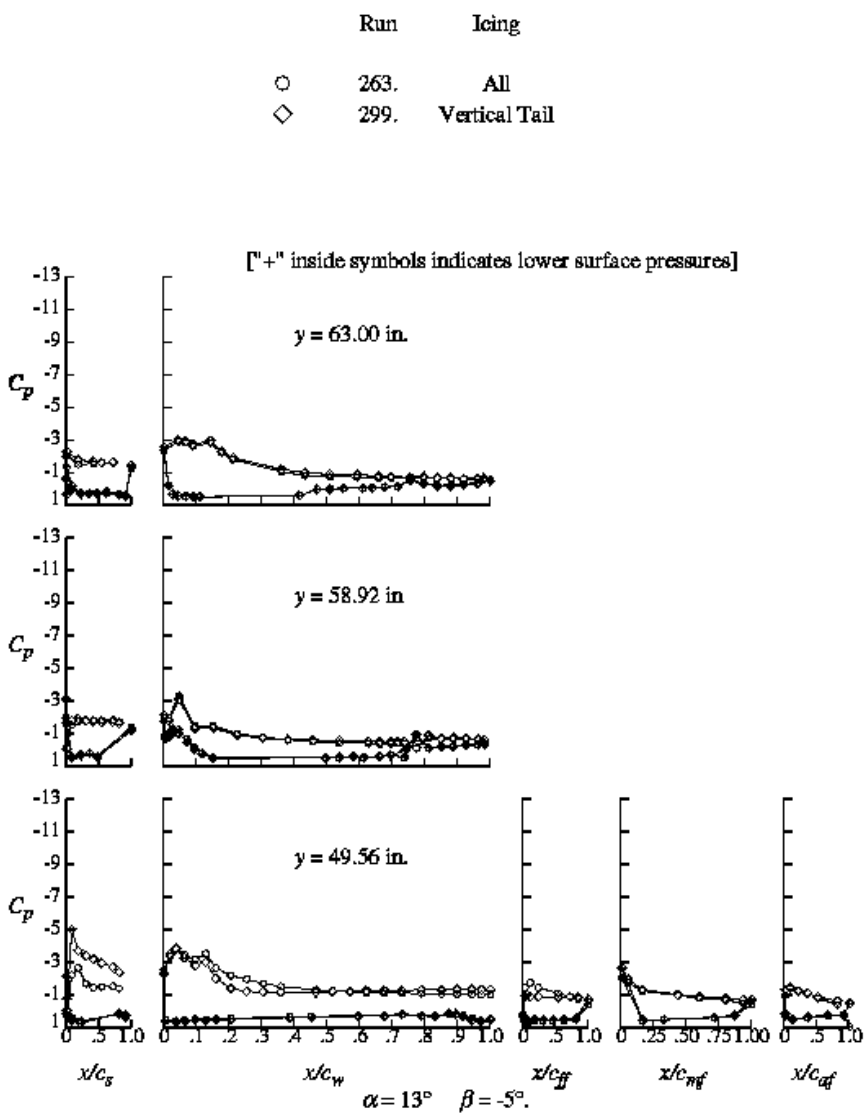

Figure 51 (concluded).—Effect of Ice #1 on the wing pressure distributions for the model in the δ_f=40° configuration.

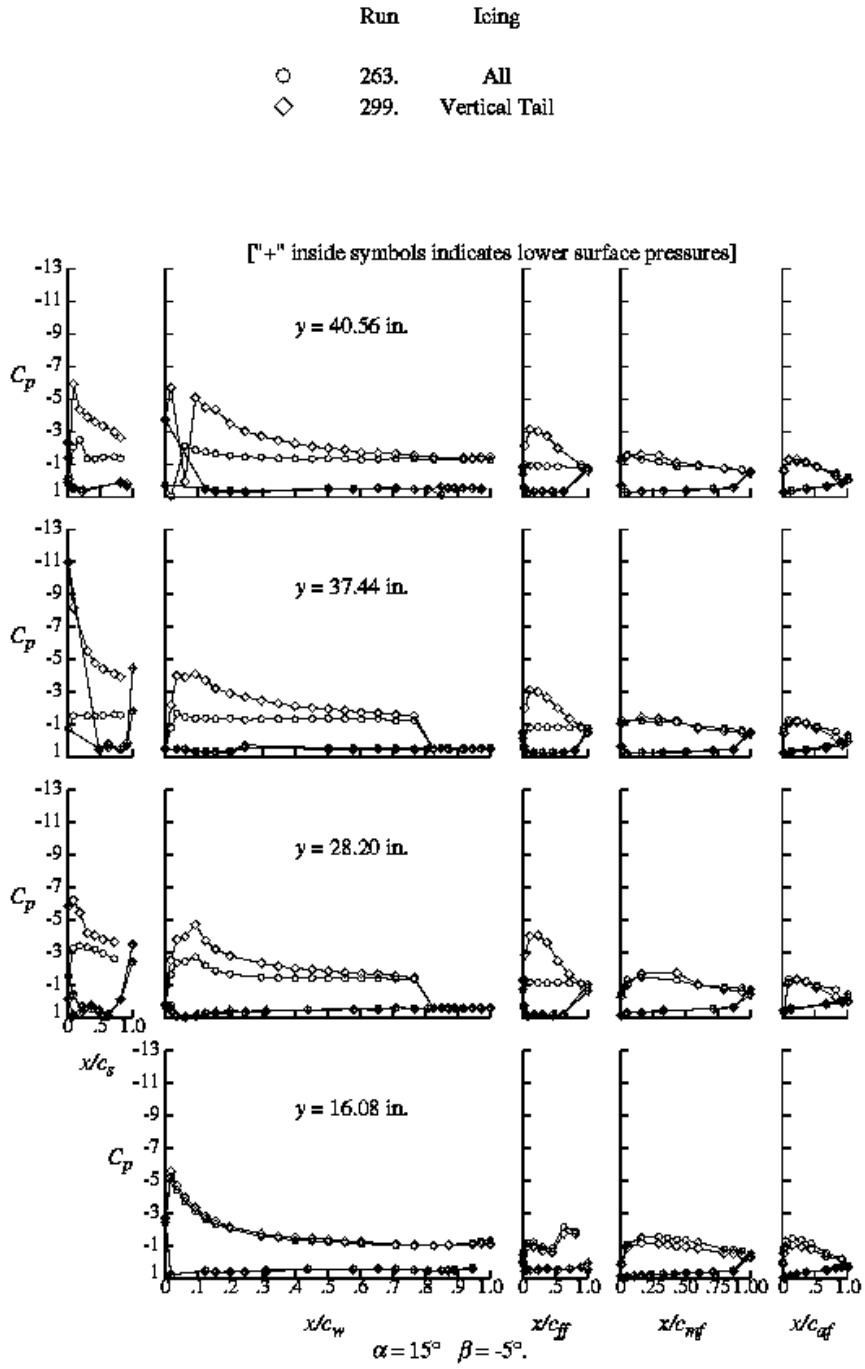

Figure 52.—Effect of Ice #1 on the wing pressure distributions for the model in the δ_i=40° configuration.

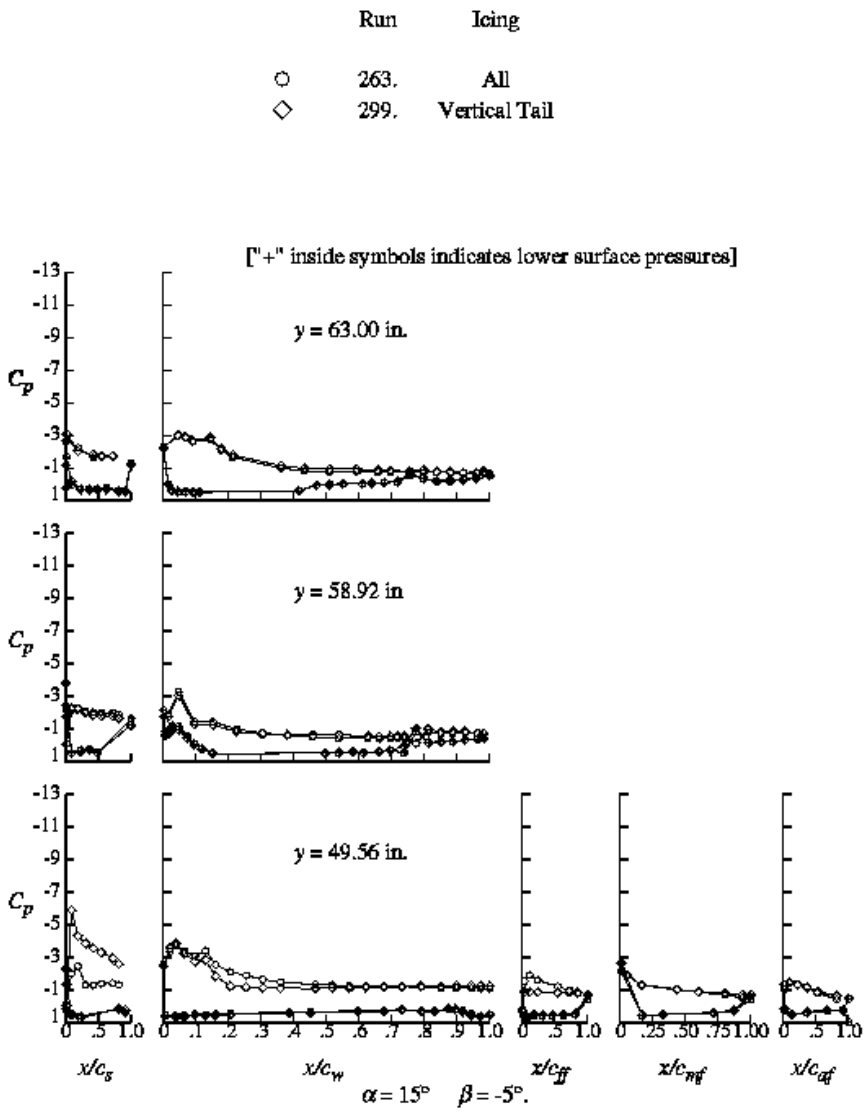

Figure 52 (concluded).—Effect of Ice #1 on the wing pressure distributions for the model in the δ_f=40° configuration.

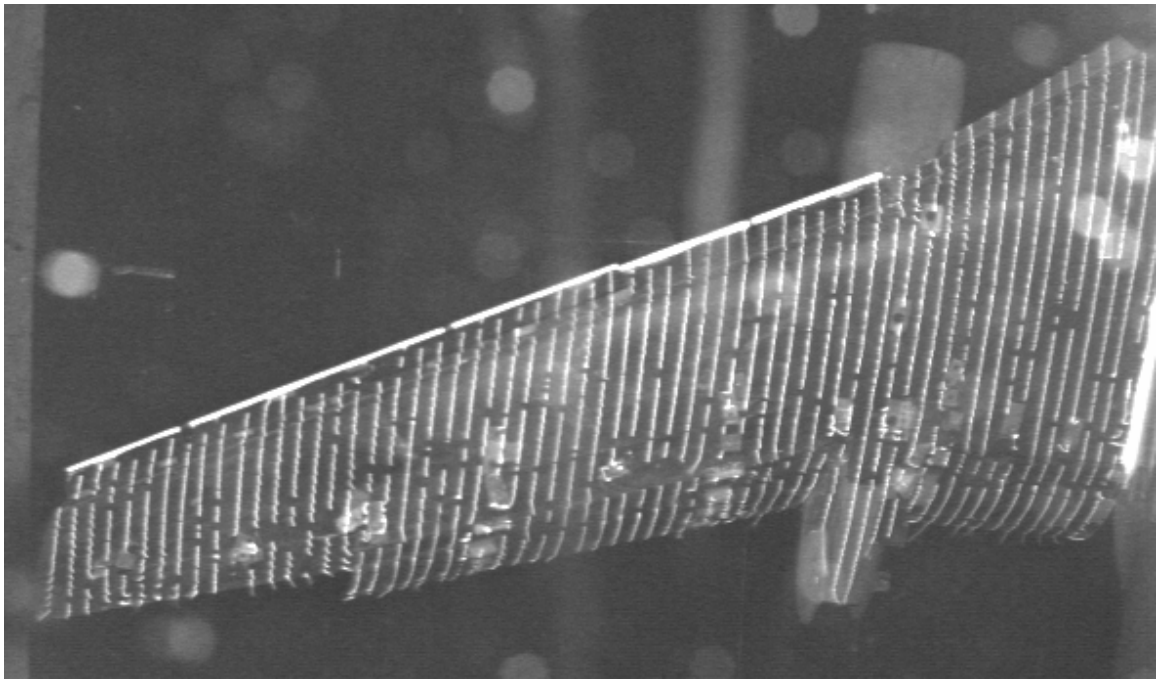

Figure 53.—Wing mini-tuft flow visualization for outboard ice #1, δ_f=40°, α=4°, β=-5°, run 263 condition.

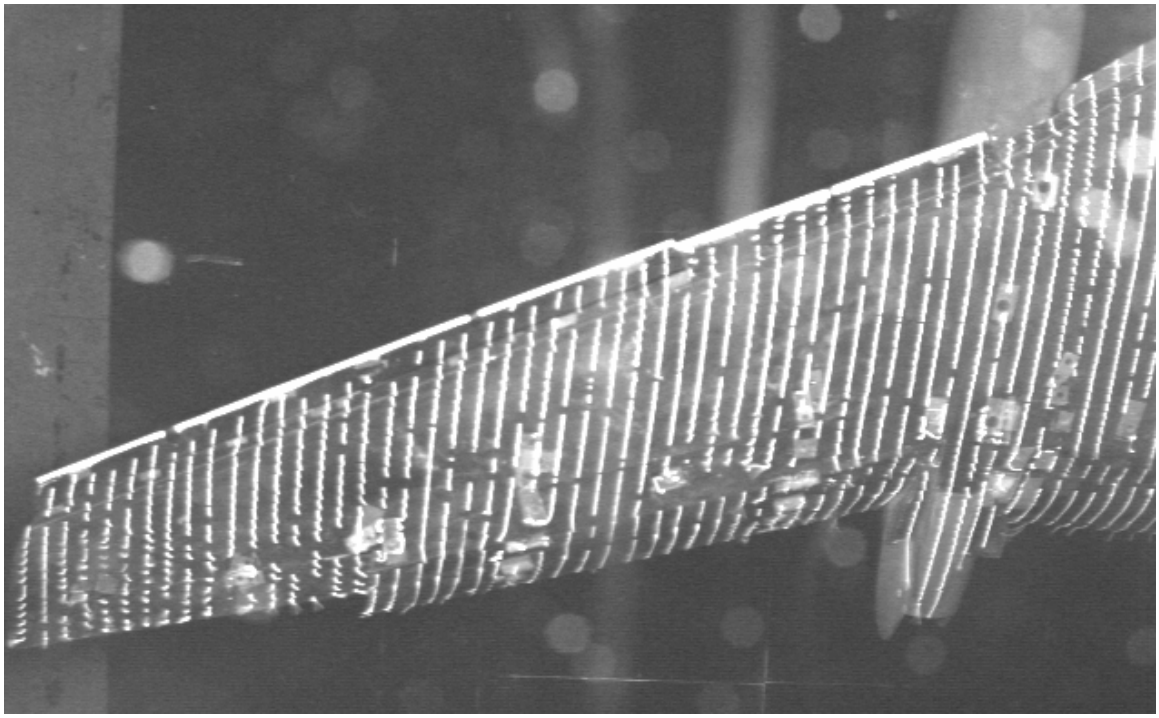

Figure 54.—Wing mini-tuft flow visualization for outboard ice #1, δ_f=40°, α =10°, β =-5°, run 263 condition.

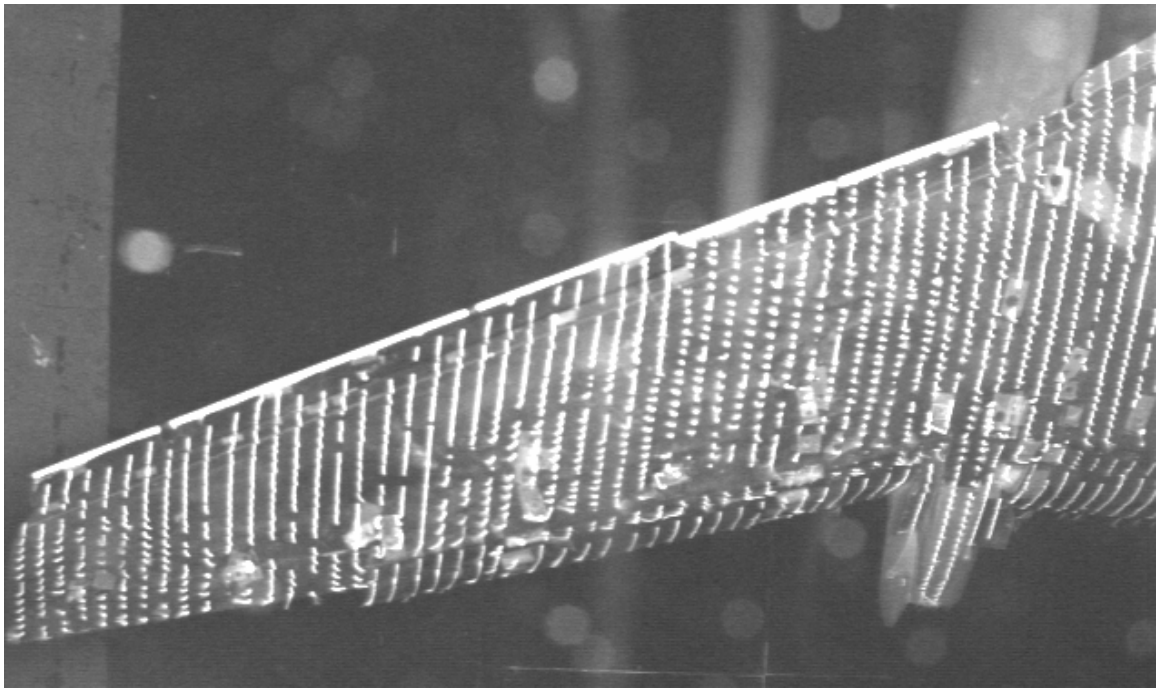

Figure 55.—Wing mini-tuft flow visualization for outboard ice #1, δ_f=40°, α =14°, β =-5°, run 263 condition.

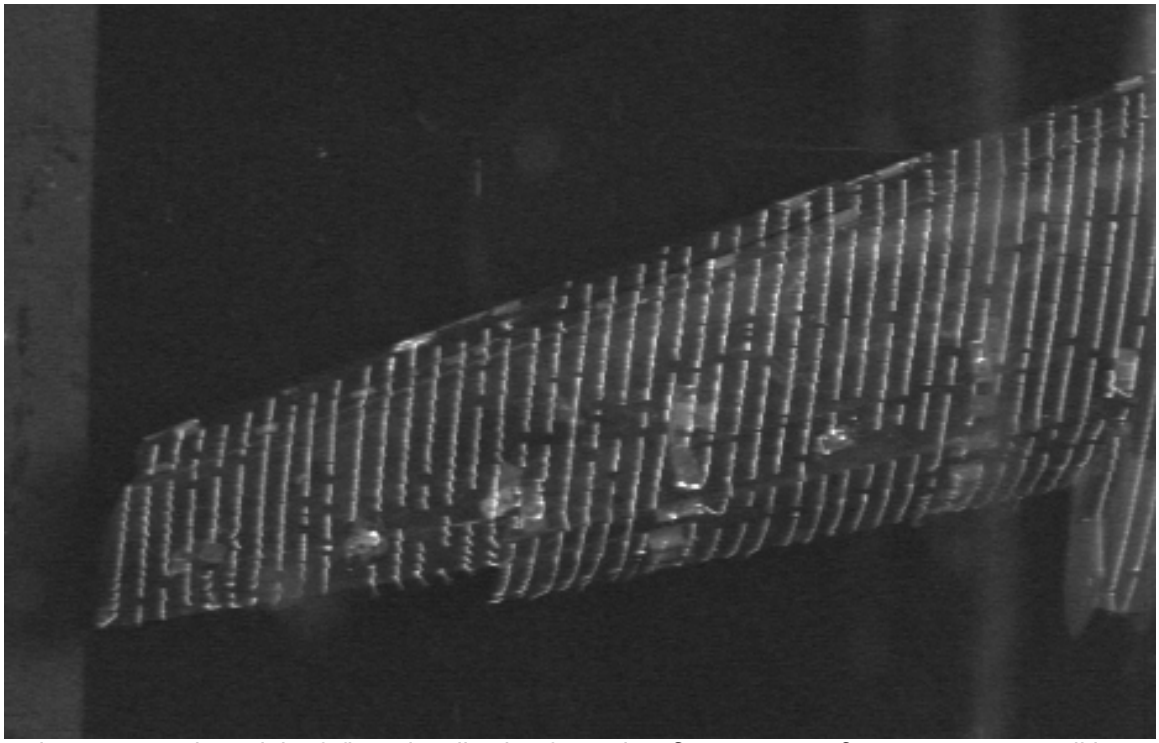

Figure 56.—Wing mini-tuft flow visualization for no ice, δ_f=40°, α =4°, β =-5°, run 280 condition.

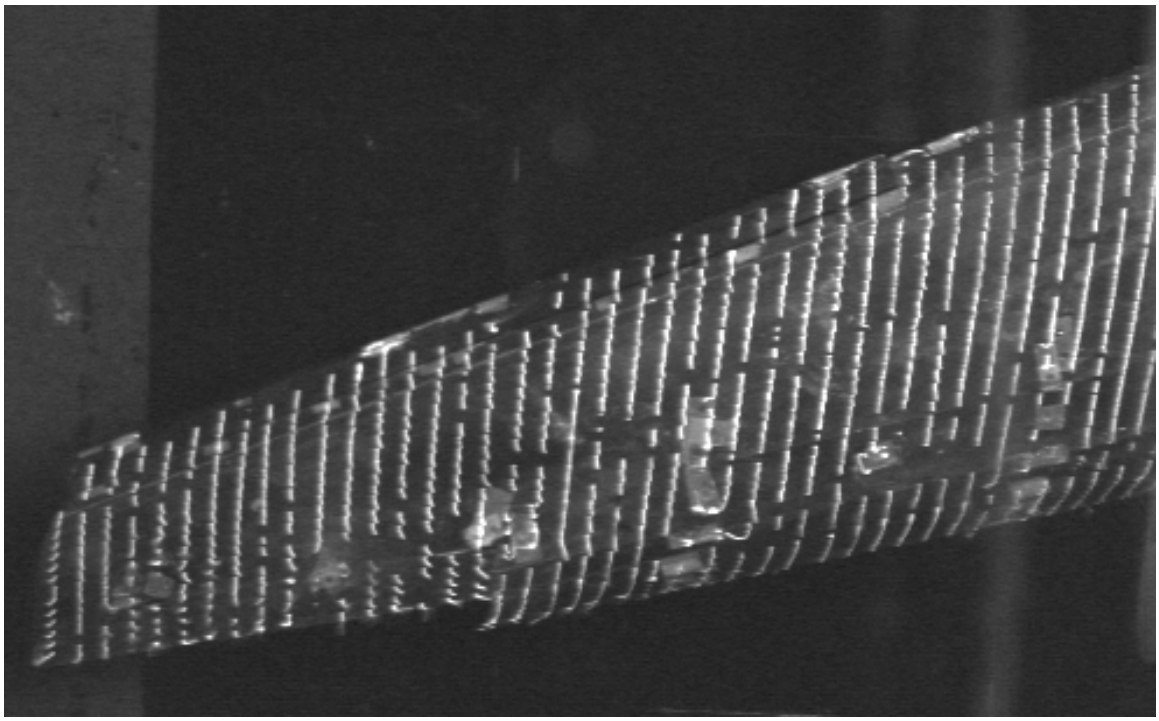

Figure 57.—Wing mini-tuft flow visualization for no ice, δ_f=40°, α =10°, β =-5°, run 280 condition.

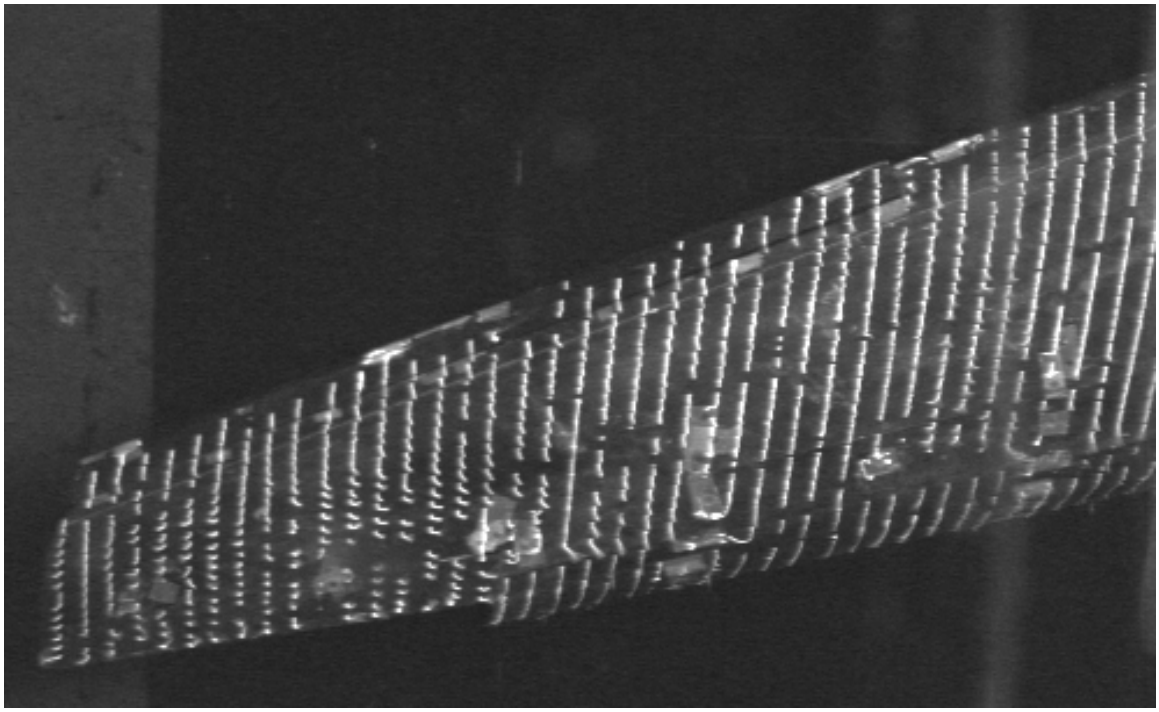

Figure 58.—Wing mini-tuft flow visualization for no ice, δ_f=40°, α =14°, β =-5°, run 280 condition.

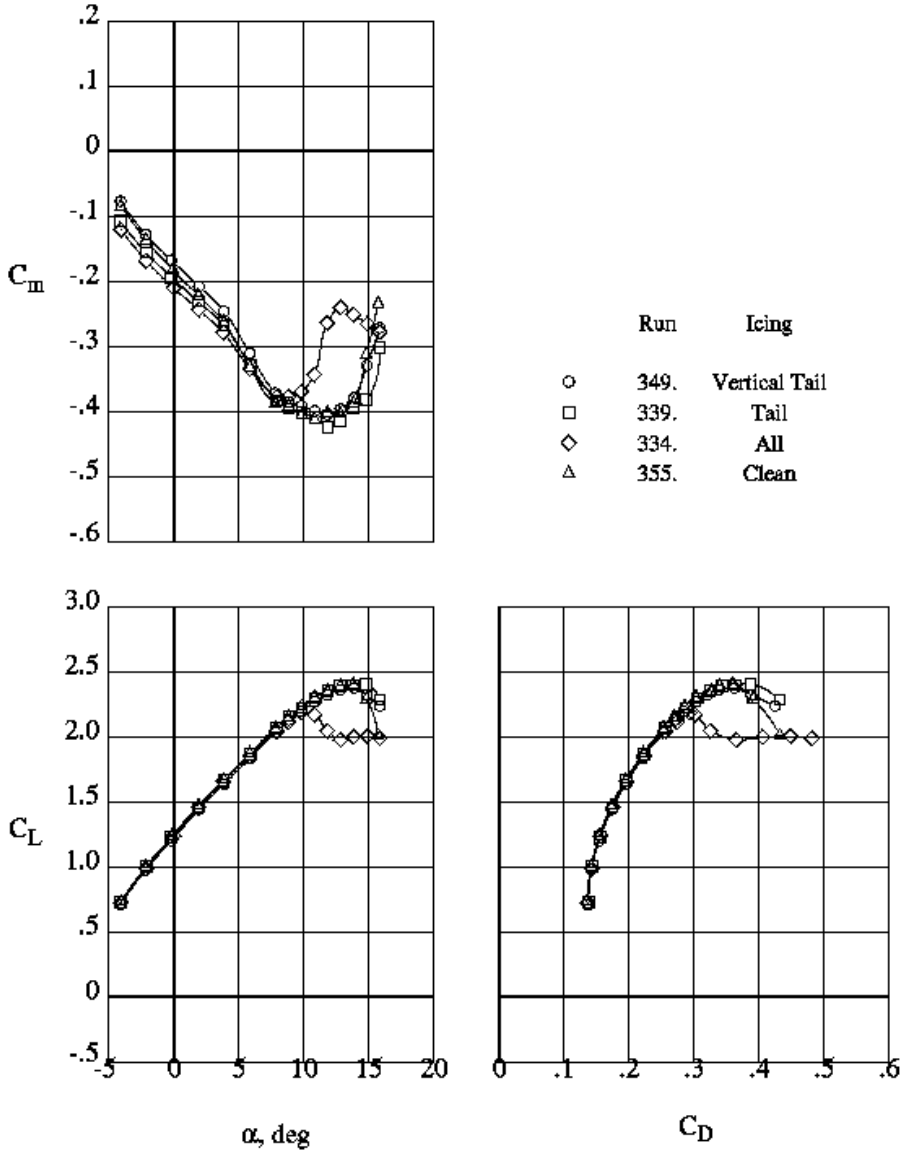

Figure 59.—Effects of Ice #1 on longitudinal aerodynamic characteristics of the model in the δ_f=30° configuration.

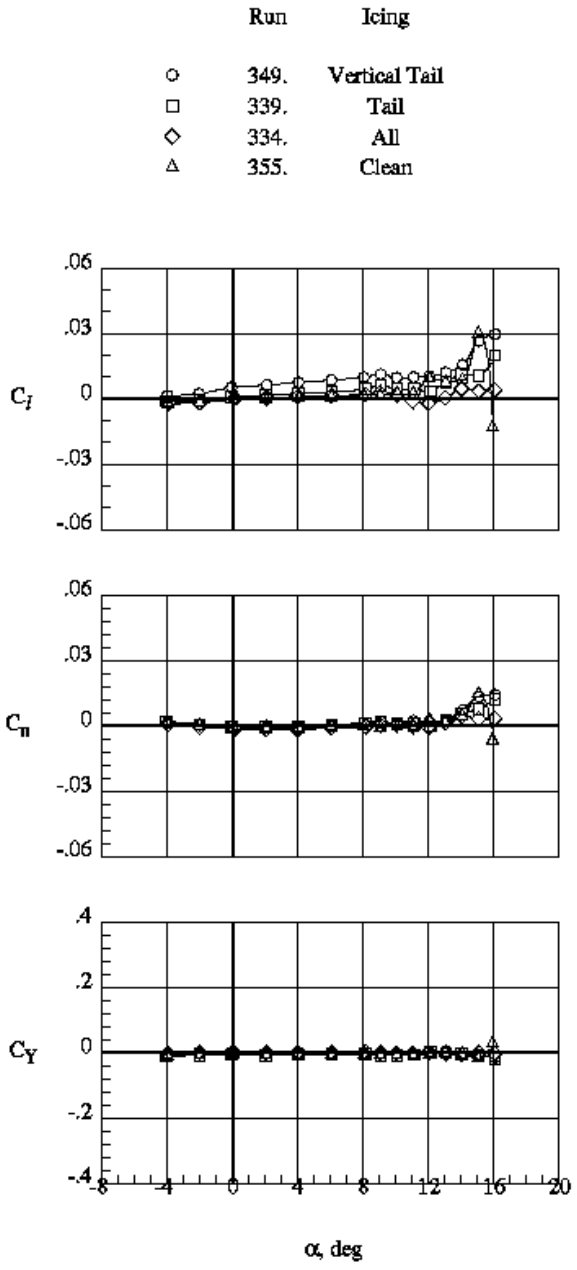

Figure 60.—Effects of Ice #1 and sideslip on the lateral aerodynamic characteristics characteristics of the model in the δ_f=30^o configuration.

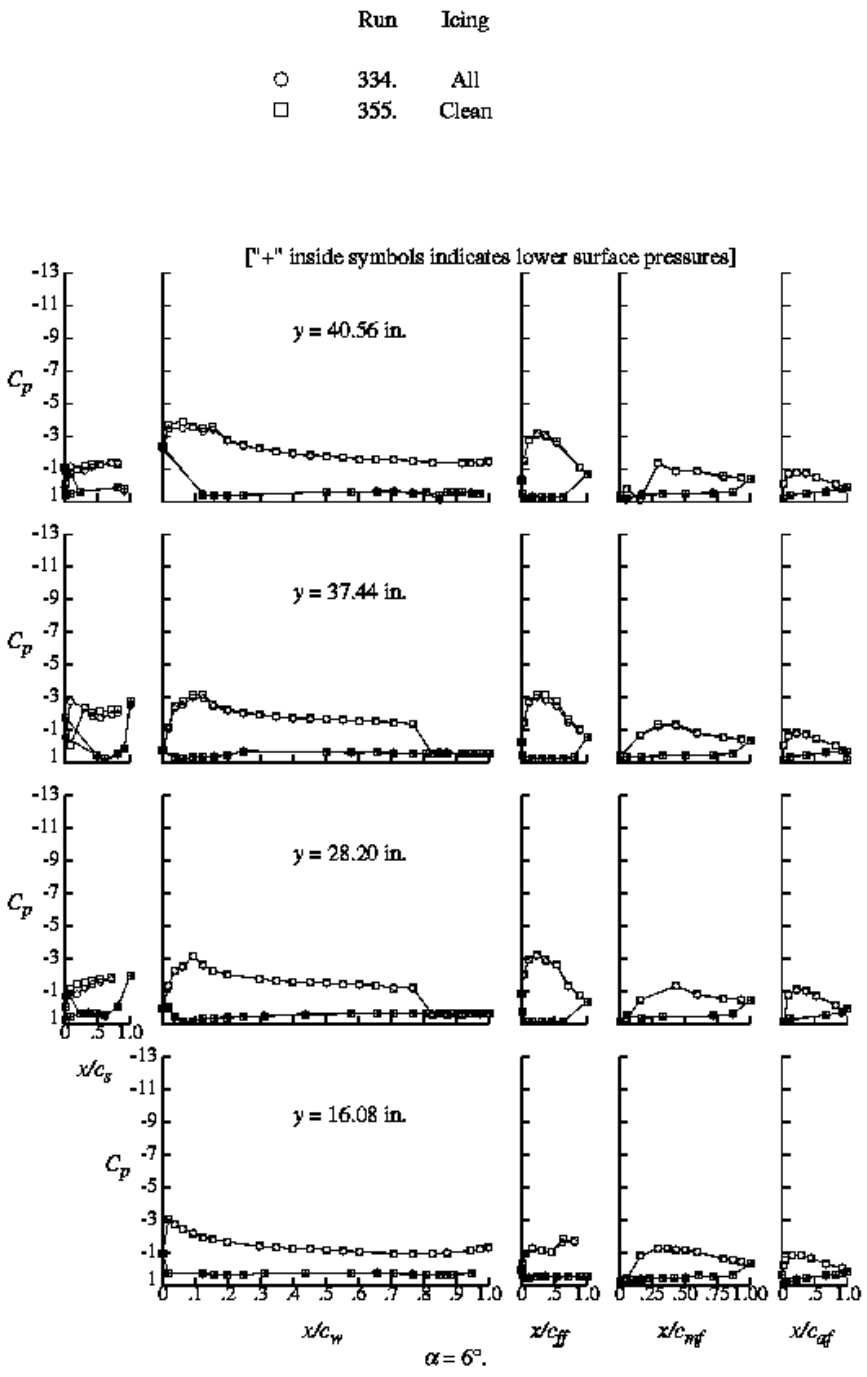

Figure 61.—Effect of Ice #1 on the wing pressure distributions for the model in the δ_f=30° configuration.

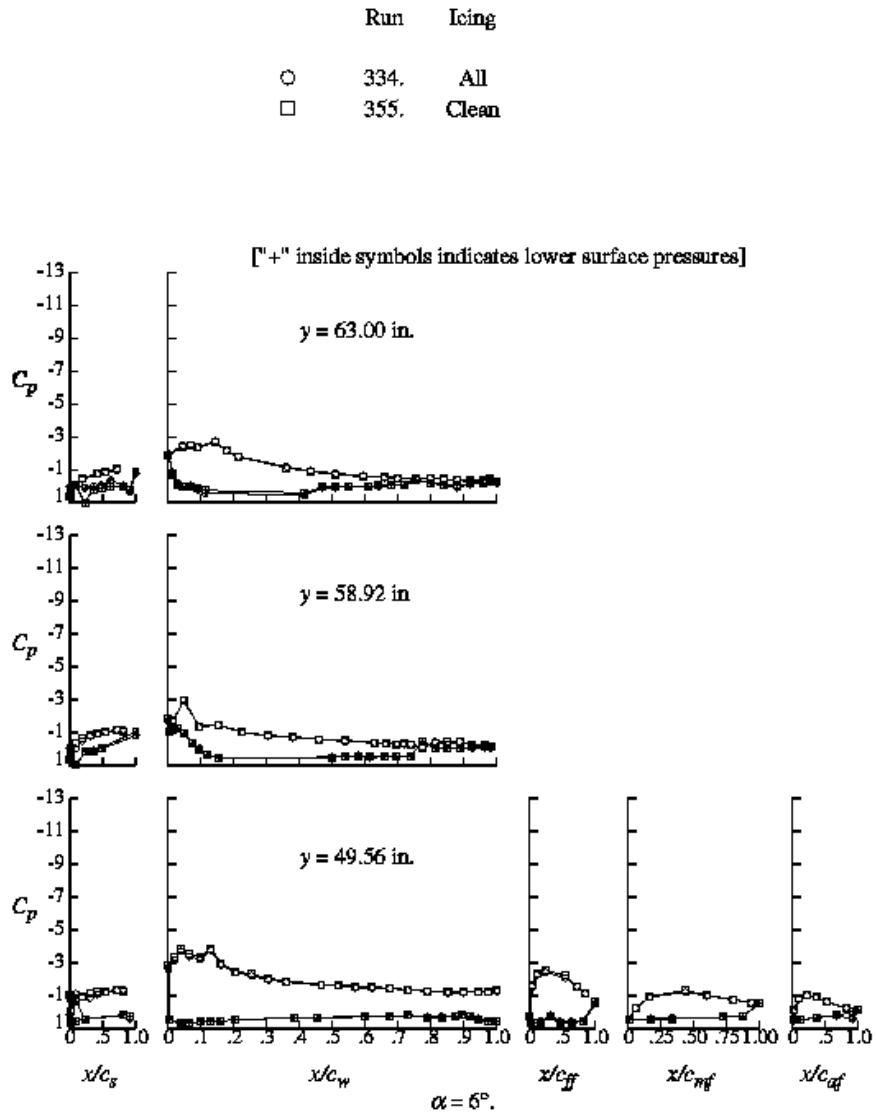

Figure 61 (concluded).—Effect of Ice #1 on the wing pressure distribution for the model in the δ_f=30° configuration.

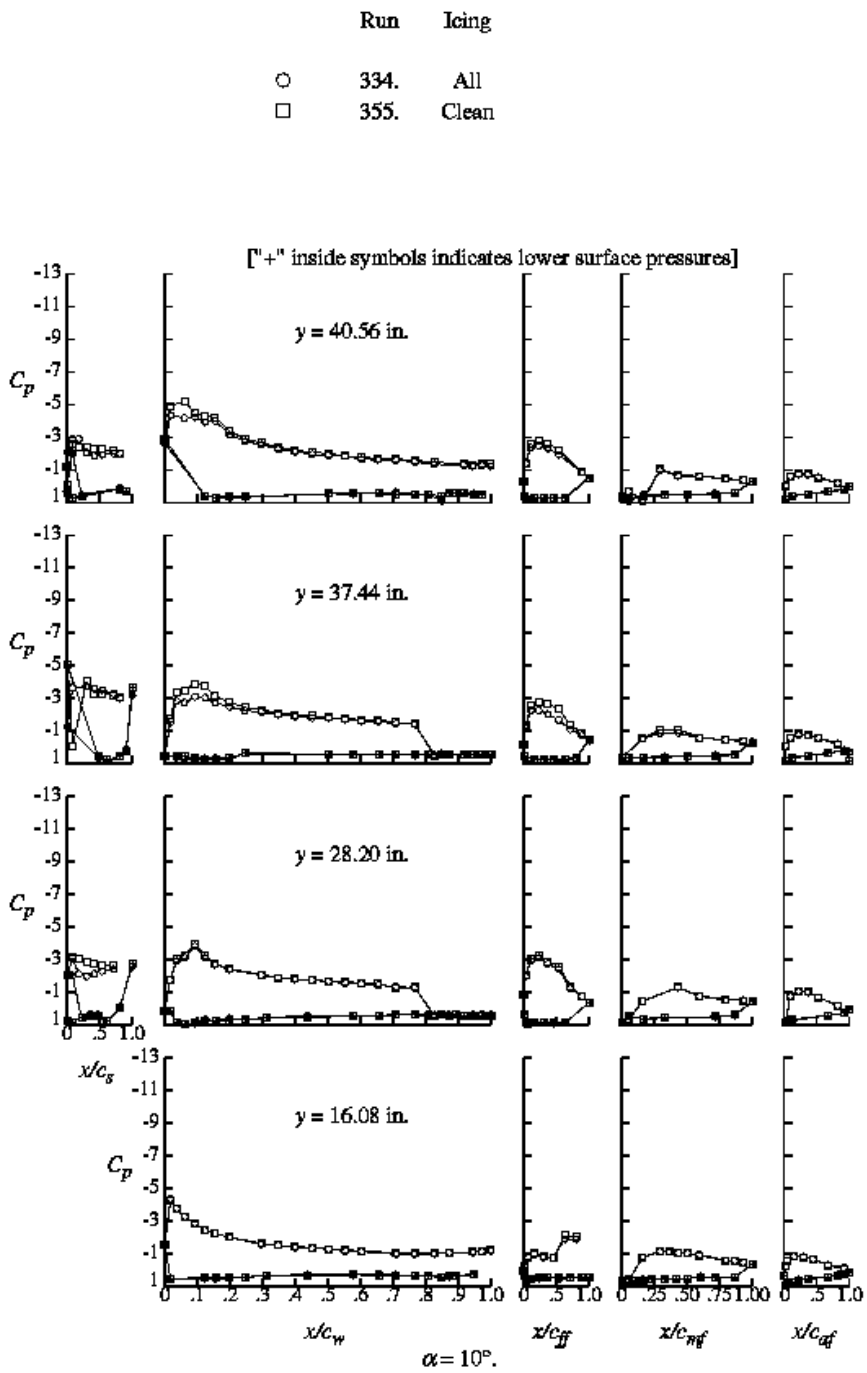

Figure 62.—Effect of Ice #1 on the wing pressure distribution for the model in the δ_f=30° configuration.

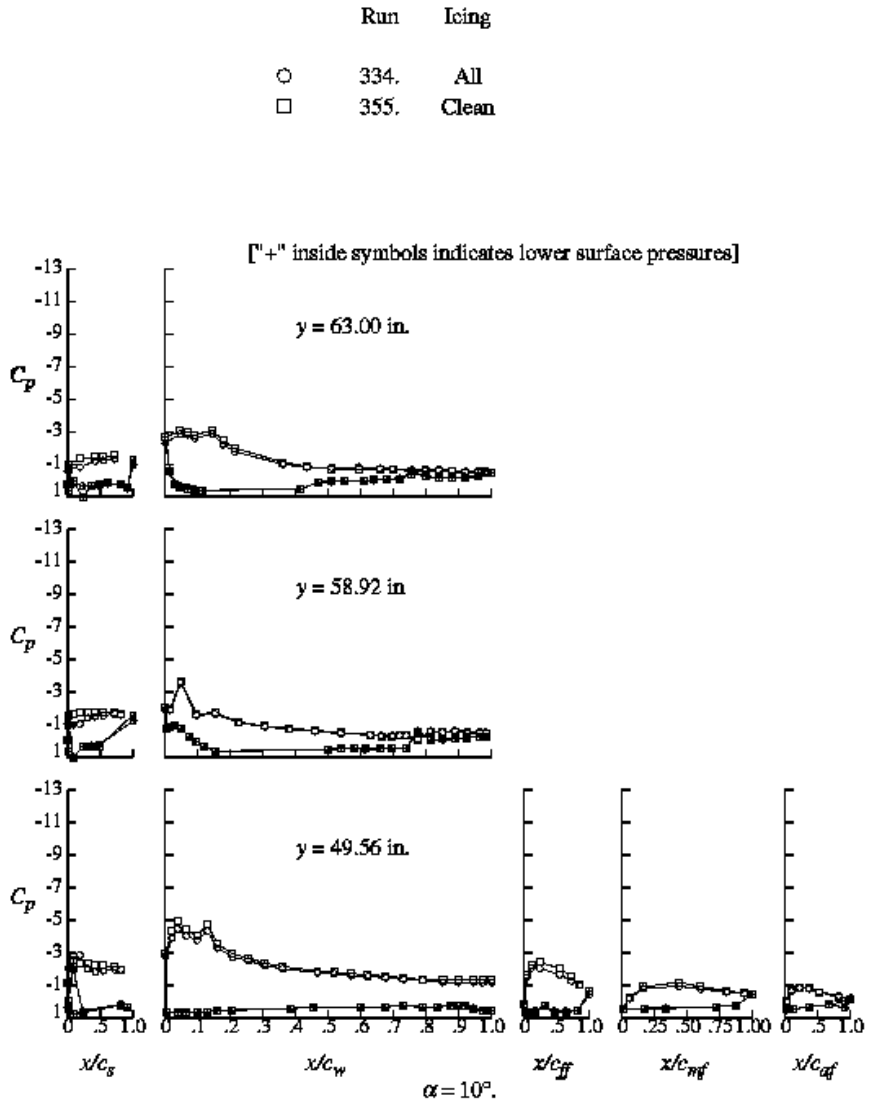

Figure 62 (concluded).—Effect of Ice #1 on the wing pressure distribution for the model in the δ_f=30° configuration.

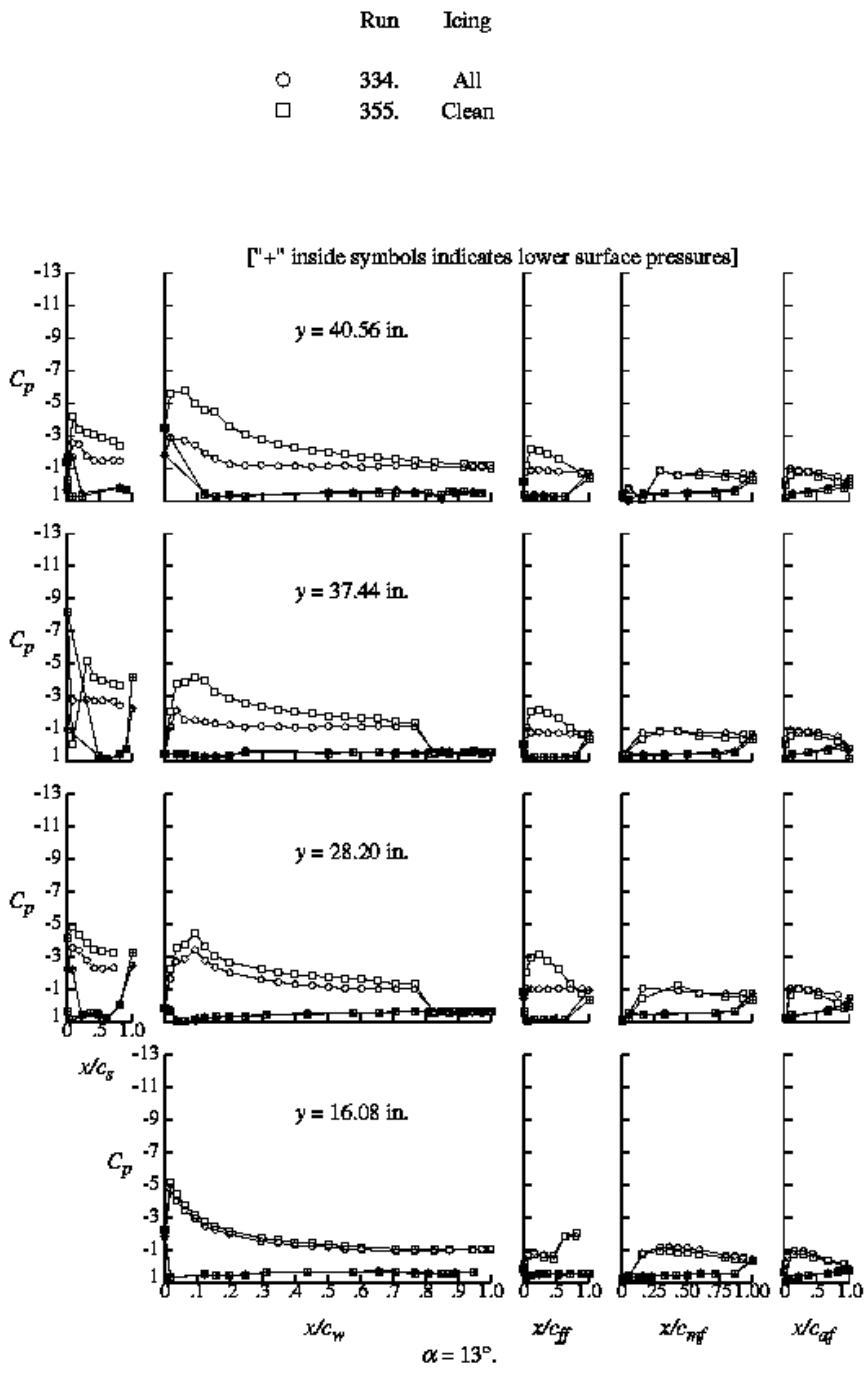

Figure 63.—Effect of Ice #1 on the wing pressure distribution for the model in the δ_f=30° configuration.

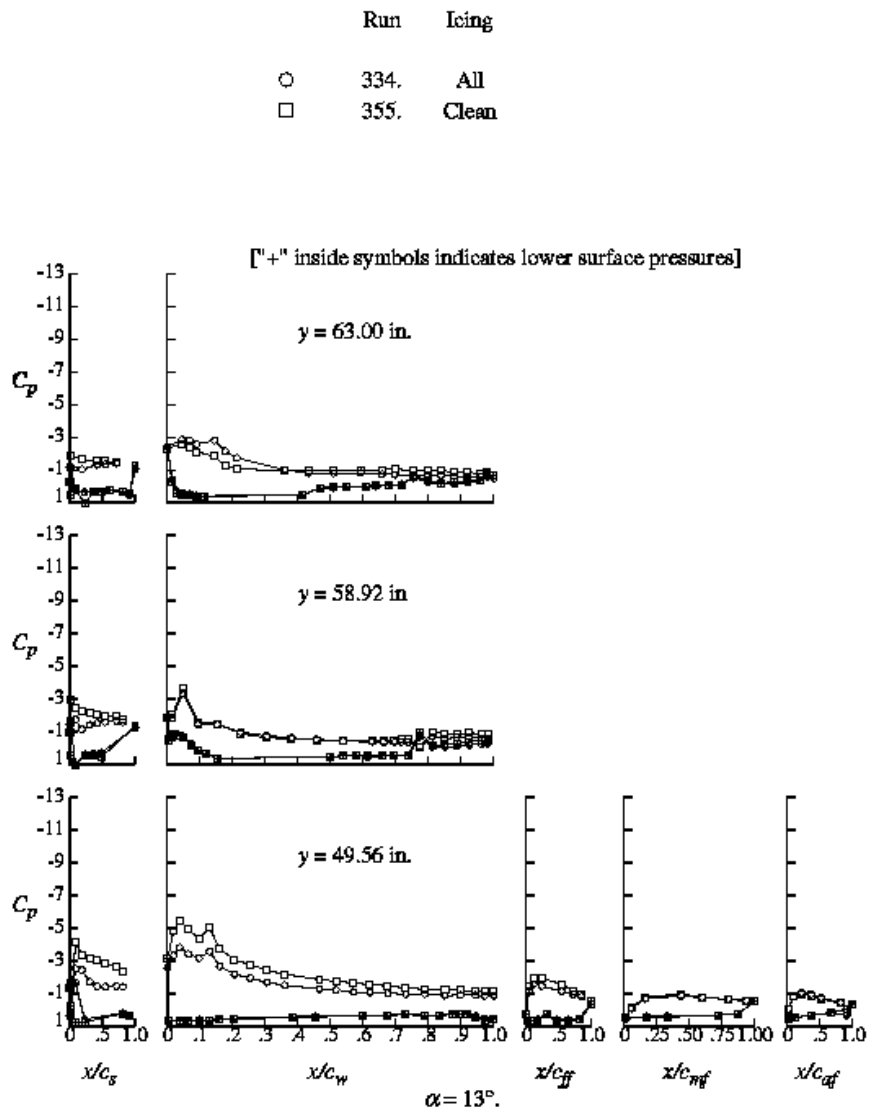

Figure 63 (concluded).—Effect of Ice #1 on the wing pressure distribution for the model in the δ_f=30° configuration.

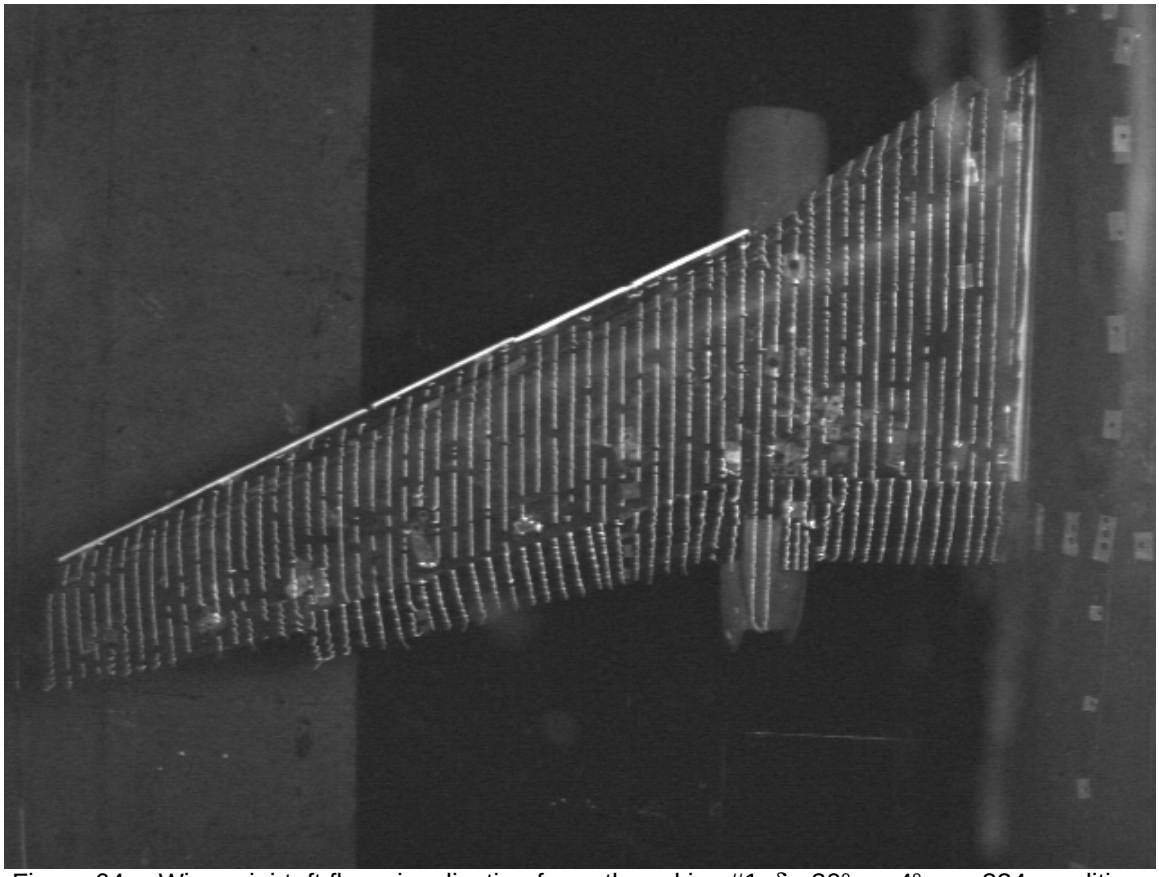

Figure 64.—Wing mini-tuft flow visualization for outboard ice #1, δ_f=30º, α=4º, run 334 condition.

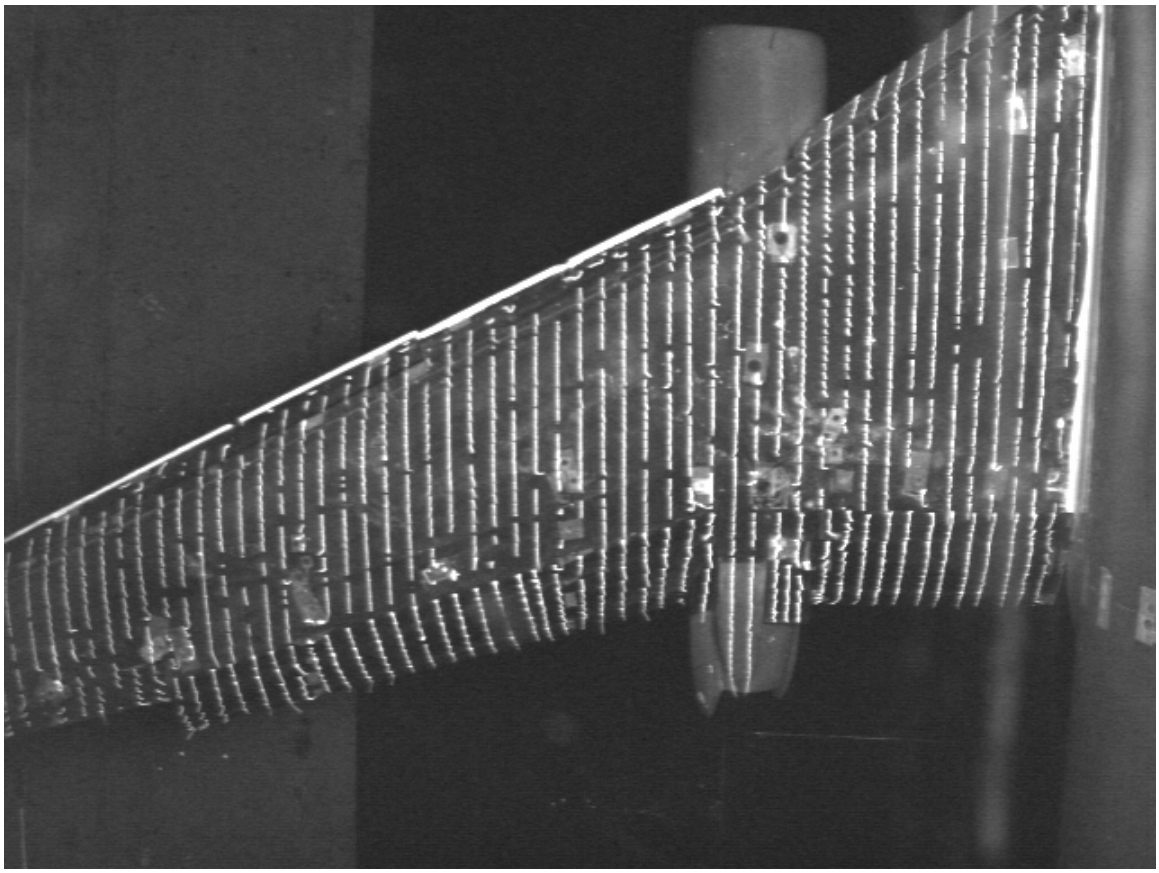

Figure 65.—Wing mini-tuft flow visualization for outboard ice #1, δ_f=30°, α =10°, run 334 condition.

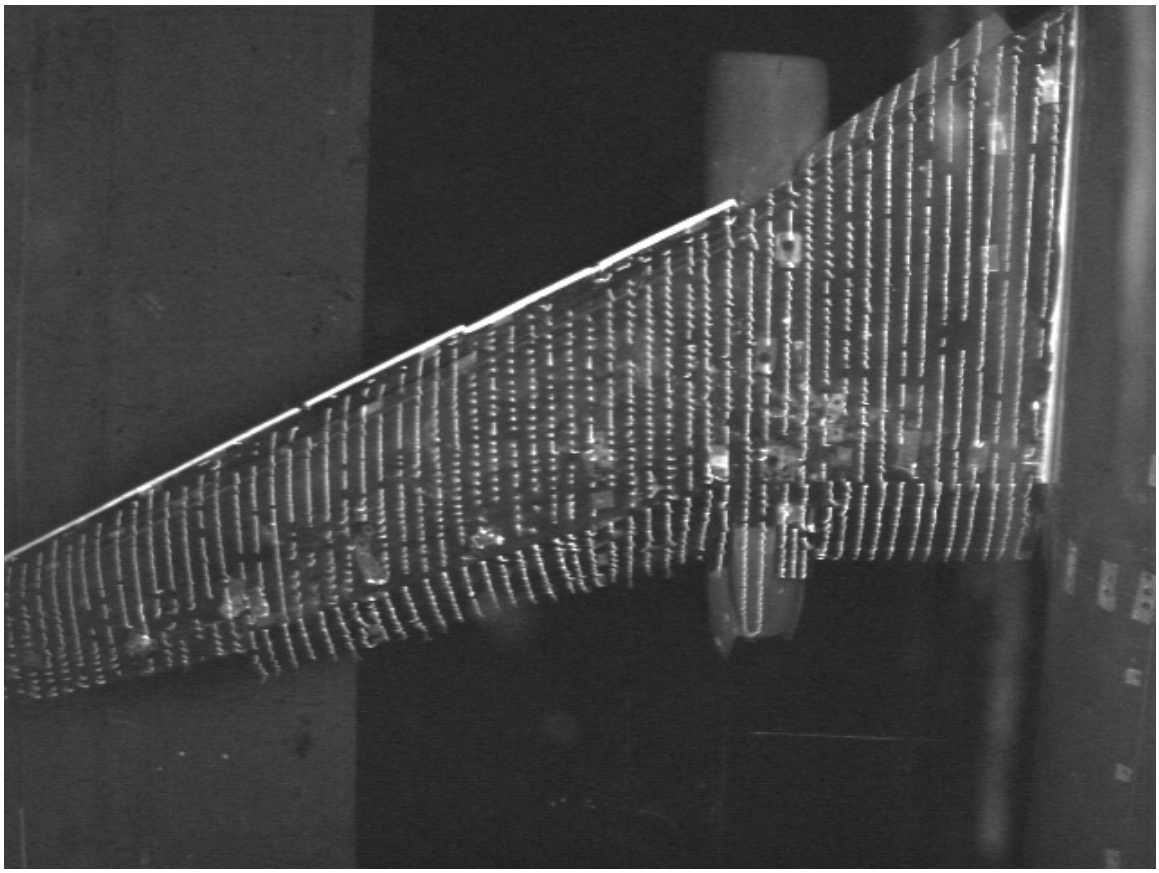

Figure 66.—Wing mini-tuft flow visualization for outboard ice #1, $\delta_f=30^o$, $\alpha=14^o$, run 334 condition.

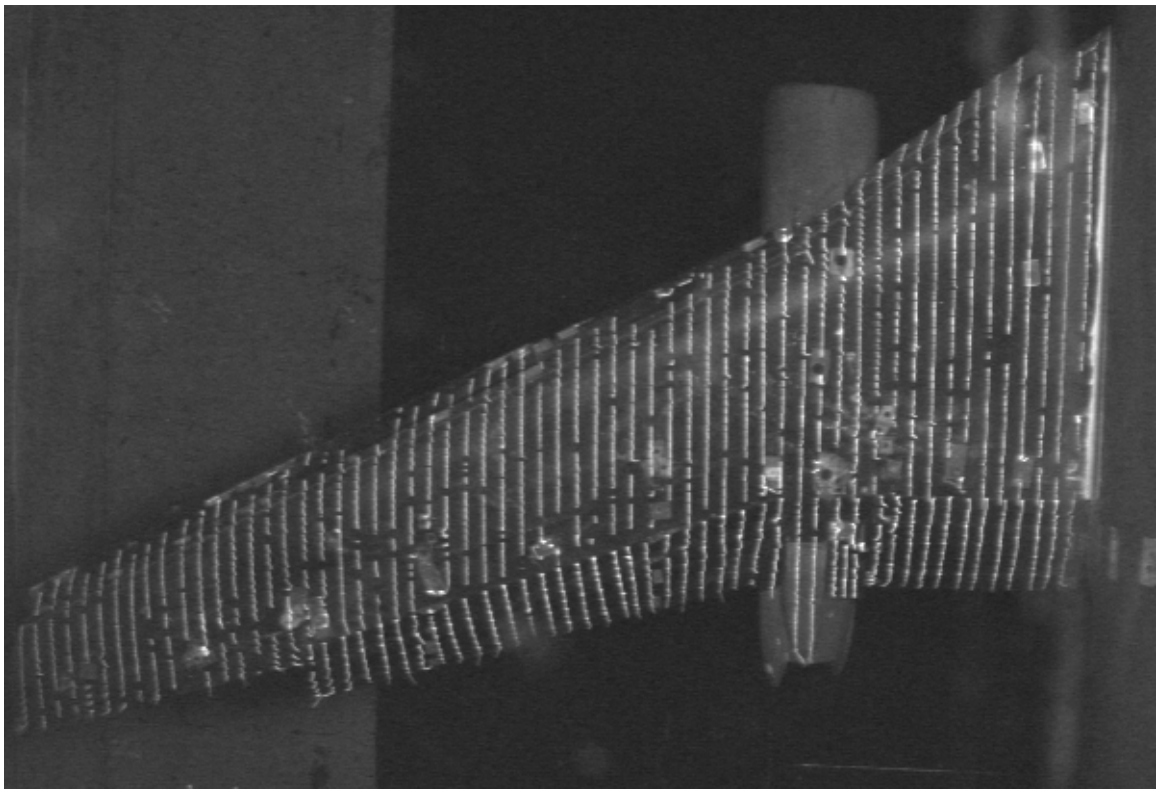

Figure 67.—Wing mini-tuft flow visualization for no ice, δ_f=30°, α =4°, run 349 condition.

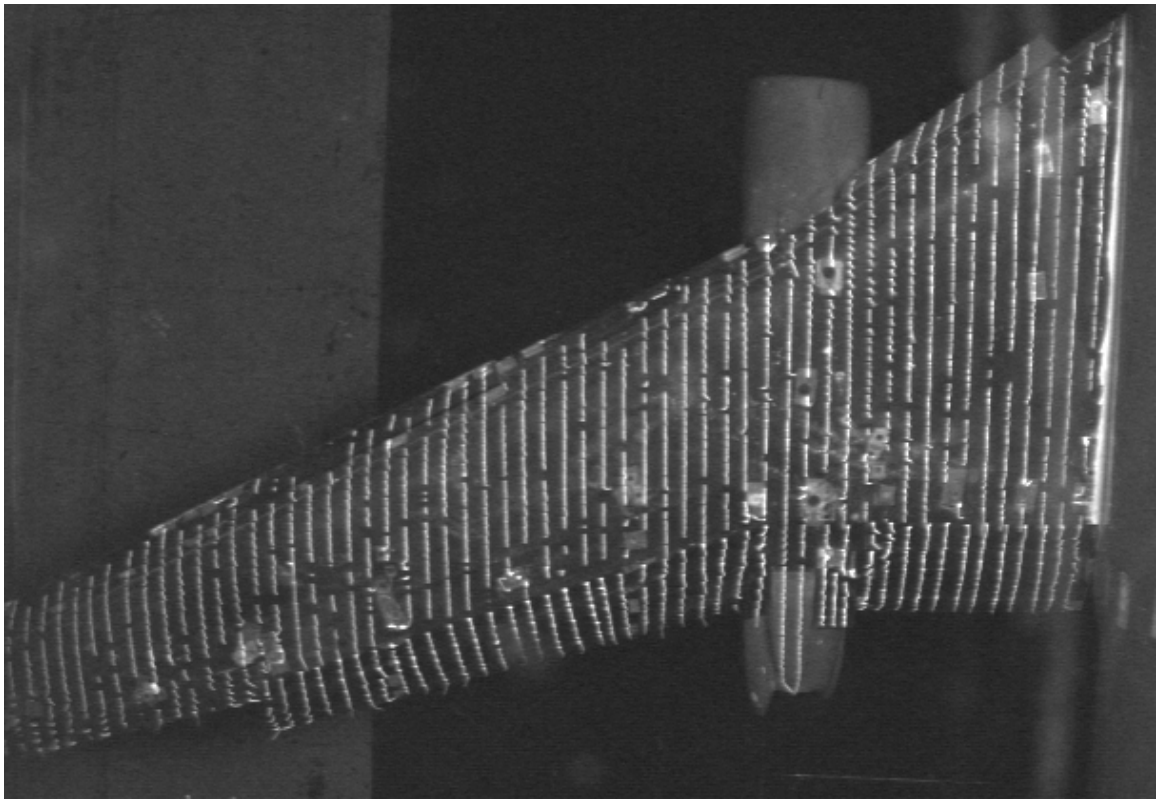

Figure 68.—-Wing mini-tuft flow visualization for no ice, $\delta_f=30^o$, $\alpha=10^o$, run 349 condition.

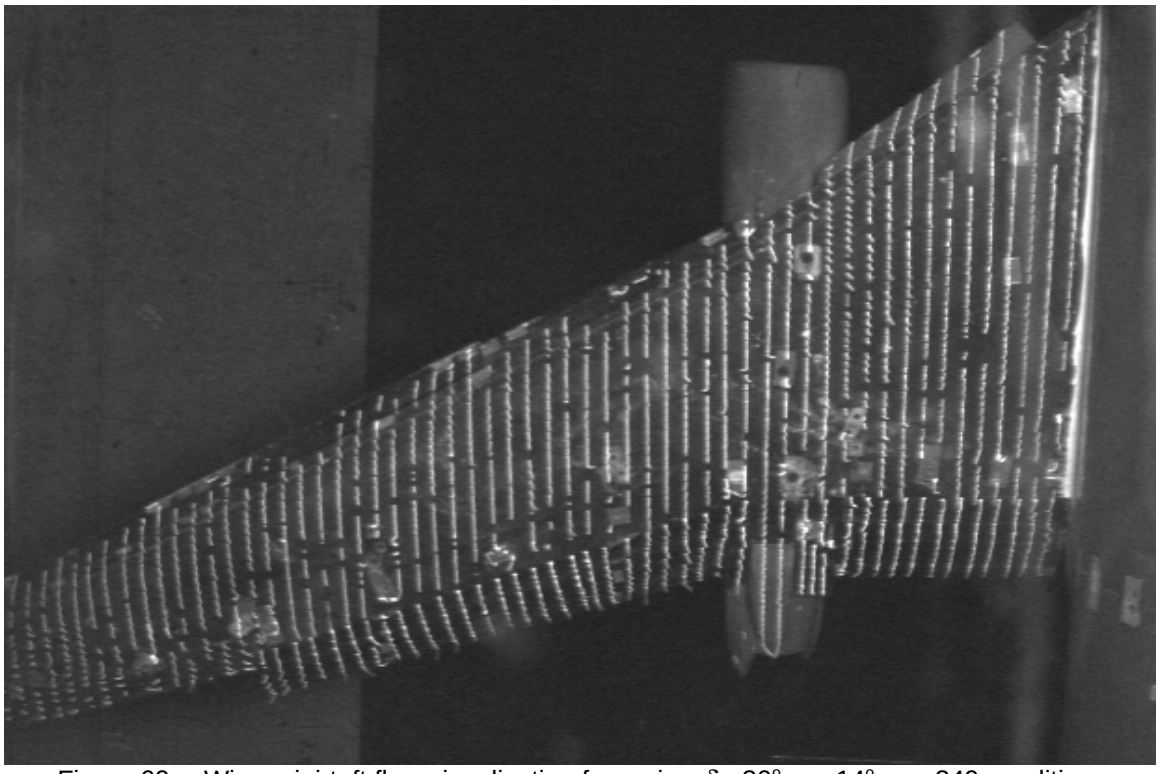

Figure 69.—Wing mini-tuft flow visualization for no ice, δ_f=30°, α =14°, run 349 condition.

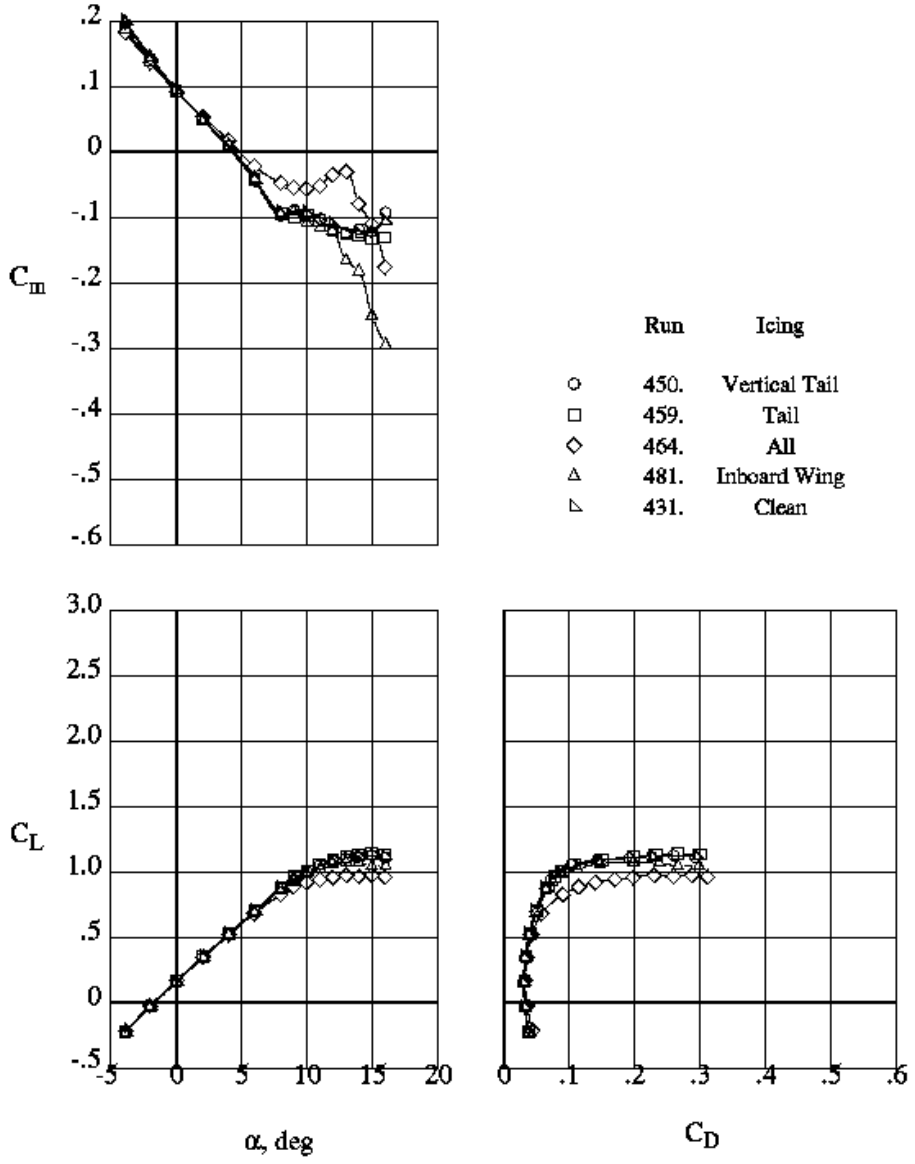

Figure 70.—Effects of Ice #1 on longitudinal aerodynamic characteristics of the model in the cruise configuration.

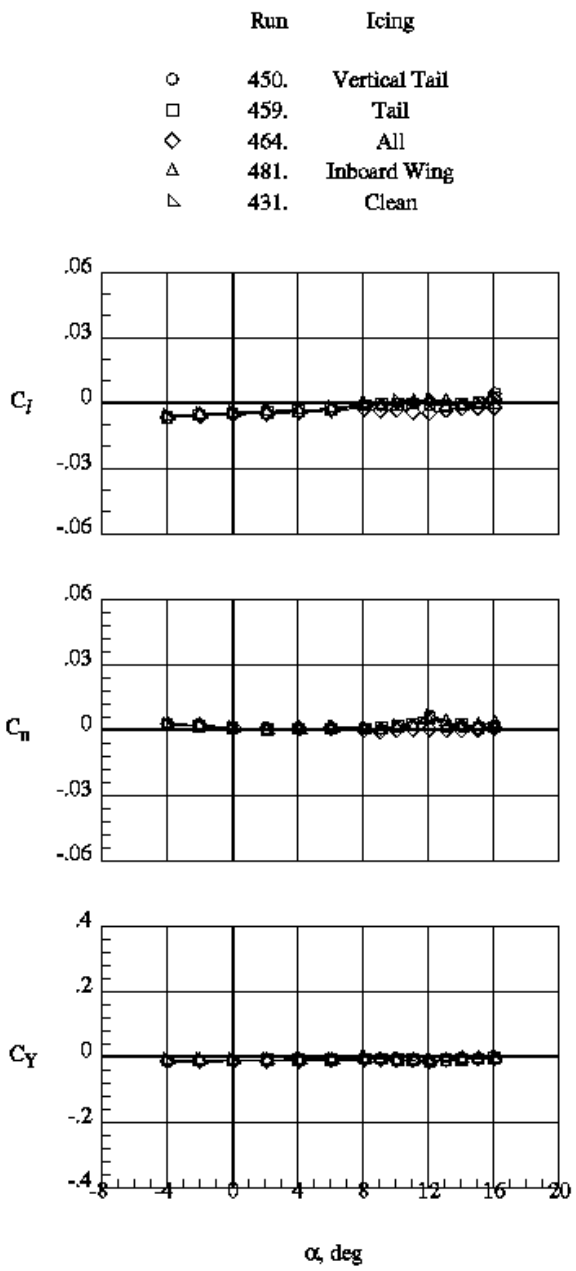

Figure 71.--Effects of Ice #1 and sideslip on the lateral aerodynamic characteristics of the model in the cruise configuration.

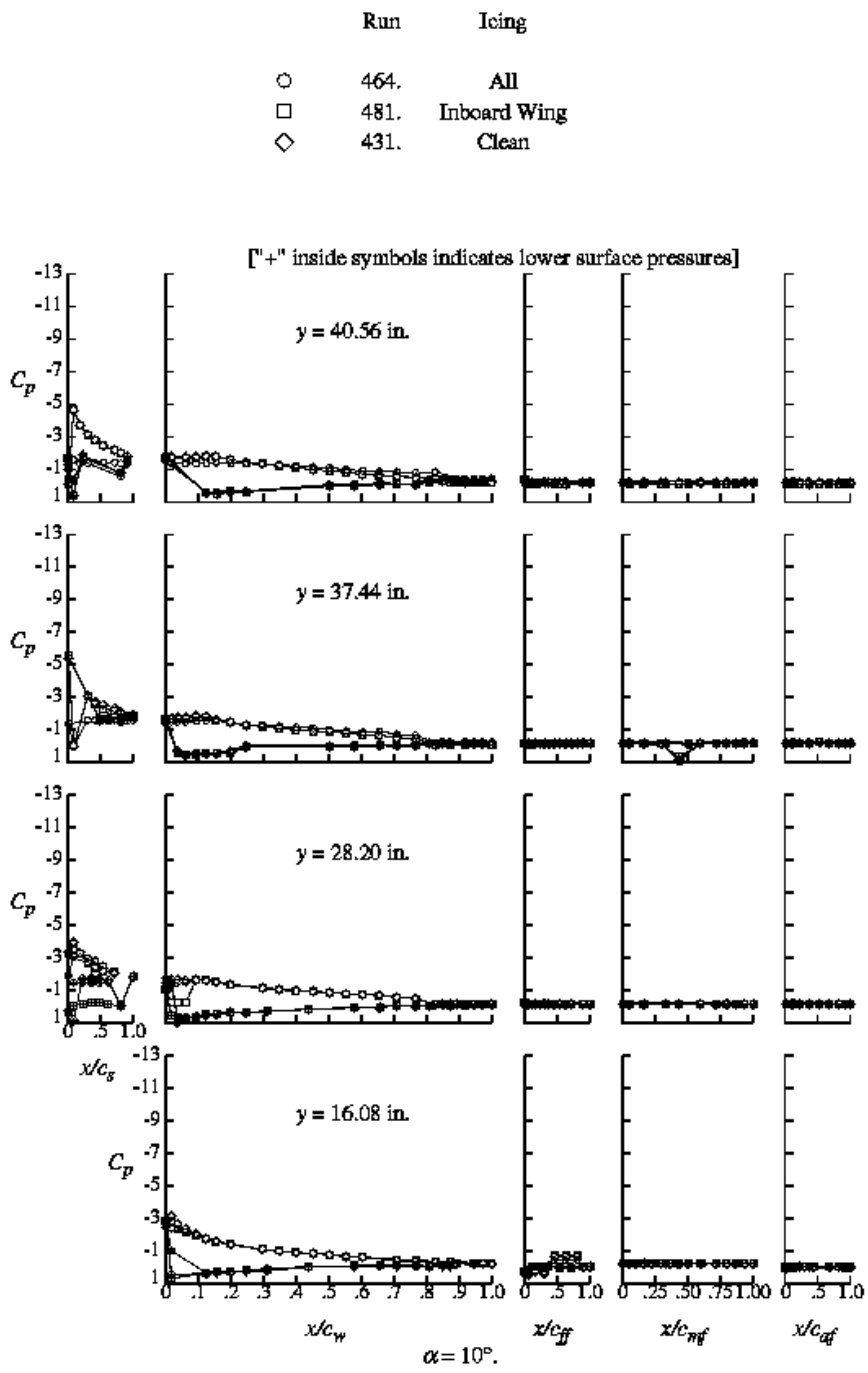

Figure 72.—Effect of Ice #1 on the wing pressure distributions for the model in the cruise configuration.

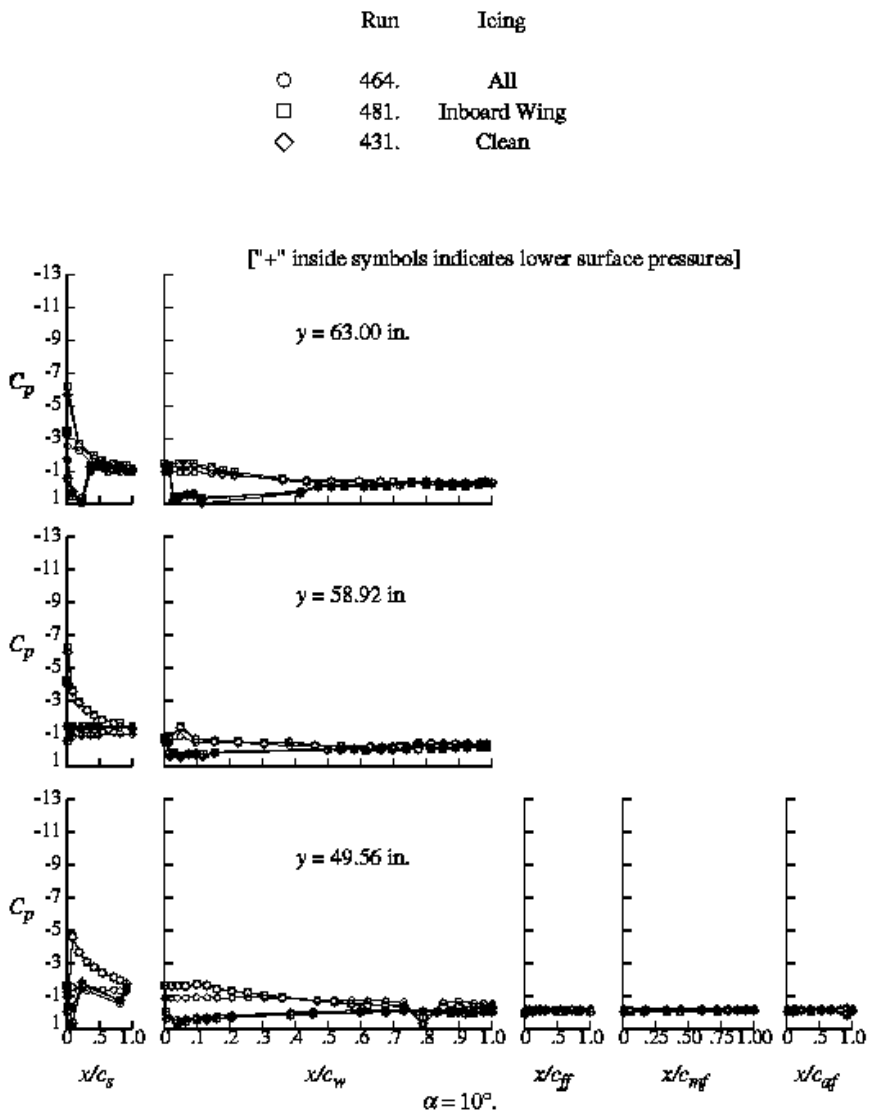

Figure 72 (concluded).—Effect of Ice #1 on the wing pressure distributions for the model in the cruise configuration.

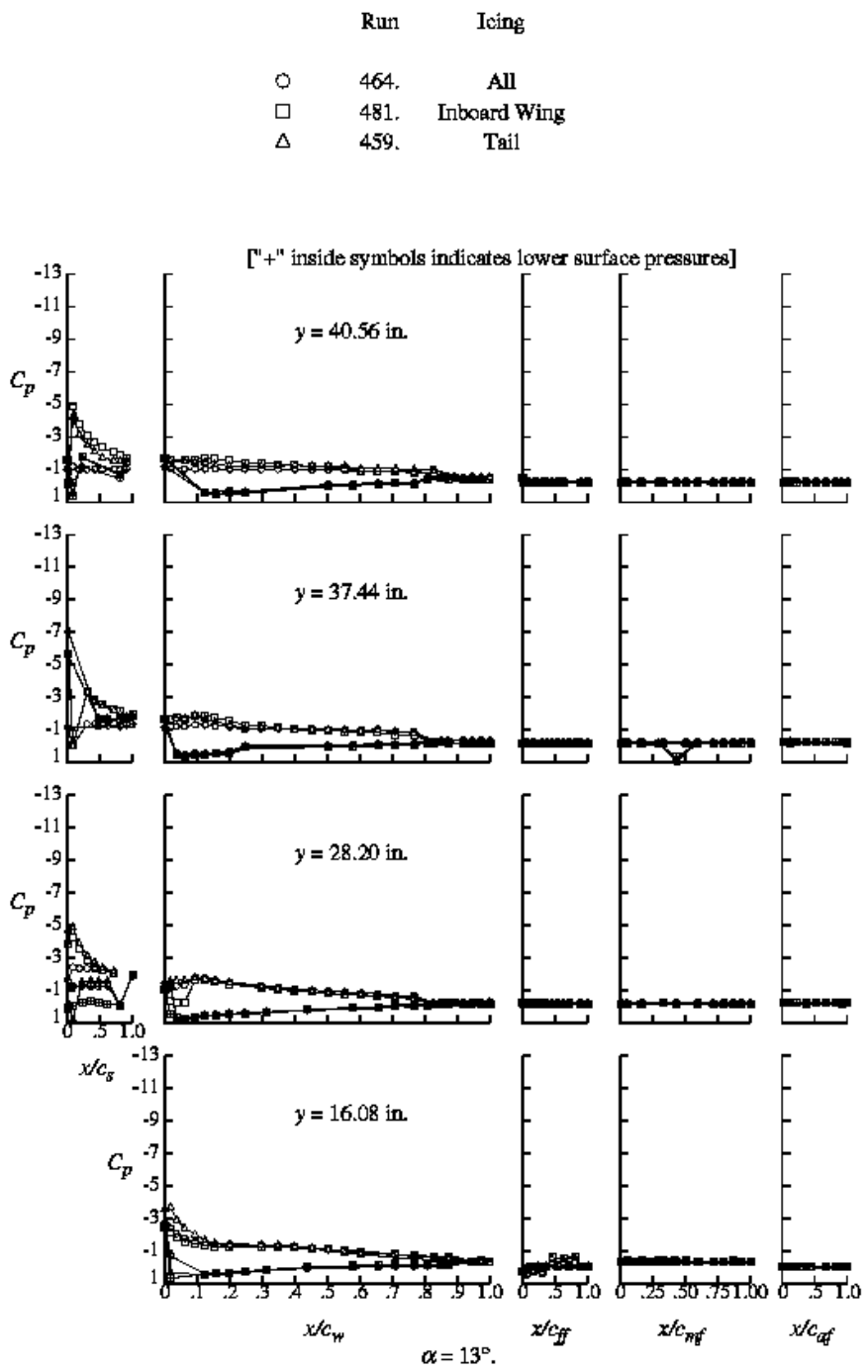

Figure 73.—Effect of Ice #1 on the wing pressure distributions for the model in the cruise configuration.

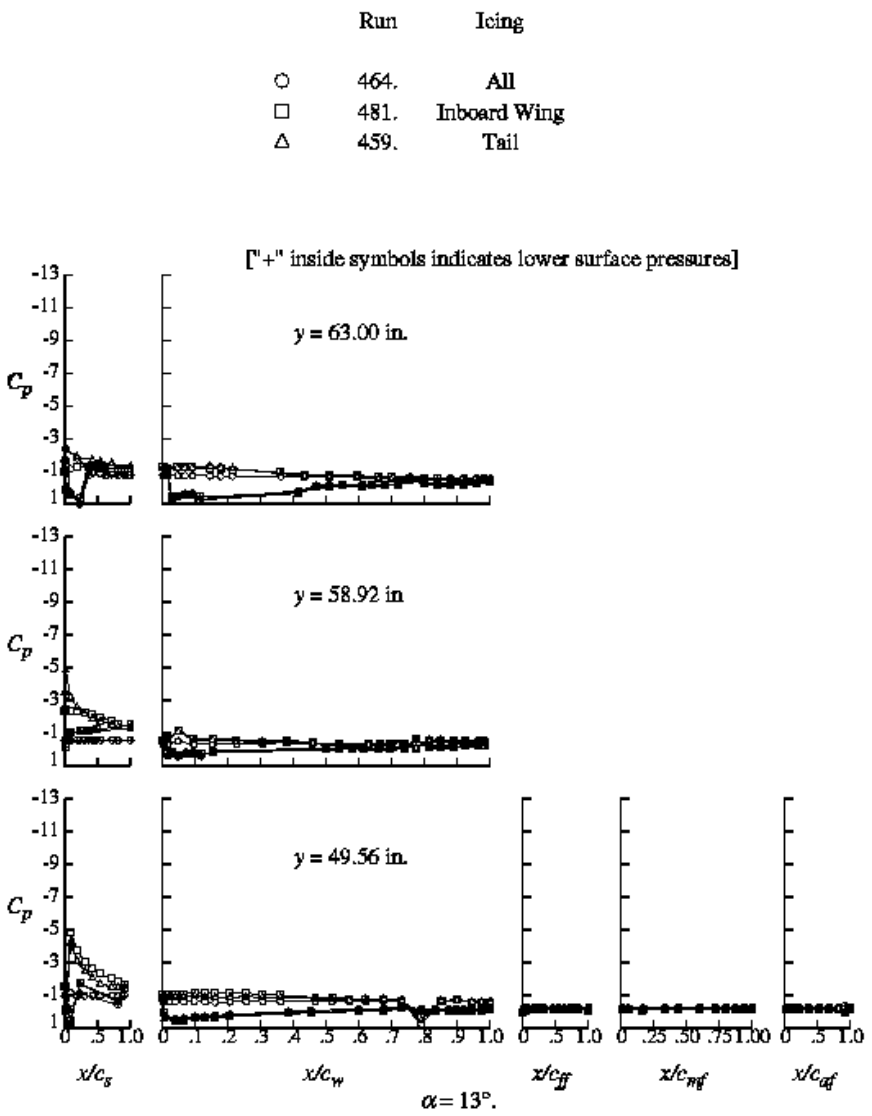

Figure 73 (concluded).—Effect of Ice #1 on the wing pressure distributions for the model in the cruise configuration.

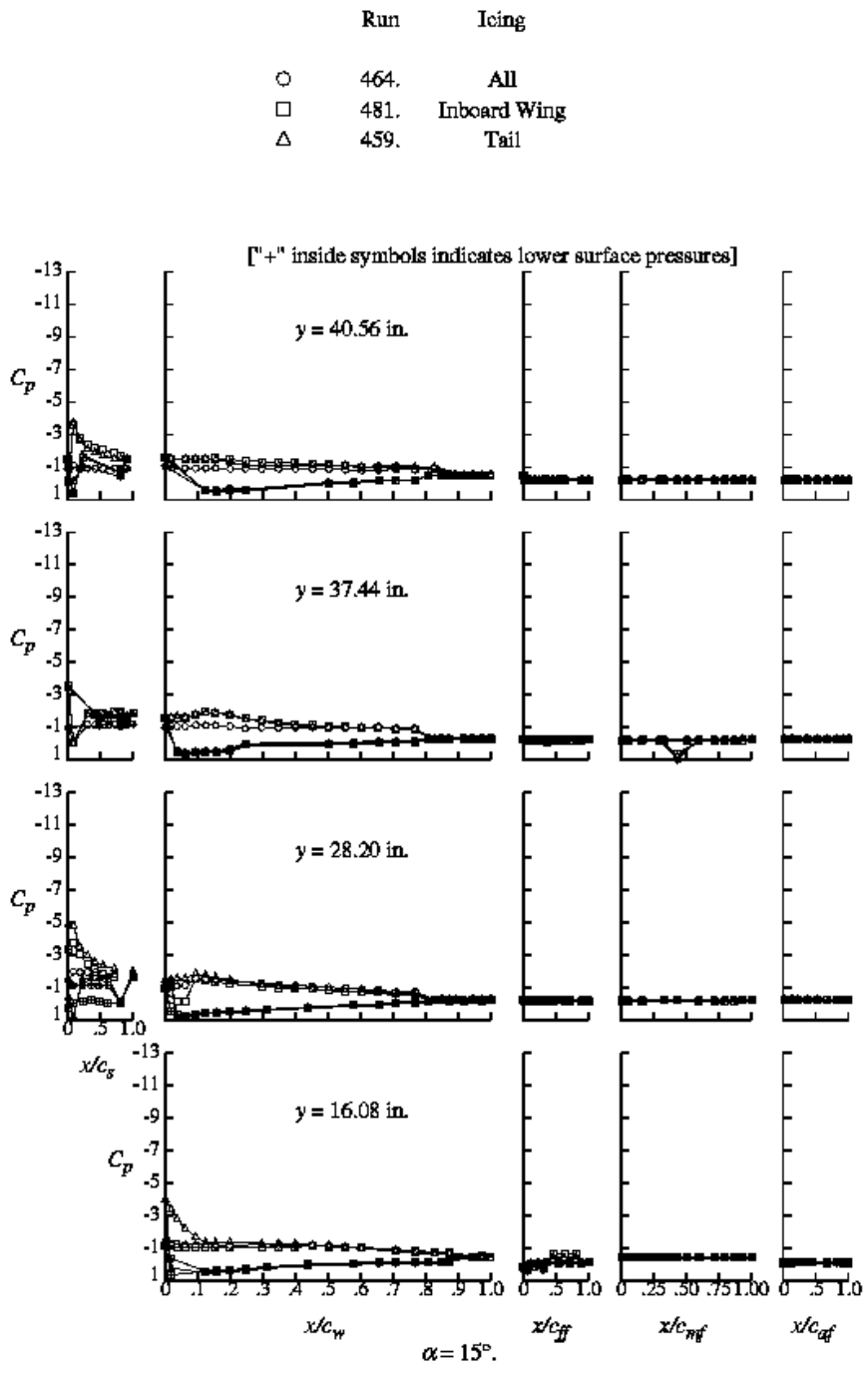

Figure 74.—Effect of Ice #1 on the wing pressure distributions for the model in the cruise configuration.

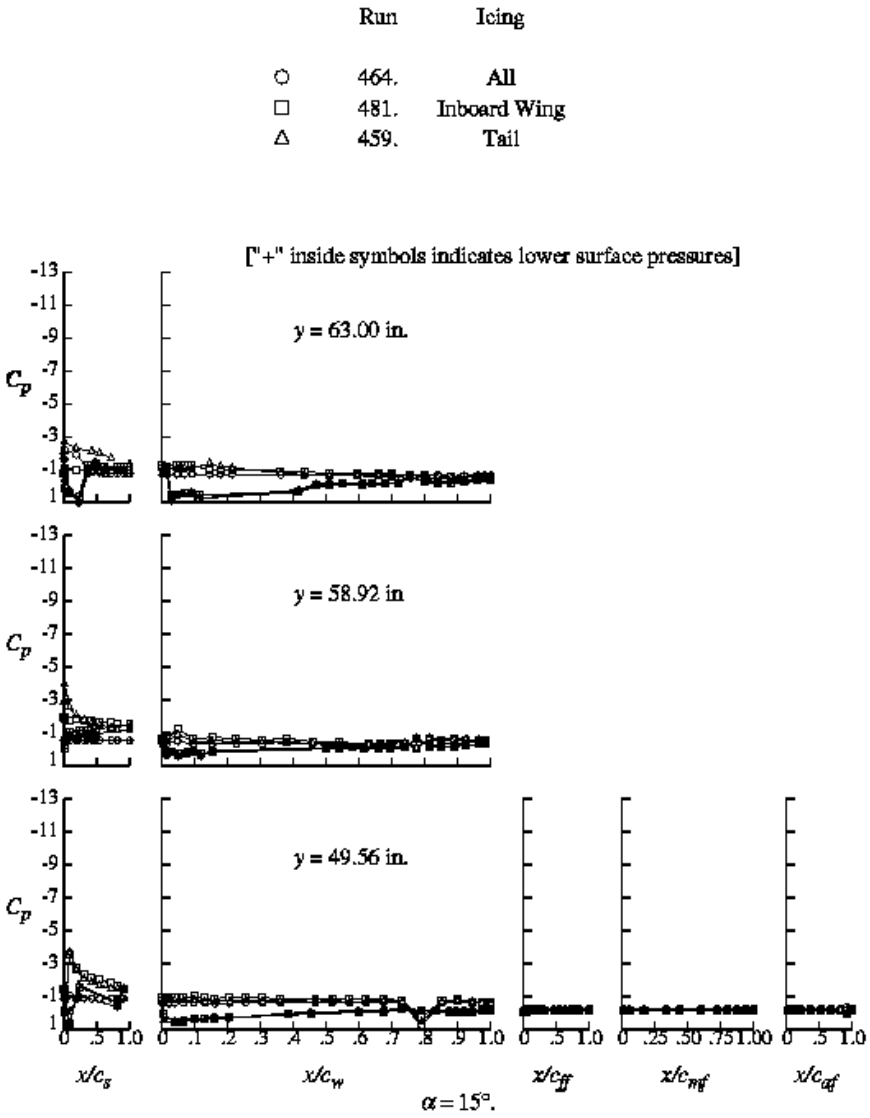

Figure 74 (concluded).—Effect of Ice #1 on the wing pressure distributions for the model in the cruise configuration.

Figure 75.—Wing mini-tuft flow visualization for all wing ice #1, cruise configuration, $\alpha=4^{o}$, run 464 condition.

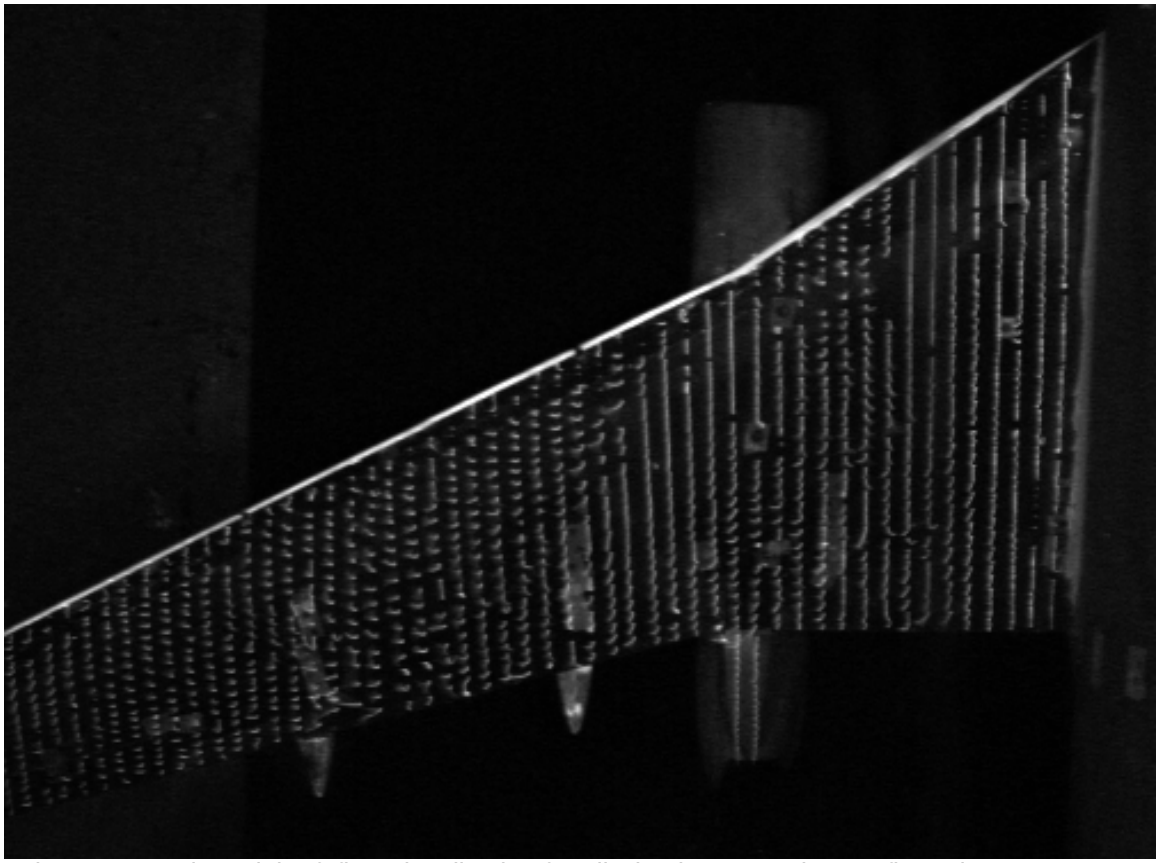

Figure 76.—Wing mini-tuft flow visualization for all wing ice #1, cruise configuration, α =10^{o}, run 464 condition.

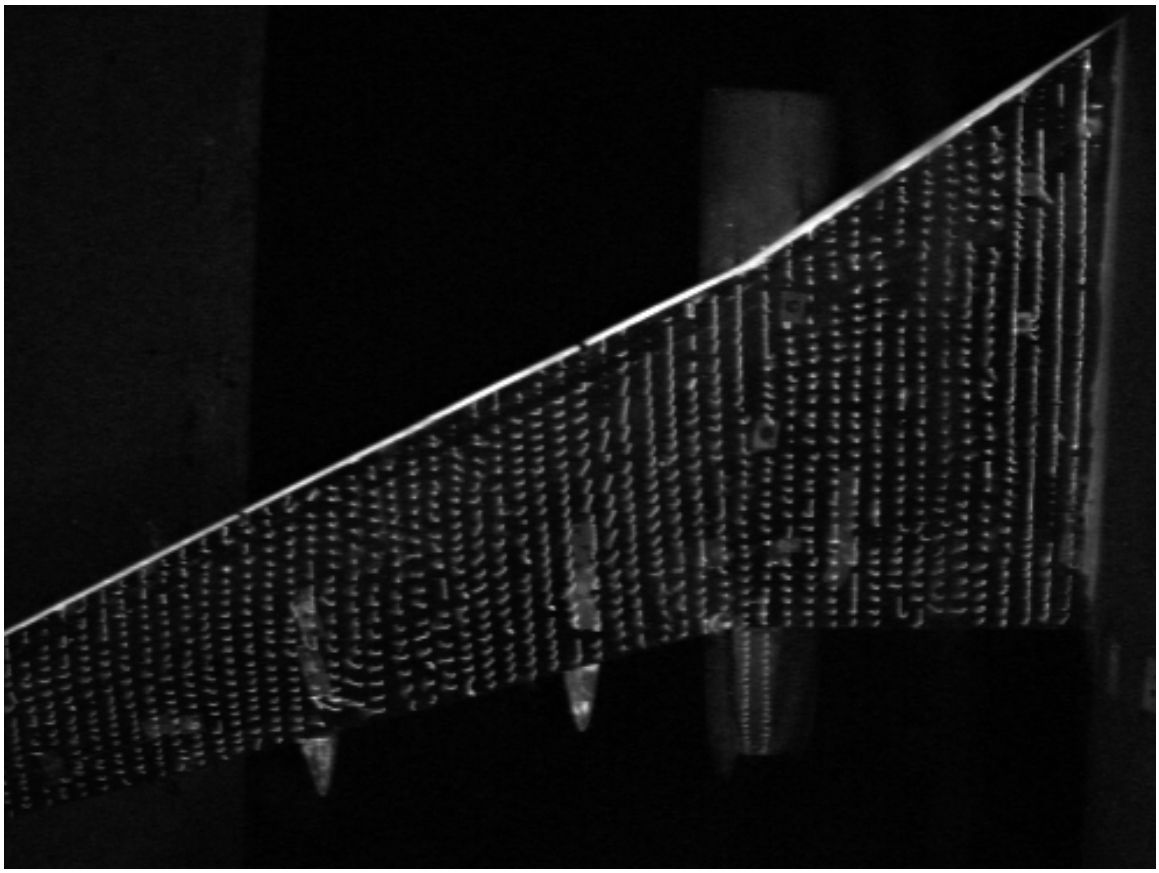

Figure 77.—Wing mini-tuft flow visualization for all wing ice #1, cruise configuration, α =14^{o}, run 464 condition.

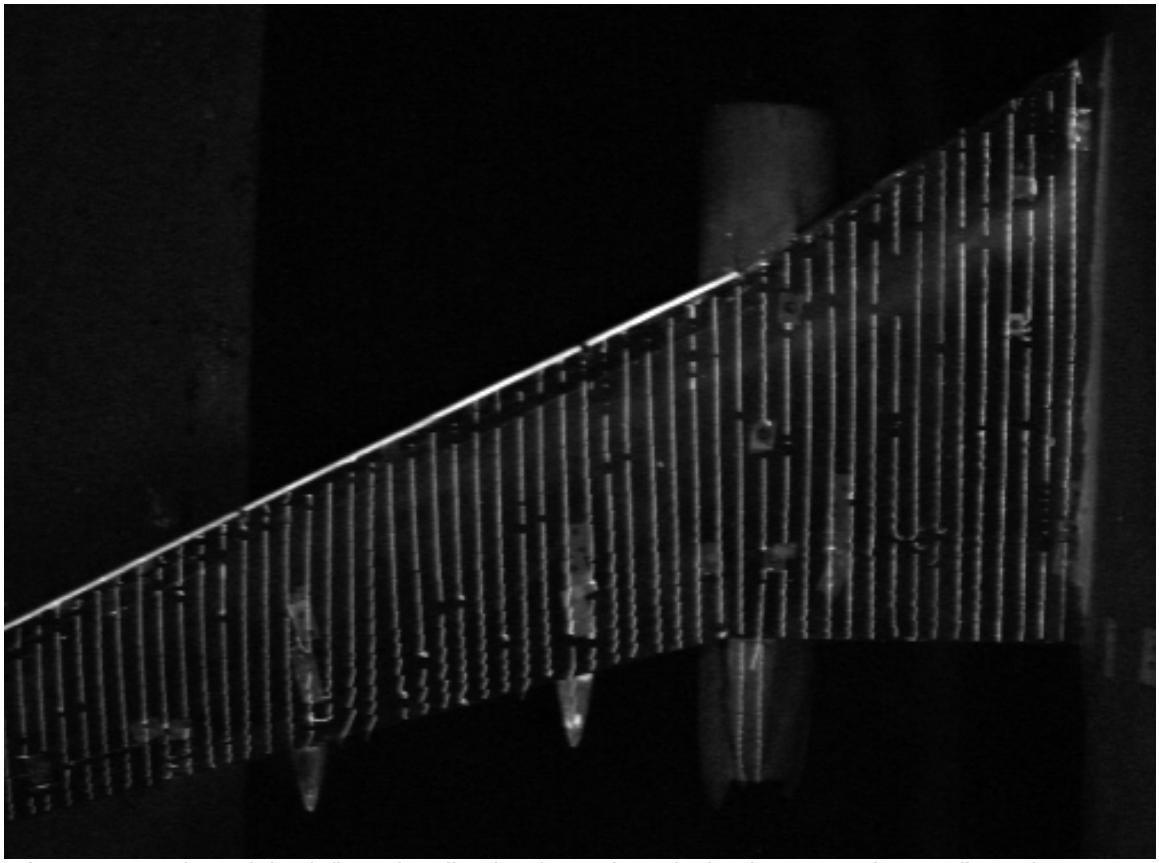

Figure 78.—Wing mini-tuft flow visualization for outboard wing ice #1, cruise configuration, α =4º, run 474 condition.

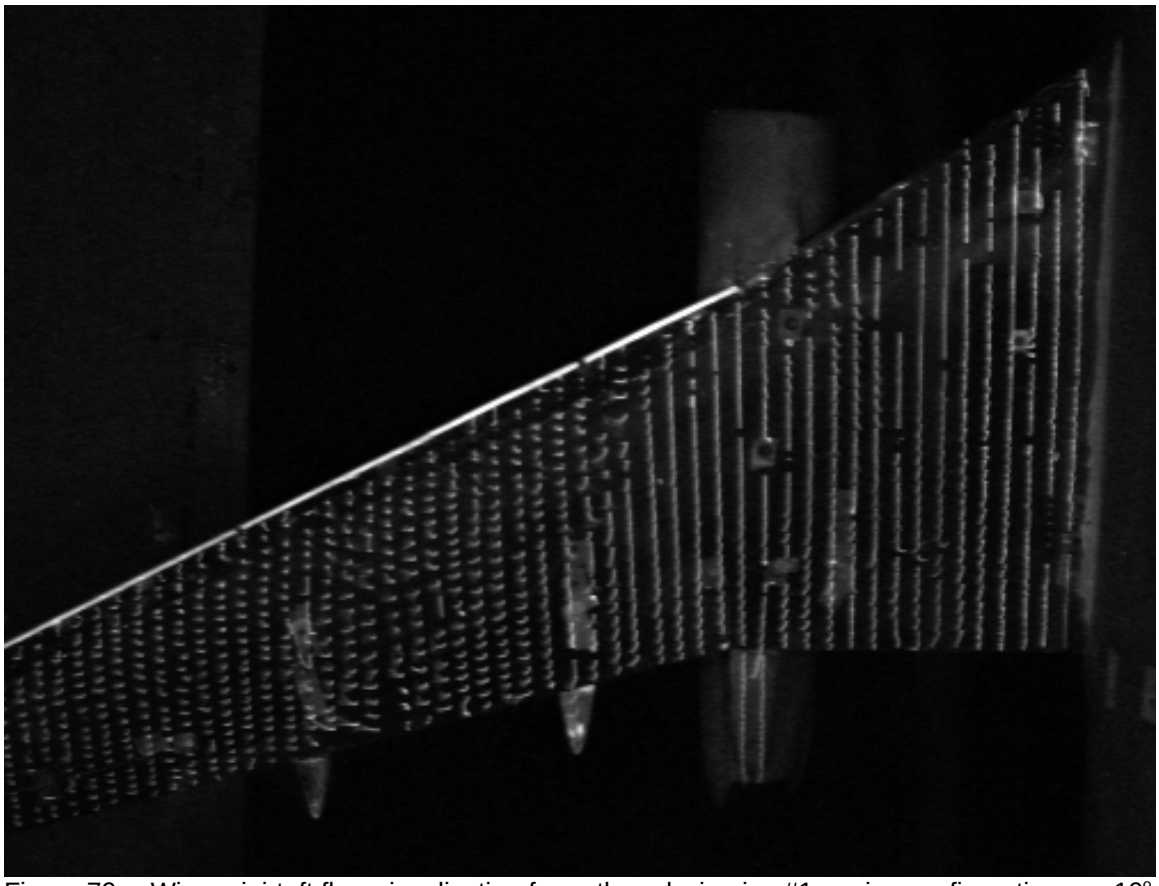

Figure 79.—Wing mini-tuft flow visualization for outboard wing ice #1, cruise configuration, $\alpha = 10^{o}$, run 474 condition.

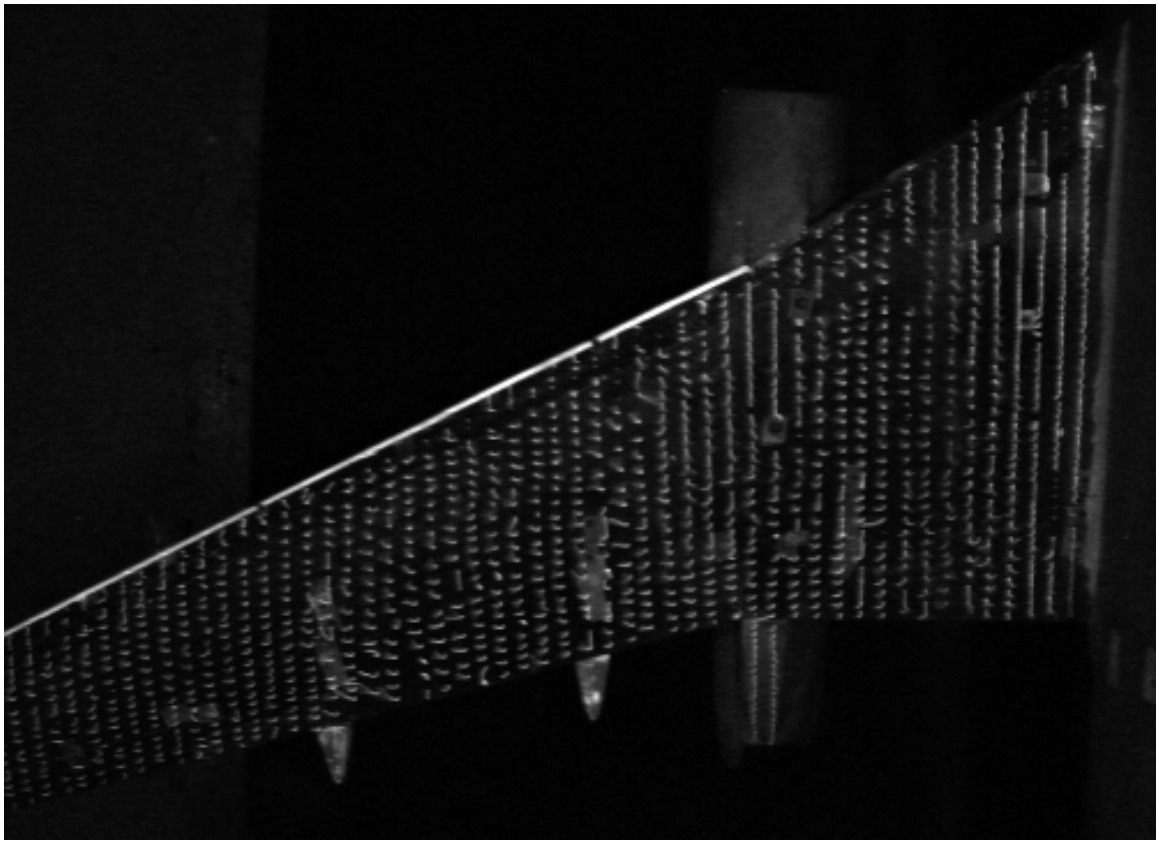

Figure 80.—Wing mini-tuft flow visualization for outboard wing ice #1, cruise configuration, α =14°, run 474 condition.

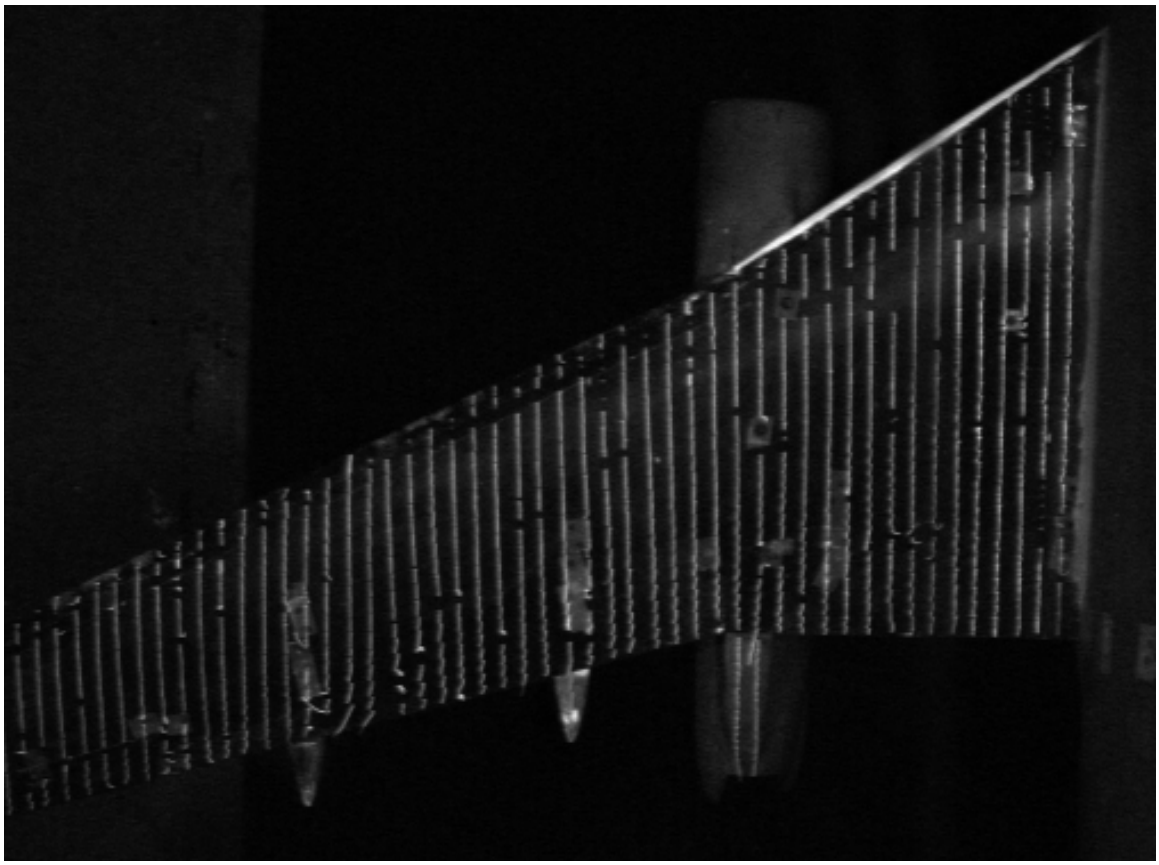

Figure 81.—Wing mini-tuft flow visualization for inboard wing ice #1, cruise configuration, $\alpha = 4^{o}$, run 481 condition.

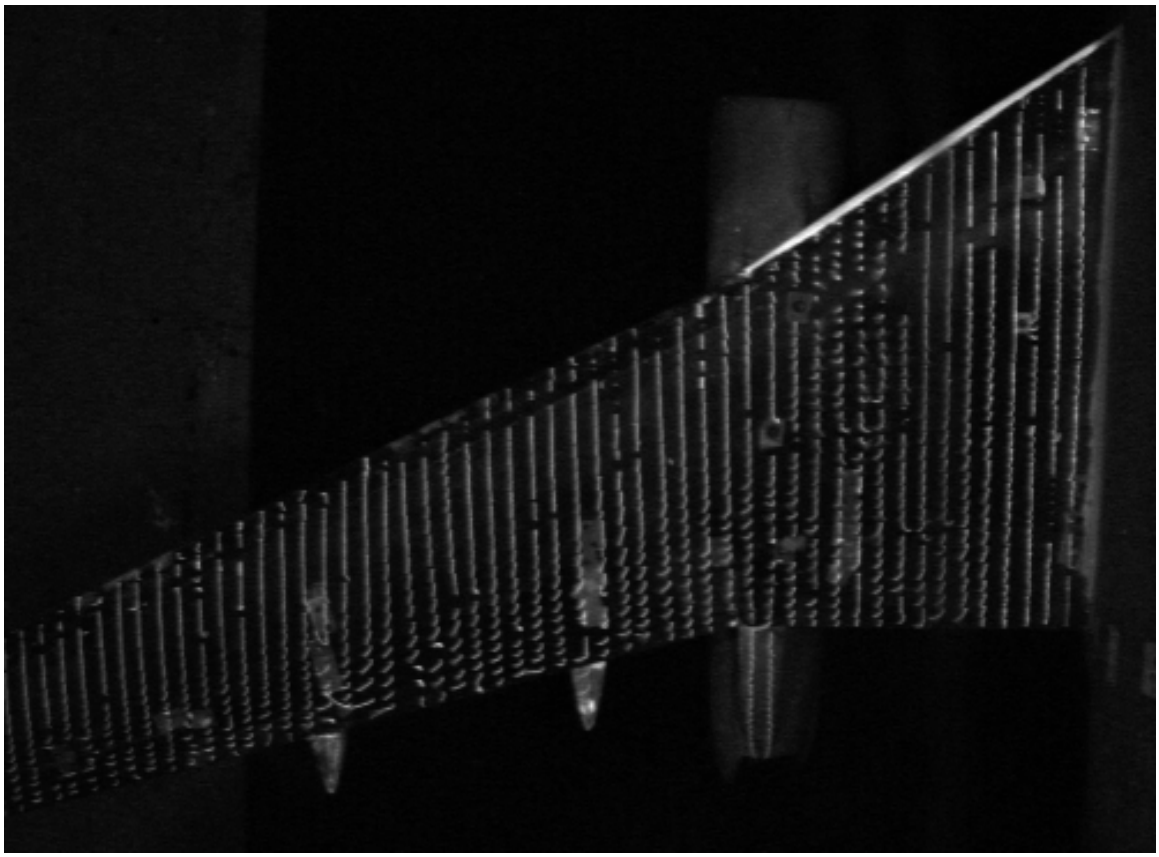

Figure 82.—Wing mini-tuft flow visualization for inboard wing ice #1, cruise configuration, $\alpha = 10^{o}$, run 481 condition.

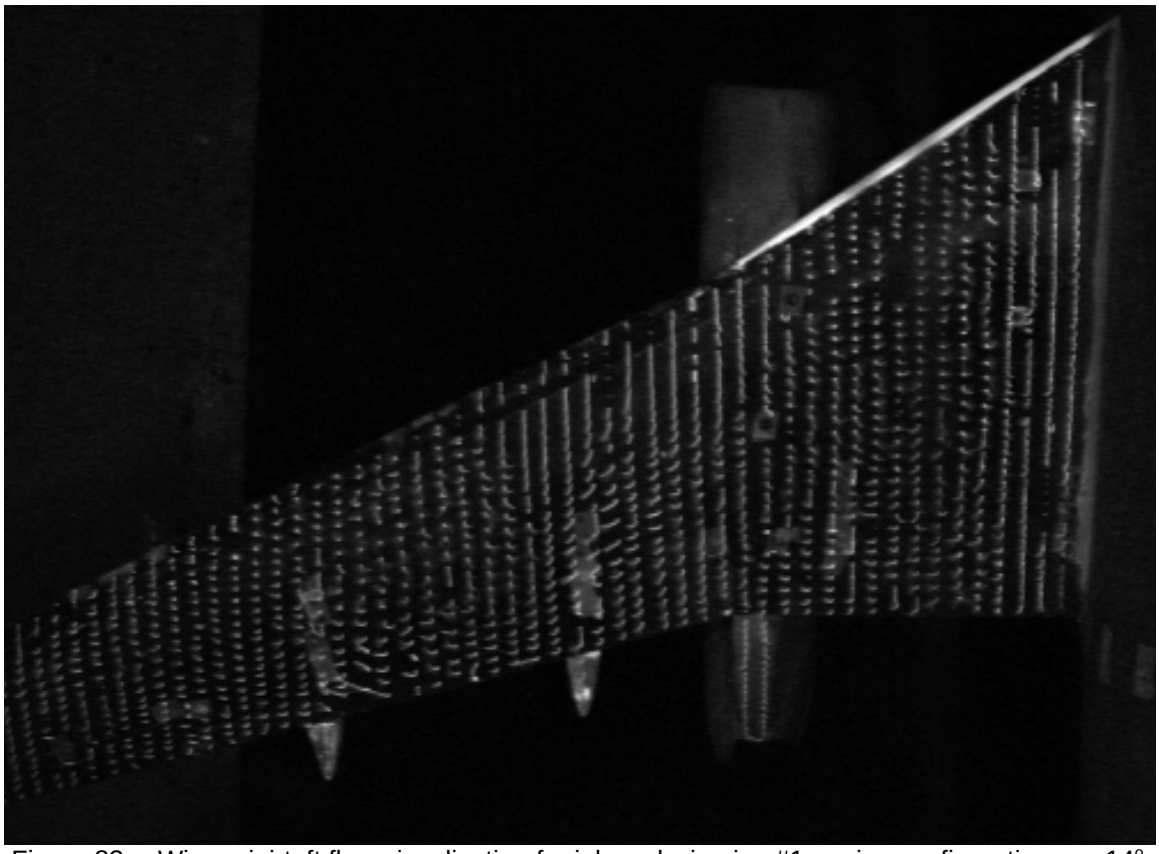

Figure 83.—Wing mini-tuft flow visualization for inboard wing ice #1, cruise configuration, α =14^{o}, run 481 condition.

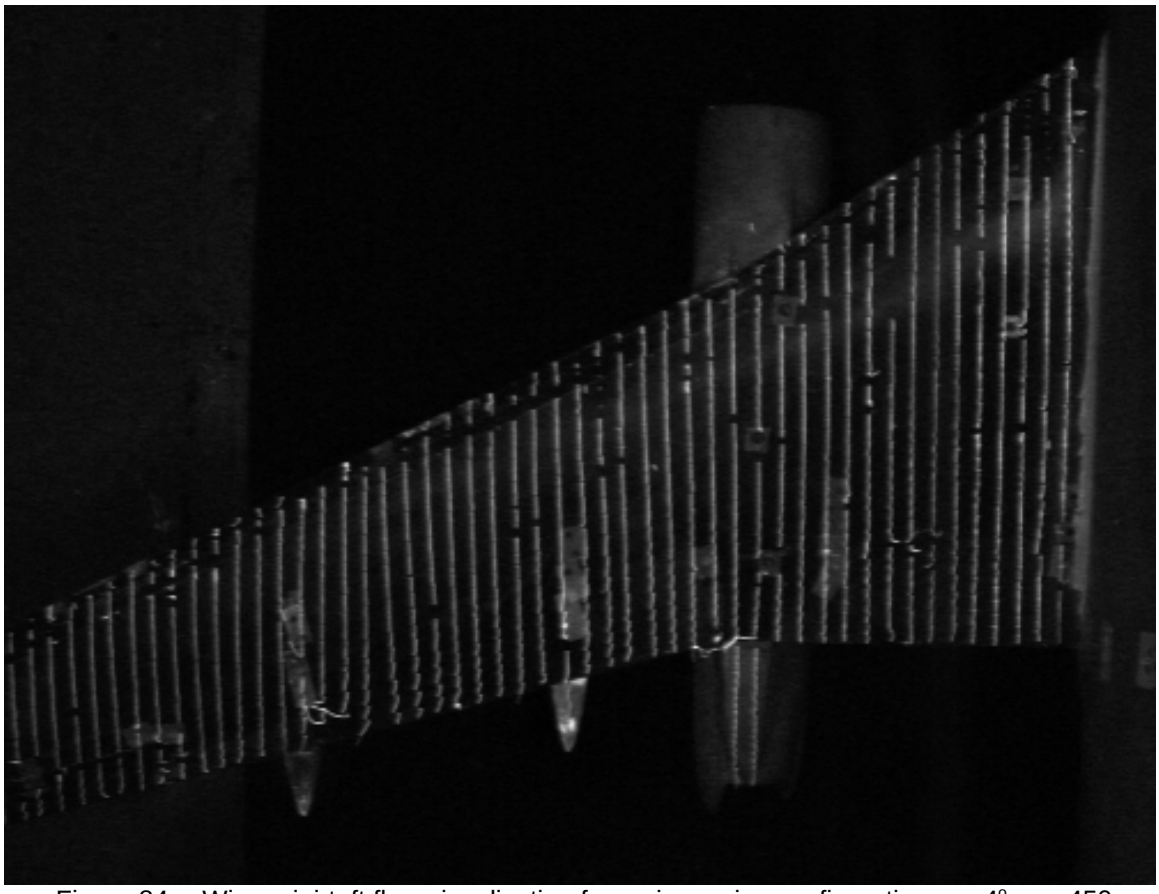

Figure 84.—Wing mini-tuft flow visualization for no ice,cruise configuration, $\alpha = 4^{o}$, run 450 condition.

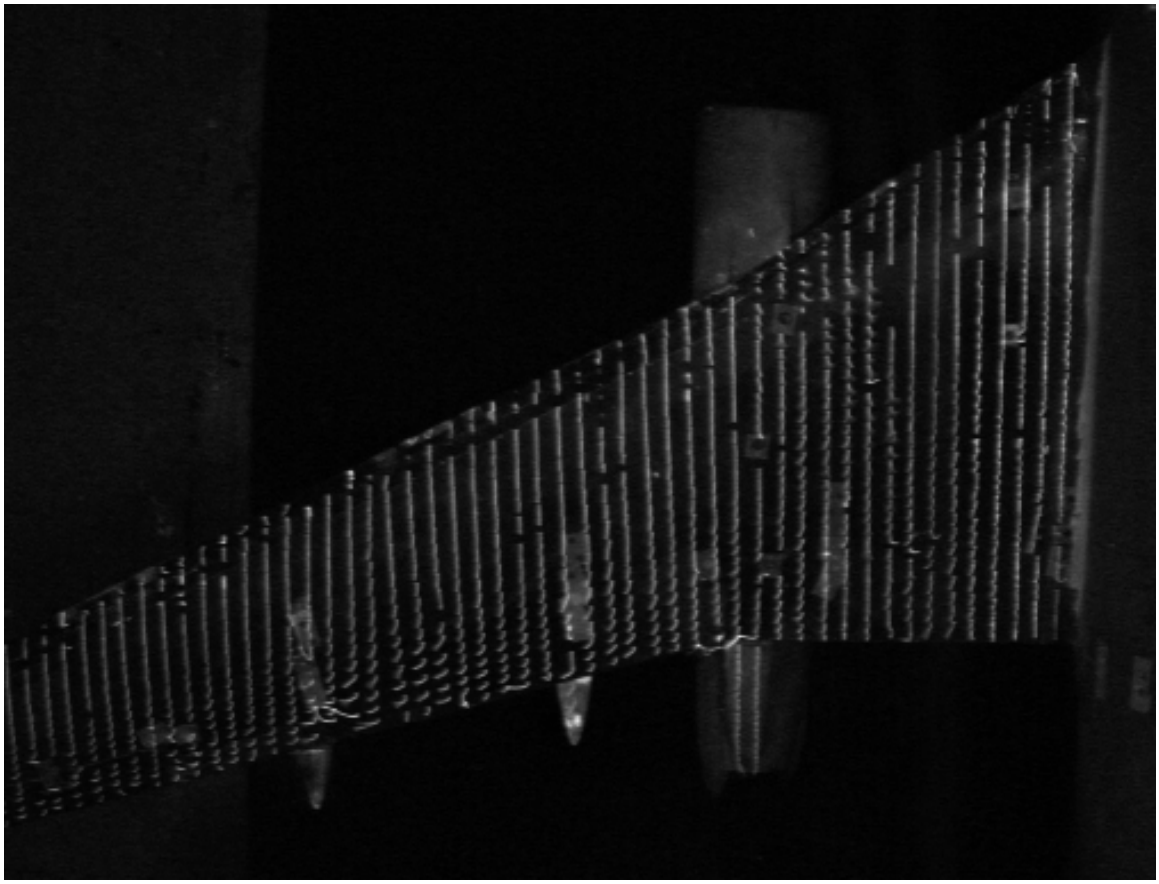

Figure 85.—Wing mini-tuft flow visualization for no ice,cruise configuration, $\alpha = 10^{o}$, run 450 condition.

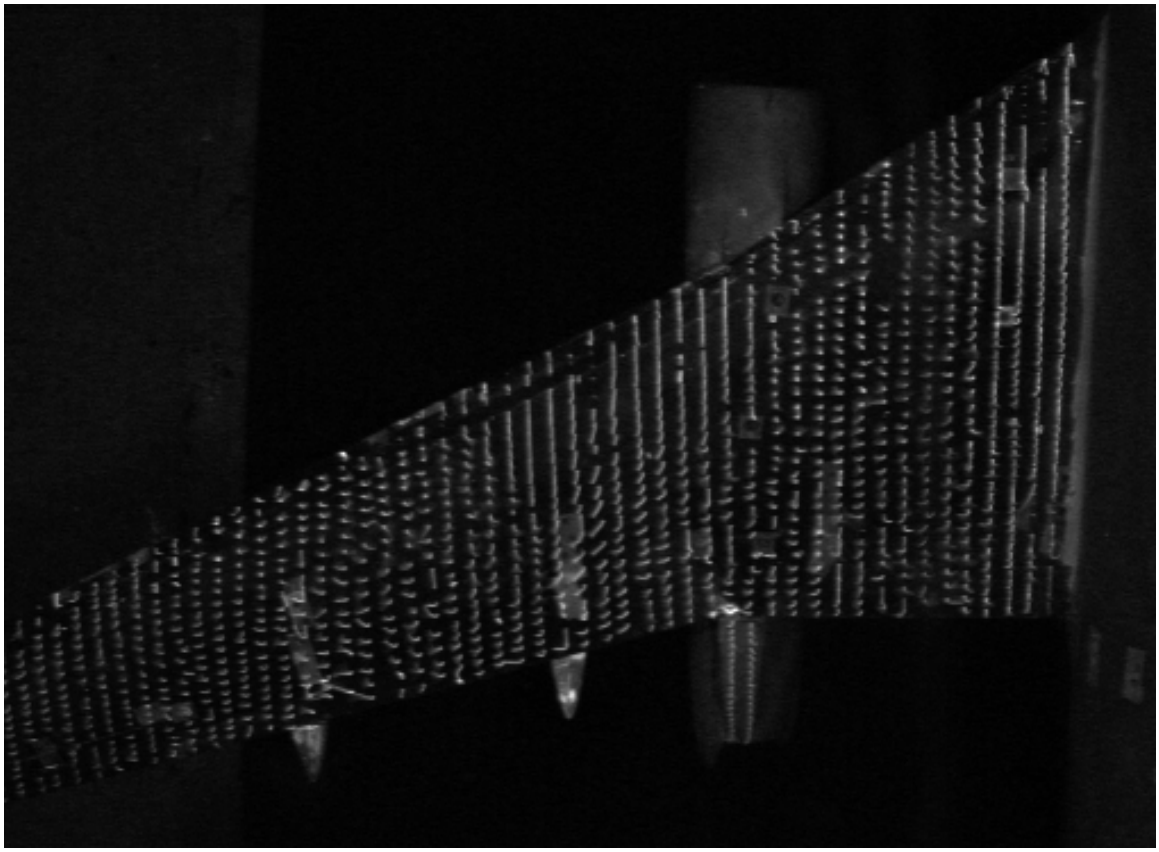

Figure 86.—Wing mini-tuft flow visualization for no ice, cruise configuration, α =14^{o}, run 450 condition.

REPORT DOCUMENTATION PAGE

Form Approved
OMB No. 0704-0188

1. AGENCY USE ONLY (*Leave blank*)	2. REPORT DATE	3. REPORT TYPE AND DATES COVERED
	May 1997	Technical Memorandum

4. TITLE AND SUBTITLE

Wind Tunnel Measured Effects on a Twin-Engine Short-Haul Transport Caused by Simulated Ice Accretions
Data Report

5. FUNDING NUMBERS

WU–548–20–23

6. AUTHOR(S)

Andrew Reehorst, Mark Potapczuk, Thomas Ratvasky, and Brenda Gile Laflin

7. PERFORMING ORGANIZATION NAME(S) AND ADDRESS(ES)

National Aeronautics and Space Administration
Lewis Research Center
Cleveland, Ohio 44135–3191

8. PERFORMING ORGANIZATION REPORT NUMBER

E–10659

9. SPONSORING/MONITORING AGENCY NAME(S) AND ADDRESS(ES)

National Aeronautics and Space Administration
Washington, DC 20546–0001

10. SPONSORING/MONITORING AGENCY REPORT NUMBER

NASA TM–107419

11. SUPPLEMENTARY NOTES

Data report for TM107143, which bears the same title. Andrew Reehorst, Mark Potapczuk, and Thomas Ratvasky, NASA Lewis Research Center; Brenda Gile Laflin, NASA Langley Research Center, Hampton, Virginia, 23681–0001. Responsible person, Andrew Reehorst, organization code 5840, (216) 433–3938.

12a. DISTRIBUTION/AVAILABILITY STATEMENT

Unclassified - Unlimited
Subject Category 03

This publication is available from the NASA Center for AeroSpace Information, (301) 621–0390.

12b. DISTRIBUTION CODE

13. ABSTRACT ***(Maximum 200 words)***

The purpose of this report is to release the data from the NASA Langley/Lewis 14 by 22 foot wind tunnel test that examined icing effects on a 1/8 scale twin-engine short-haul jet transport model. Presented in this document are summary data from the major configurations tested. The entire test database in addition to ice shape and model measurements is available as a data supplement in CD-ROM form. Data measured and presented are: wing pressure distributions, model force and moment, and wing surface flow visualization.

14. SUBJECT TERMS

Aircraft icing; Wind tunnel; Aircraft performance; Flow visualization

15. NUMBER OF PAGES

102

16. PRICE CODE

A06

17. SECURITY CLASSIFICATION OF REPORT	18. SECURITY CLASSIFICATION OF THIS PAGE	19. SECURITY CLASSIFICATION OF ABSTRACT	20. LIMITATION OF ABSTRACT
Unclassified	Unclassified	Unclassified	